University of Alberta

MICROTUBULE ORGANIZATION IN THE PRESENCE OF MOTOR PROTEINS

by

Diana White

A thesis submitted to the Faculty of Graduate Studies and Research
in partial fulfillment of the requirements for the degree of

Doctor of Philosophy

in

Applied Mathematics

Department of Mathematical and Statistical Sciences

© Diana White

Fall 2013

Edmonton, Alberta

Abstract

In this thesis, we construct a nonlocal transport model that describes the evolution of microtubules (MTs) as they interact with motor proteins. MTs, whose organization is crucial for normal cellular development, have been found to organize into various patterns *in vitro* and *in vivo* through their interactions with motor proteins. In the first part of the thesis, we state results of a simplified version of the model, a model that describes the interaction of MTs with *stationary* distributions of motors. In the second part of the thesis, we state results for the full model, a model that describes the interaction of MTs with *moving* distributions of motors. For both models, an advection-type term accounts for directed MT transport, and an integral term accounts for reorientation of MTs due to their interactions with cross-linking motor proteins. For our simplified model, directed movement corresponds to a combination of MT treadmilling and MT sliding (where motor proteins are present). In the full model, when motors are moving, directed movement corresponds to treadmilling alone. Simulations of each model show how MT patterns depend on boundary constraints, as well as different model parameters that represent motor speed, motor processivity, cross-linking capability (activity), and directionality.

For stationary motors in *large* domains, and using model parameter values for motors that are consistent with experimental values, we find that patterns such as asters, bundles, and vortices are able to persist. *In vivo*, MTs take on aster patterns during interphase. Also, in neurons and polarized epithelial cells, MTs form bundles. Vortex patterns have not been observed *in vivo*, however are found in *in vitro* experiments. In *constrained* domains, we find that similar patterns form. However, we also find that when two opposing motors are present, anti-parallel bundles are able to form. Such patterns are similar to those found in the mitotic spindle during cell division. Our model quantitatively describes how motors are involved in MT patterning. To date, there are no other models that describe such patterning by explicitly incorporating motor properties (for **stationary motors**) into a model for MT evolution.

For moving motors, we simulate our model using periodic boundary conditions, representing MT organizations in large domains. We do this to compare our simulation results with results that have been found *in vitro*. Also, we simulate our model using parameters consistent with fast and slow processive motors, fast non-processive motors, and slow weakly processive motors, similar to the types of motors used in experiments. Similar to experiments, we find that depending on motor type and density, various types of patterns, such as arrays of asters, arrays of vortices, and clusters of disorganized MTs exist.

Consistent with previous theoretical models, we find that MT patters depend on motor density. In particular, for specific motor types, MTs form vortices at low motor density, asters at intermediate values of motor density, and bundles at high motor densities.

Acknowledgements

I would like to thank my supervisor Adriana Dawes for her insight, useful advice, and positive attitude through high and low times. I would also like the thank my co-supervisor Gerda de Vries, for her patience, guidance and support, and for teaching me how to be a critical thinker and communicator of science. I would also like to thank Thomas Hillen, for his useful suggestions regarding the more technical mathematical analysis in this thesis.

Finally I would like to thank the Center of Mathematical Biology for always giving helpful feedback, my family for their unconditional love and support, and my partner and best friend Jonathan Martin, for his useful advice in the modeling aspects of this thesis and for always being there for me.

Table of Contents

List of Tables

List of Figures

Chapter 1

Introduction

In this thesis, we develop a mathematical model to describe how microtubules (MTs) are organized in two-dimensional space as they interact with a class of proteins called motor proteins. In particular, we develop a novel integro-partial differential equation to describe MT evolution, that is coupled to a reaction-diffusion system of equations to describe motor evolution. It is important to develop and study such models because MT organization (which is effected by interactions with motor proteins) is directly linked to normal cellular function. In particular, MTs take on different organizations, with the aid of motor proteins, where these organizations play a crucial role in cellular processes such as cell division, cell movement, as well as cell polarization [28]. The importance of MT organization is highlighted in detail in Section 1.3, and consequences of unregulated MT organization are highlighted in Section 1.5.

MTs were discovered in the mid 1950s [7], and it was at this time that their structure was fully described (see Section 1.1). One of the most interesting breakthroughs in the field of MT research was in the 1980's, when a unique type of MT behavior, referred to as dynamic instability (described in detail in Section 1.1), was discovered [31]. It was at this time that MTs also gained widespread interest in the clinical world [71], in particular in cancer treatment protocols. The reason for this interest is because MT dynamic instability is required for cell division. So, by altering the dynamics of MTs, one can alter the process of cell division in all cells, including those that are cancerous. In particular, evidence suggests that even minor alterations of MT dynamics can arrest the cell cycle progression at mitosis, eventually leading to apoptotic cell

death. A number of different drugs are clinically used to alter MT dynamics during cell division, with two of the most successful families of drugs being the vinca alkaloids and taxanes. These particular drugs are used in the treatment of a variety of human cancers and belong to a large class of drugs referred to as chemotherapeutic drugs.

The problem of MT reorganization is very exciting because it has only been in recent years that imaging techniques have advanced to the point where we can capture 3-dimensional images of MTs, and track their movements over time. Thus, it is now possible to test model hypotheses experimentally. In particular, we can use experimental imaging techniques to track the evolution of MTs and motors, and compare the images captured from experiments with simulation and theoretical results. An important feature of our model is that it only has two interacting components, MTs and motors. This feature is experimentally advantageous, since there are a relatively small number of biological variables to consider when conducting *in vitro* experiments (as compared to MT organization in real cells). In general, we know that there are many different factors that contribute to MT organization in cells, but in this project we will focus only on MTs and motors, since in *in vitro* studies, it has been shown that MTs organize into many different patterns in systems comprised only of MTs and motors (as described in Section 1.3). Also, it has been shown that motors play a key role in MT organization *in vivo* (as described in Section 1.3.2). In particular, our model will describe the individual movements of MTs (referred to treadmilling, and described in detail in Section 1.1), and their interactions with motor proteins (described in Section 1.2). A detailed description of MT organization found *in vivo* and *in vitro* is given in Sections 1.3 and 1.4, respectively, and an example of what can happen when MT organization is disrupted is given in Section 1.5. For the major questions addressed in this thesis, and a preview of the thesis results, please refer to Section 1.6.

1.1   Microtubule structure and dynamics

Microtubule structure: Microtubules, along with actin polymers and intermediate filaments, are a main type of cytoskeletal filaments that make up
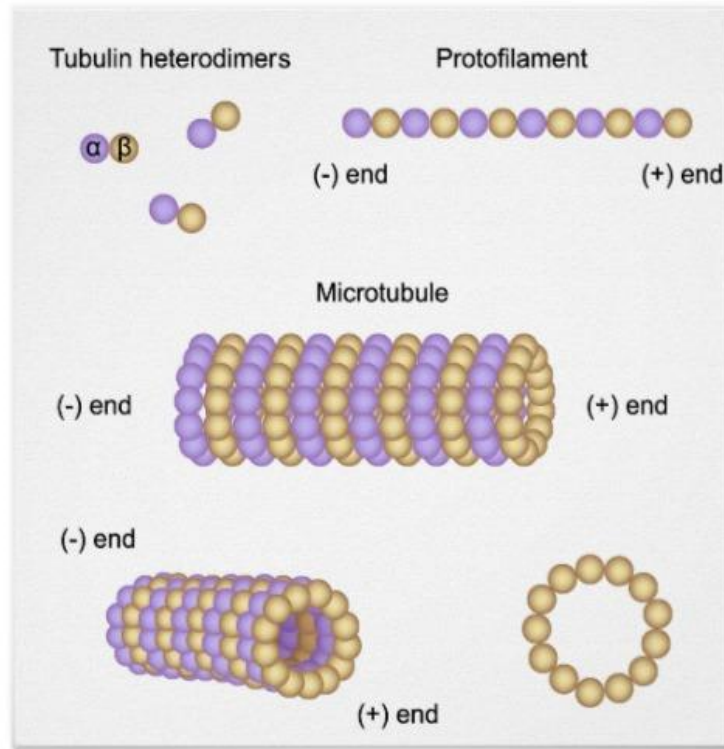
Figure 1.1: Structure of a single microtubule showing 13 protofilaments, each is composed of α- and β-tubulin heterodimers, connected laterally forming a hollow cylinder.

the cytoskeleton of cells [28, 65]. MTs are rigid protein polymers that are composed of a single type of globular protein called tubulin. Tubulin is a heterodimer, consisting of the protein subunits α- and β-tubulin, that polymerize in the cell to form MTs. In general, 13 protofilaments are associated with a single MT (see Figure 1.1). The protofilaments are arranged linearly, connected side-by-side in a circular fashion, so that each MT forms a long cylinder with a hollow core.

Along each protofilament, the α- and β-tubulin are aligned in a head-to-tail fashion, so that each MT is a polar structure with two distinct ends. The positive end (the end with the majority of the β-tubulin) is generally more dynamic, being able to grow and shrink relatively fast, while the negative end (the end with the majority of α-tubulin) is less dynamic with slower growth and shrinking rates. A MT grows (polymerizes) by the addition of tubulin dimers and shrinks (depolymerizes) by the subtraction of tubulin dimers.

3

Microtubule dynamics: As stated above, MTs typically grow through the addition of tubulin dimers at the positive end of a MT. During growth, both α- and β-tubulin units are bound to a guanosine-5'-triphosphate (GTP) molecule, an energy source that is essential for the polymerization of MTs [20, 28, 65]. The GTP bound to the α-tubulin is not exchangeable for the lower energy guanosine diphosphate (GDP) (and so it is stable), while the GTP bound to the β-tubulin can be hydrolyzed to the lower energy GDP. In order for MTs to grow, the positive end of the MT must contain β-tubulin bound to the higher energy GTP. If the tip of the MT contains the lower energy GDP, the end of the MT becomes unstable and is prone to depolymerization. In general, if a cap of tubulin dimers with GTP-bound β-tubulin exists at the front (positive end) of a MT, it can continue to grow. However, if hydrolysis catches up with the growing end, the MT will collapse, and quickly depolymerize. This process is referred to as a *catastrophe*. Once the end of the MT exchanges GDP for GTP, the MT tip can rebuild its cap and start growing again. This process is referred to as a *rescue*. The unique GTP binding and hydrolysis property of MTs gives them two interesting dynamic properties, referred to as dynamic instability [31, 68] and treadmilling [38, 67].

Dynamic instability was discovered by Mitchison and Kirschner [31], and refers to the slow polymerization of a MT followed by a much faster depolymerization (see Figure 1.2). This behavior has been observed both *in vivo* and *in vitro*, and is a common type of behavior found in most cell types.

MT treadmilling is a chemical process that is defined as the steady-state unidirectional flux of subunits through a polymer as a result of continuous net assembly at one end of a polymer and continuous net disassembly at the other end. In MTs, this means that the reaction rate of assembly of tubulin dimers at the positive end of a microtubule is approximately the same as the rate of disassembly at the negative end of the same microtubule. The net result is the apparent directed (constant) motion of the MT towards its positive end (see Figure 1.2).

In general, MT treadmilling is a slower process than dynamic instability, however, both processes have been found to be key contributors to MT reorganization. In particular, mathematical models of aster formation in fish

4
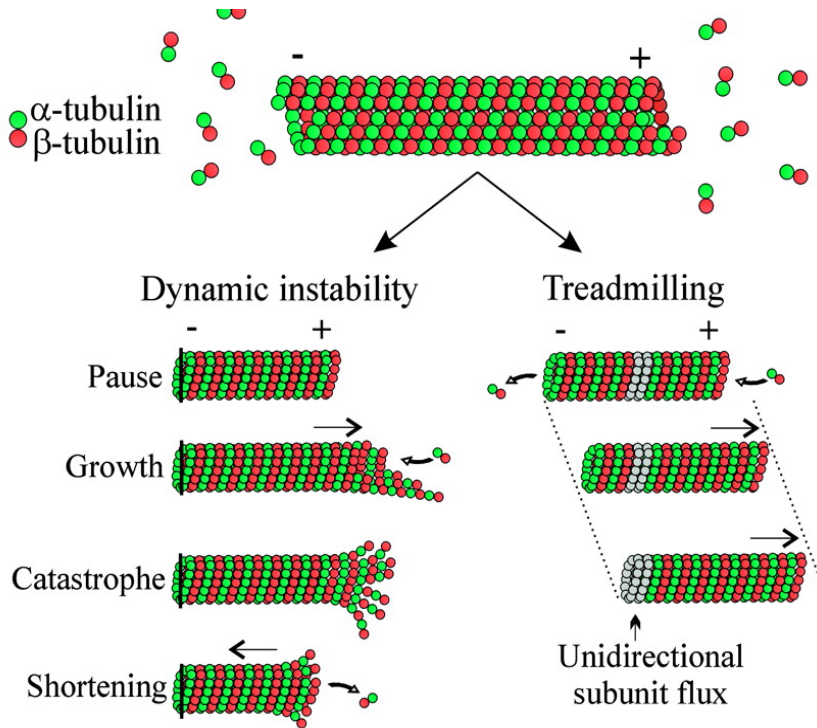
Figure 1.2: Dynamic instability and treadmilling in microtubules. Picture taken from [?].

melanophores reveal how MT asters form by MT treadmilling and nucleation alone [9] (an example of aster configuration shown in Figure 1.5(a)). Also, theoretical models describing MT organization resulting from dynamic instability show the existence of exponentially decreasing MT length distributions [10, 70]. Such results are similar to length distributions found in many cell types that take on a centrosomal (aster) configuration. Other examples describing the importance of treadmilling and dynamic instability in MT organization are given in Section 2.1 and 2.2, respectively.

1.2 Motors and microtubule associated proteins

There are many different types of proteins that associate with MTs, affecting their organization, stability, and growth dynamics. Two important types of proteins which we will discuss in detail here include motor proteins and
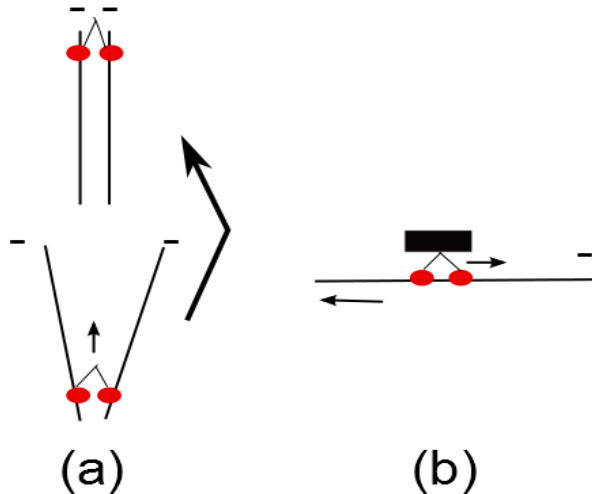
Figure 1.3: Motor interactions with MTs. (a) MT alignment by a motor protein. (b) MT sliding by static motor.

microtubule associated proteins (MAPs) [28, 65].

Motor proteins are ATPases, and so are driven by the hydrolysis of adenosine triphosphate (ATP). ATP hydrolysis is the reaction by which chemical energy that has been stored and transported in the high-energy phosphoanhydridic bonds in ATP is released, where the product left over is adenosine diphosphate (ADP). By transforming chemical energy into work, they are able to walk along MTs, carrying important proteins (at their cargo domain) around the interior of the cell.

Motor proteins can affect MT organization in a number of ways; however, here we assume that the two primary ways they do so are by (1) helping to align MTs parallel with one another [44, 58], and (2) by aiding in MT directed transport (MT sliding) [19, 57]. MT alignment occurs when motor proteins are attached (or cross-linked) to two MTs simultaneously. As they walk along MTs (either towards their positive end or negative end), they produce pushing and pulling forces that help to reorient the MTs (see Figure 1.3(a)). MT sliding occurs when a motor is attached (absorbed) to a non-moving substrate at its cargo domain, where their free legs are able to attach to a MT. Since the motor remains stationary, it effectively pushes the MT along its own axis as it walks along it. Such a sliding mechanism has been used in *in vitro* experiments, when the cargo domain of a motor is absorbed to a slide or coverslip [69, 15](see Figure 1.3(b)). A mathematical description of such a motion is similar to MT

6
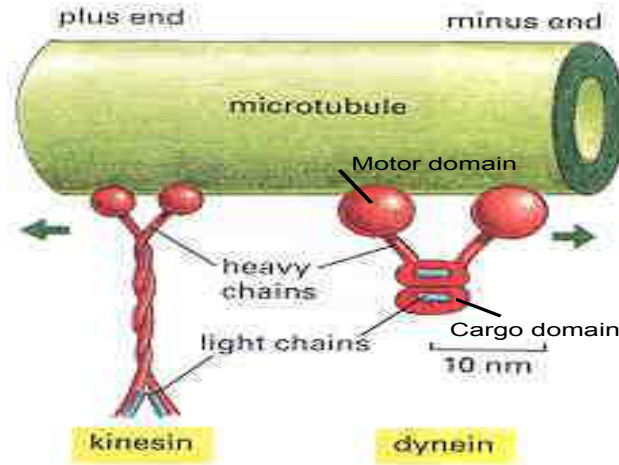
Figure 1.4: A dynein and kinesin motor attached to a microtubule. Picture taken from [**?**].

treadmilling in that both types of motion describe directed movement of MTs along their axis. The only difference is that MT treadmilling can occur when motors are not present (MT sliding requires motors).

MTs are associated with two main families of motor proteins, kinesin and dynein (see Figure 1.4) [28, 65]. Kinesin, also referred to as a positive-directed motor, moves towards the plus end of MTs and is comprised of two heavy chains that wrap around each other in the central stalk region (an alpha-helical coiled-coil domain). One end of each heavy chain is attached to the MT, while the other end is connected to the cargo domain, which is comprised of protein light chains. Dynein, a negative-directed motor, moves towards the minus end of a MT and is comprised of two heavy chains with globular heads that attach to the MT. Two stalks connect the heavy chains to light chains located at the motor's cargo domain.

There are a number of important motor properties that determine the extent to which MT alignment and sliding aid in MT reorganization. These properties include the speed of the motor, the ability for the motor to attach to two MTs simultaneously (to cross-link), motor concentration [57, 19, 59, 58], and the kinetics (processivity) of the motor (the rate at which a motor attaches/detaches from a MT). Processive motors are able to walk along MTs for long periods of time, while non-processive motors may only walk along MTs for short periods of time, or not at all. In Section 1.4, we describe how

7

differences in these motor properties have been found to alter MT organization *in vitro*.

MAPs are another type of protein that interact with MTs [28, 65]. Many of these proteins identified to date are found in neural tissue, however there are a small number that have been found to have widespread cellular distribution. Examples of MAPs that have widespread distribution include MAP3 and MAP4, while other MAPs, including MAP1, MAP2, and tau, are only found in neural cells.

In general, MAPs have a number of different important functions. For example, some MAPs help MTs to form bundles by forming cross-bridges between MTs, while others increase MT stability, alter rigidity, or influence the rate of assembly. Three well studied MAPs isolated from the brain, MAP1, MAP2, and tau, are thought to be involved in stabilizing MTs against dynamic instability. Although these proteins play a role in organizing MTs, we will not include them in our model efforts.

1.3 Microtubule organization *in vivo*

In the previous sections, we have described how single MTs are structured, as well as some of the important proteins that interact with them. We also described some of the important types of dynamics that single MTs undergo. However, to fully understand MT function within cells, it is not only important to understand how single MTs behave, but also how groups of them interact and how they are organized within a cell. We will review general MT organizations in Section 1.3.1, and describe in detail those that will be of particular interest in this thesis in Section 1.3.2.

1.3.1 General organizations of MTs

MTs organize into different structures depending on the cell-cycle stage, as well as the cell type [29, 56, 66]. Three primary cell-cycle stages are cell growth (G1 and G2), interphase (S), and mitosis (M) [28]. Also cells can enter a resting phase (G0), called quiescence. Most cells that are in a quiescent stage, as well as cells that are in interphase (non-dividing stage), have MTs that take on

a centrosomal configuration (an astral configuration of MTs), similar to that shown in Figure 1.5(a). During interphase, DNA is replicated and MTs grow from the centrosome (where they are also nucleated). MTs are anchored at the centrosome by their negative ends [28]. As MTs grow from the centrosome by addition of tubulin dimers at the positive end of the MT, they organize into a single aster that helps to provide structural support for cells, as well as to provide a means to transport important proteins from the center of the cell to the cell surface (via motor proteins).

In contrast, during mitosis, MTs reorganize as the cell prepares to divide [28]. During mitosis, chromosome alignment and segregation depends primarily on interactions between the cells kinetochore and the mitotic spindle. The mitotic spindle is composed of a tight bundle of MTs located at the cells dividing center (see Figure 1.5(b)), and the kinetochore is a proteinaceous chromosome component located at the center of the mitotic spindle. Along with the MTs associated with the mitotic spindle, two asters of MTs exist at the poles of the cells, being centered at the two replicated centrosomes.

MTs not only take on different configurations during various stages of the cell cycle, they also take on different configurations depending on the cell type [29, 56, 66]. A common type of motile cell, called a fibroblast, takes on a centrosomal-type configuration of MTs (see Figure 1.5(a)) [28]. These cells group together and are a type of connective tissue cell that secrete collagen and other components of the cells extra cellular matrix (ECM). Since fibroblasts are motile cells, they can move around, and so can proliferate and migrate during wound healing and in tissue culture.

Other types of specialized cells, such as skeletal muscle cells, neurons, and epithelial cells, contain large numbers of non-centrosomal MTs [29]. Such non-centrosomal organizations are essential for these cells to carry out their specialized activities. For example, in neuronal cells, MTs are organized in parallel arrays along the length of the cell axon, with their negative ends directed towards the centrosome [29, 35]. Such a configuration allows for long-distance transport of proteins and vesicles along the axon (via motor proteins) that would not be possible for a single centrosomally located MT to achieve on its own [17]. In cylindrical shaped polarized epithelial cells (e.g., cells of the liver, intestine, kidney and cochlea), MTs are aligned parallel to the baso-
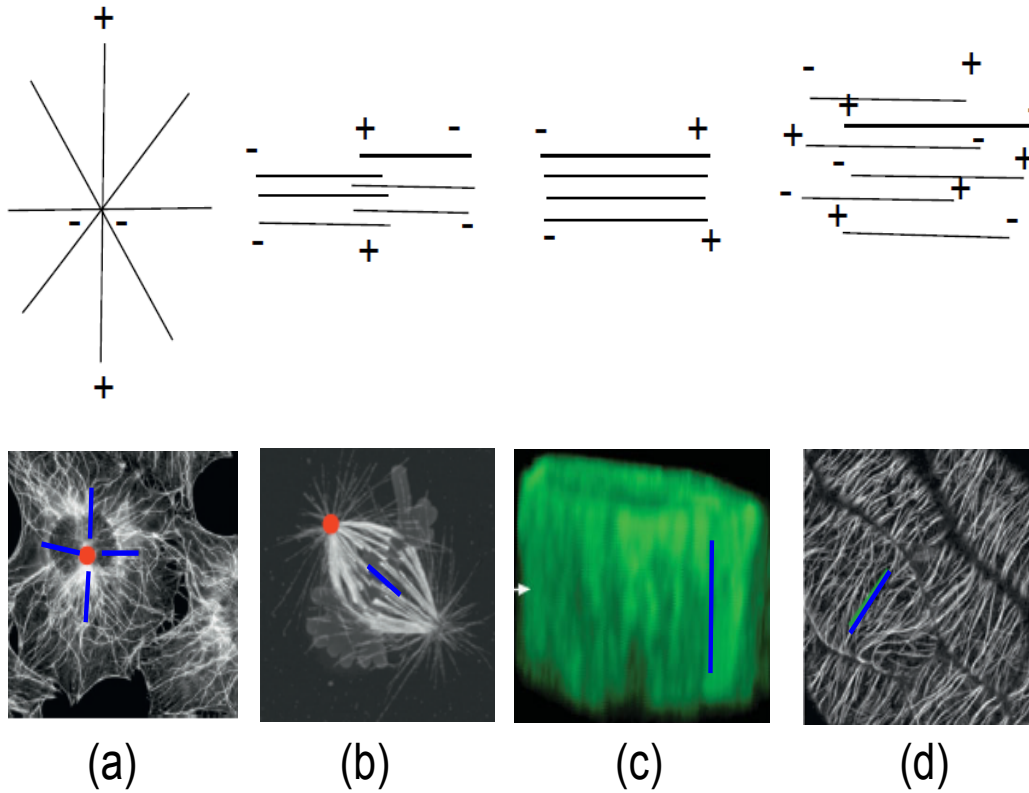
Figure 1.5: MT organization *in vivo*. Top row shows schematics while bottom row shows images taken from real cells. Images (a), (b), and (d) show images of black and white pictures in fluorescent labeled MTs [11], and image (d) is a 3D reconstruction based on confocal optical sections using transition electron microscopy [4]. The blue line shows the MT orientation. (a) Centrosomal configuration of MTs in cross-section of a fibroblast. MTs are in an aster configuration and are anchored at their negative ends at the cells centrosome (shown in red). (b) MT configuration in cross-section of a typical dividing cell. Two asters of MTs are located at the spindle poles, centered at the replicated centrosomes, while an anti-parallel bundle of MTs, referred to as the mitotic spindle, is located at the cell center. (c) A polarized MDCK cell showing a distinct peripheral apico-basal parallel MT array. (d) MT organization in a plant cell. MTs are arranged in a mixed parallel bundle.

lateral walls of cells with their negative ends anchored at the cells adherens junction (AJ), and their positive ends located at the basal surface (see Figure 1.5(c)). Such a configuration allows for vectorial transport of proteins between the apical and basal domains via MTs, as well as polarized sorting of membrane components [5, 29, 41].

Although there is much information regarding the static organizations that MTs can take on, a description of how MTs move between these configurations is incomplete. For example, it is not fully understood how MTs move between a centrosomal configuration shown in Figure 1.5(a) to the configuration shown in Figure 1.5(b) during cell division. Also, in some types of specialized cells, such as columnar epithelial cells described above, MTs move from a centrosomal configuration when epithelial cells are not polarized (when cells are not connected to one another) to a polarized configuration as shown in Figure 1.5(c)(when cells adhere to one another).

1.3.2 *In vivo* MT/motor systems of interest

In this thesis, we will focus on a variety of MT organizations found in cells. Three examples we consider include MT organizations associated with the cell-cycle stages of cell interphase, cell division, and the MT organization associated with polarized neurons. In particular, we will provide insight into how negative-focused asters are established and maintained, similar to organizations formed during cell interphase (as shown in Figure 1.5(a)) and at the spindle poles of dividing cells (as shown in Figure 1.5(b)). We will also describe how anti-parallel organizations of MTs can be formed, similar to the organization of MTs of the mitotic spindle (as shown in Figure 1.5(b)). Also, we describe how parallel bundled organizations of MTs are formed, similar to those found along the axons on neurons. As stated earlier, we will focus on how these organizations arise in systems comprised of only motor proteins and MTs.

In interphase and during cell division, the motor protein cytoplasmic dynein, a processive, negative-directed motor, has been shown to be involved in the establishment of radial MT arrays. In particular, during mitosis, dynein activity is required for the tethering of MTs at spindle poles [55]. Also, in interphase

cells, dynein activity has been found to prevent the loss of MTs from their radial array, as well protecting them (the MTs) from disruption [8].

In dividing cells, it has been proposed that mitotic spindle formation and movement can be explained by a sliding filament mechanism [55, 26]. That is, a mechanism by which certain cross-linking motors attach to two MTs simultaneously and slide MTs anti-parallel to one another. A number of mitotic motors have been discovered, and it is believed that the slow moving, positive-directed, weakly processive motor (kinesin-5), along with an opposing negative-directed motor, act between overlapping MTs to form these anti-parallel arrays. Kinesin-5 is able to form cross-links and has been found to slide MTs relative to one another. A possible candidate for the opposing negative-directed motor is kinesin-14 (commonly referred to NCD). Such a motor is very fast, but not processive. However, such a motor stably anchors itself along one MT and is able to generate force (non-processively) along a second MT, aiding in MT bundling.

In neurons, forces involved in axonal extension are unclear. However, it has been found that the fast, processive, positive-directed motor protein, kinesin-1 (also called conventional kinesin), may help provide the force for axonal growth by aiding in the sliding of MTs. Recall, as described above, that the axon of neurons is composed of very tight bundles of parallel MTs [23]. Other proteins, such as cytoplasmic dynein and kinesin-5, are found in neurons, although their roles are not entirely understood. Some studies suggest that these proteins are associated with retrograde and anterograde transport of vesicles and short MTs, respectively [18]. Also, other studies have shown that kinesin-5 is able to cross-link MTs and aid in MT sliding [26].

1.4   Microtubule organization *in vitro*

In an effort to understand how MTs reorganize in cells, a number of *in vitro* (and *in situ*) experiments have been conducted to examine the types of MT patterns found in systems comprised of only MTs and motor proteins [63, 59, 40, 51, 43, 44, 58, 19]. Such studies show that, depending on MT and motor properties, as well as the size and shape of the boundary, various MT patterns, such as those described in Figure 1.6, can be found. Some of
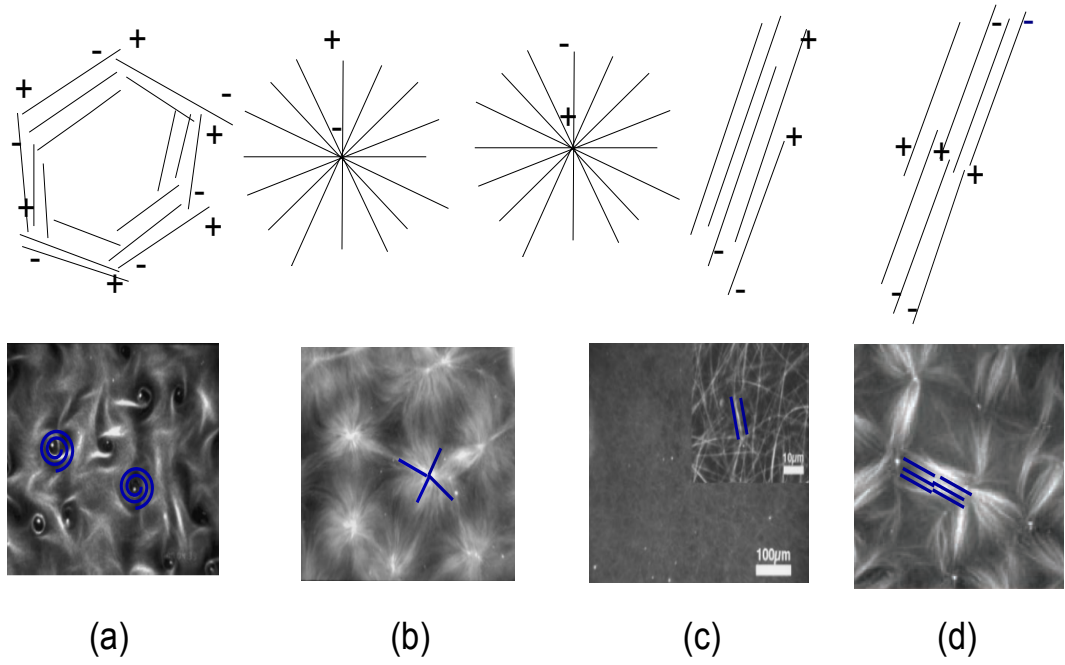
Figure 1.6: MT patterns organized *in vitro* by the action of multimeric motor complexes. MTs are visualized using dark-field microscopy [58]. Top row shows schematics while bottom row shows images taken from experiment. Blue lines represent MT orientation. (a) Vortices, (b) negative and positive-focused asters, (c) bundles, (d) and anti-parallel bundles.

the first MT patterning experiments, completed in the early 1990s, were gliding assays [63], comprised of both positive and negative-directed immobilized motors and moving MTs. These experiments show how anti-parallel bundles of MTs can form *in vitro* when motors of opposite directionality interact with freely moving MTs (see Figure 1.6(d)).

Newer experiments (late 1990s-present) have looked at MT patterning in systems comprised of MTs and moving motors [43, 44, 58, 19]. Some studies consider one motor type [43, 44], while others consider two (two motor types with different directionality) [58, 19]. A well-known study of MT/motor organization using a single type of moving motor is that by Nédélec *et al.* [44]. This study highlights the dependency of motor concentration on MT patterning. In particular, this study shows that, depending on the motor concentration, a variety of patterns including vortices, asters, and bundles can be formed. MT patterns are formed by uniformly mixing stabilized MTs (stabilized by Taxol) and kinesin motors in very large (quasi)-2-dimensional domains. Different patterns are obtained by varying the motor concentration. For low

13
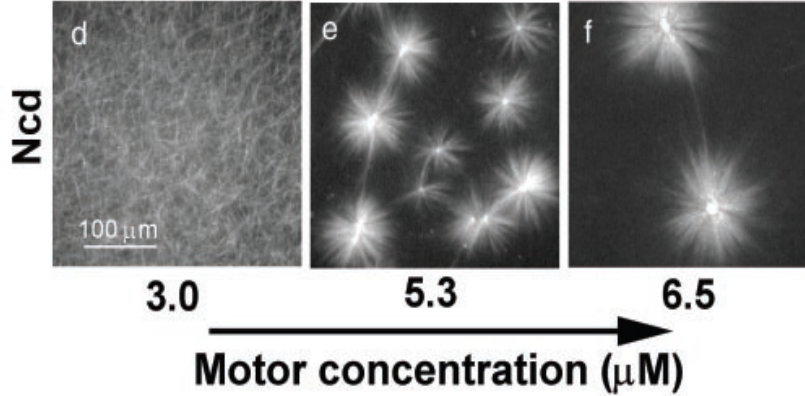
Figure 1.7: MTs form asters in mixtures with a processive NCD motor construct. MTs are visualized using dark-field microscopy [58].

motor concentrations ($< 15\mu g/ml$ kinesin), vortices are found (as in Figure 1.6(a)), for low-medium motor concentrations ($\sim 25\mu g/ml$ kinesin), mixtures of asters and vortices are found, and for medium-high motor concentrations ($\sim 37.5\mu g/ml$ kinesin), lattices of just asters are found (as in Figure 1.6(b)). Finally, for very high motor concentrations ($\sim 50\mu g/ml$ kinesin), MT bundles are found (as in Figure 1.6(c)).

Other studies by Surrey and Nédélec *et al.* have described the importance of motor processivity, motor speed, and motor directionality on MT patterning [58]. In particular, MT patterns formed using positive-directed motors are different from those which use negative-directed motors. In mixtures of MTs and NCD motors (negative-directed motors), negative-focused asters are formed at moderate and high motor densities (as in Figure 1.7), while in mixtures of MTs and positive-directed motors, vortices are formed at moderate motor densities and positive- focused asters are formed at high motor densities (as in Figure 1.8).

Another important consideration in the study of *in vitro* MT patterning is boundary constraints. In particular, some cells are very large (with cross-sections on the order of $100 \times 100 \ \mu m^2$), while others are very small (with cross-sections on the order of $10 \times 10 \ \mu m^2$), and so the size and shape of the boundary used in experiments is an important feature that should be analysed. A recent study by Vignaud *et al.*[64] suggests that local effects occurring at the boundary of a cell can propagate long distances throughout the entire
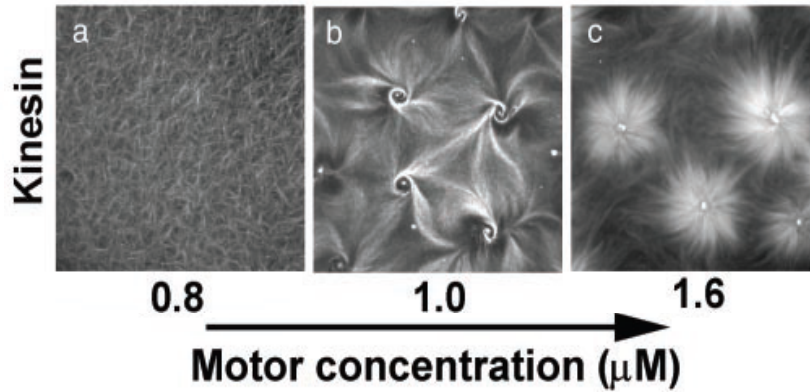
Figure 1.8: MTs form vortices in mixtures with medium concentrations of kinesin motors, and asters in mixtures with higher concentrations of motors. MTs are visualized using dark-field microscopy [58].
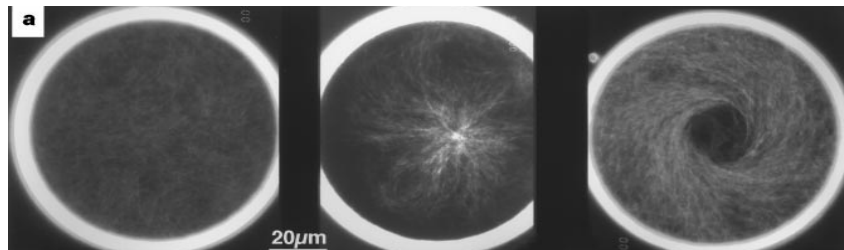
Figure 1.9: Self-organization in constrained geometry of micro-fabricated chambers etched in glass [44]. MTs observed by dark-field microscopy. MTs form asters, but buckle at the boundary when they grow long enough and form vortex patterns.

MT network, changing the qualitative organization of MTs. An example of a study that has explored the importance of boundary constraints on overall MT patterning is that of Nédélec *et al.* [44]. Here, the author describes the effect of confined geometries on MT patterns (see Figure 1.9). In smaller domains, asters initially form. However, as MTs grow and reach the boundary, they begin to buckle and the system breaks down into a global vortex pattern.

1.5 Unregulated MT organization

One question that arises when studying MT organization is, what happens when MT organization is altered? One major area of study that addresses this question is epithelial to mesenchymal transition (EMT), as a step in cancer progression [33, 62, 61]. EMT occurs when polarized epithelial cells lose their

polarization and adhesive characteristics, to become mesenchymal cells, cells that are non-epithelial with migratory characteristics that are loosely embedded in the extracellular matrix. EMT occurs naturally in many developmental processes. For example, in vertebrates, it is required for the formation of neural crest cells, which delaminate (split) from the dorsal-most region of the neural tube. However, EMT is also a key step in the metastasis of many different kinds of cancers. In particular, this happens when polarized epithelial cells of a cancerous tissue lose their polarization and adhesive characteristics and break down the extracellular matrix, migrating and eventually gaining access to the circulatory system. There are a number of steps involved in EMT, where one of the main steps involved is the reorganization of the cytoskeleton [33]. In particular, studies have shown that MTs (and not actin) are necessary for basement membrane stabilization. When MT dynamics are altered, so that they move from their bundled configuration as in polarized epithelial cells, the basement membrane becomes unstabilized and the cells become motile.

1.6   The Thesis Overview

The goal of this research project will be to address the topic of MT organization. In particular, we develop an integro-partial differential equation (PDE) model to describe how MTs and motor proteins evolve through space and time as they interact with one another.

As stated above in Section 1.2, there are many proteins that interact with MTs. However, in this project, we will only look at the behavior of MTs as they interact with motor proteins. We do this for a number of reasons, the first being that it is easier to construct a model with only two interacting components as opposed to many interacting components. Also, from the experiments of Nédélec *et al.* [58], it is known that MTs can reorganize into many different varieties of patterns in systems comprised of only MTs and motors. Finally, it is interesting to focus on the importance of motors in the reorganization process since motors have been found to be a key contributor to MT reorganization *in vivo*, as described in Section 1.3.2.

We will develop our model by assuming that MT pattern formation (organization) is governed by one of two mechanisms: treadmilling and motor

protein action. Recall from the sections above that treadmilling accounts for movement of a MT along its axis, with constant speed, and motor proteins can reorient MTs when they crosslink two MTs simultaneously and walk along them. Later, in the future work section of Chapter 8, we will describe some modeling ideas to incorporate MT dynamic instability into our model.

To begin addressing the question of how MTs reorganize in the presence of motor proteins, we give a detailed description of previous modeling efforts in Chapter 2. Such modeling efforts will be useful tools when constructing our model, which is outlined in Chapter 3. In particular, for our model, we will make use of some of the older models that have been developed, as well as make some novel extensions of our own.

In Chapters 4 and 5, we describe results of a simplified version of our model. In particular, we study the evolution of MTs under the influence of stationary distributions of motors. In this case, the model is simplified to a well-studied transport type (Bolzmann) equation for MT movement, and is analogous to gliding assays [63] (experiments where motors are absorbed to slides).

In Chapter 4, we describe results of the transport model under further simplifications. In particular, we describe long-term MT patterning when MTs do not treadmill, and show how MT patterns evolve when influenced solely by motor cross-linking capability. When MT cross-linking capability is high, MTs form bundles, and when it is low, MTs form asters. Also, in this Chapter, we describe the parabolic scaling of the transport model. Such a model describes the types of MT patterns that form when MT treadmilling is slow, but MTs switch orientation (due to their interactions with motor proteins) very quickly, and results in a diffusion-type equation for MT movement.

In Chapter 5, we describe results of the full transport model using either periodic boundary conditions or a novel bounce back boundary condition (described in detail in Section 3.4). Here, directed MT transport is not only a function of MT treadmilling, but is also a function of MT sliding. We show that, for non-processive motors (when directed motion is only a function of MT treadmilling, and not sliding), MTs form vortices when MT cross-linking capability is low and motors are located on the boundaries. MTs can only change orientation on the boundaries if motors are located there. If there are no motors on the boundaries, all MTs eventually end up on the boundaries.

For non-processive motors, we also show that MTs are able to form bundles when cross-linking is high. For one type of negative-directed processive motor, we find similar results (negative-directed motors cause sliding to occur in the same direction as treadmilling). When we include two types of processive motors (motors with opposite directionality), we find a larger variety of patterns are able to form. In particular, using periodic boundary conditions, in systems of slow moving, negative-directed motors, and fast moving, positive-directed motors, if cross-linking capability is high, a single aster forms. If cross-linking capability is low, arrays of vortices form. Also, using bounce back boundary conditions, and two types of opposing processive motors, we find arrays of anti-parallel bundles. This result is similar to that found in gliding assays [63, 59, 19]

In Chapters 6 and 7, we show results for the full model for MT evolution. Here, motors are able to move. First, in Chapter 6, we develop a novel existence and uniqueness result for the full model, which is based on Banach's Fixed Point Theorem [52]. Then, in Chapter 7, we describe numerical results for the full model. Here we show that the MT patterns found are different from those that are found in Chapter 5. We consider three classes of motors: processive, weakly processive, and non-processive, and use model parameters that represent each motor type when running simulations. We find for fast moving, processive, negative-directed motors, arrays of asters form in low to high motor density systems, similar to results found from experiment [58]. Also, for slower moving, processive, positive-directed motors, arrays of vortices are able to form in low density motor systems. This result is also similar to that found in experiment [58].

Finally, in Chapter 8, we discuss the conclusions of our model, as well as give a description of interesting ideas and questions that can be explored in future studies. In particular, we discuss not only the successes of our model, but we also examine limitations and describe how we can go about making our model better at predicting MT patterns.

Chapter 2

Previous Modelling Efforts

In the previous chapter, we gave an introduction to many of the important concepts regarding MTs and their organization. We described MT structure, as well as organization, and described briefly how MT structure and organization are related to their function. One of the important questions that arose from this discussion was how MTs reorganize within cells. In particular, what are the contributing mechanisms involved in reorganizing MTs from one configuration to another during the cell-cycle stages and within various cell types?

In this chapter, we describe an overview of present literature that provides an explanation of some of the mechanisms that contribute to MT patterning both *in vitro* and *in vivo*. Such literature describes a variety of models including experimental, computational, as well as theoretical. Many of these models have been successful in capturing important qualitative features of MT patterning. However, many models are overly simplified and do not provide detailed insights into the underlying biology of how MT dynamics and motor proteins affect MT organization. The goal of this chapter will be to describe some of the previous modelling efforts, and to outline the successes and limitations of these past models. In the next Chapter, Chapter 3, we use this information to piece together a framework for the development of our own theoretical model.

2.1 Models of dynamic instability

It is well known that MT dynamic instability plays a role in MT patterning [10, 16]. The first experiment to capture the unique behavior of dynamical instability was completed by Mitchinson and Kirschner in 1984 [31, 39]. In this experiment, the authors examined MTs nucleating from the centrosomes of fibroblastic-type cells (cells that take on a centrosomal configuration in interphase as in Figure 1.5(a)) and found that two distinct populations of MTs co-existed. In particular, they found that below a critical concentration of free tubulin ($\cong 14\mu M$) some MTs were found to shrink while others grew, although the total MT polymer mass decreased. Above this critical value, they found that MTs grew and that the total polymer mass increased. The type of behavior exhibited by MTs at low free tubulin concentration has only been observed in MTs. They coined this behavior dynamic instability (see Figure 1.2).

Not only are populations of growing and shrinking MTs found in cells that take on a centrosomal configuration in interphase (as in the Mitchinson and Kirschner experiment), but they are also found during other cell-cycle stages, where MTs are not in a centrosomal configuration. An example of this is during cell division, when astral MTs (those MTs that are centered at the spindle poles, radiating out towards the cell periphery) elongate, while MTs of the mitotic spindle attach to the cell's kinetochores and shorten [36]. Kinetochores are centromere-based protein complexes that attach to MT positive ends at the center of the mitotic spindle. As the spindle MTs shorten, the kinetochores help to capture and transport chromosomes to opposite cell ends [36].

One of the first computational models developed to describe dynamic instability of MTs was developed by Hill and Chen [20]. Hill and Chen used Monte Carlo kinetic simulations to describe dynamic instability at the extreme tip of a MT. They called their model the 'cap' model. The word 'cap' comes from the resulting behavior found from simulations. In particular, they found that below a critical concentration for tubulin ($\cong 2\mu M$), MTs exist in either one of two phases, capped (by GTP) or uncapped. In the capped phase, the MT grows (with a fluctuating size in cap), and in the uncapped phase the MT quickly collapses. Although this model is useful at capturing the qualitative

description of MT dynamic instability found in experiment, it does not give a realistic quantitative description. In particular, from these simulations, a critical concentration of $\cong 2\mu M$ was found, as compared to the experimental value of $\cong 14\mu M$ found by Mitchinson and Kirschner [31].

One of the first theoretical models describing the importance of dynamic instability in MT patterning was proposed by Dogterom and Leibler [10]. The goal of the authors was to describe how the length distributions of MTs evolved in systems of non-interacting, growing and shrinking, MTs. An example of such a system found *in vivo* is one where MTs are organized radially (as in Figure 1.5 (a)). In this configuration, MTs remain static at their negative ends and dynamic at their positive ends. The model describing the evolution of growing and shrinking MT densities of length x at time t, given by $G(x,t)$ and $S(x,t)$, respectively, is

$$\frac{\partial G}{\partial t} + \gamma_g \frac{\partial G}{\partial x} = \nu_R S - \nu_C G, \tag{2.1}$$

$$\frac{\partial S}{\partial t} - \gamma_s \frac{\partial S}{\partial x} = \nu_C G - \nu_R S. \tag{2.2}$$

The parameter γ_g is the MT growth rate, γ_s is the MT shortening rate, ν_C is the frequency of catastrophe, and ν_R is the frequency of recovery for a MT.

Through numerical simulation of the model, using semi-infinite boundary conditions, Dogterom and Leibler found that the resulting system displays unbounded growth of MTs for certain parameter ranges, as well as bounded, exponentially decreasing MT length distributions for other parameter ranges [10].

Other models, such as that by Bolterauer *et al.*, have also shown exponentially decreasing length distributions [6]. Also, recent extensions to Dogterom's model, that include a more biologically realistic bounded domain (i.e., using closed boundary conditions), show similar results [16]. In particular, like Dogterom, the model of Govindan *et al.* describes exponentially increasing length distributions for certain parameter ranges, and exponentially decreasing length distributions for other parameter ranges. The only difference between the models of Dogterom and Govindan is that distributions always remain bounded when using closed boundary conditions, as in Govindan's model.

2.2   Models of MT treadmilling

Other experiments show that MTs, like many other polymers, undergo tread-milling both *in vivo* and *in vitro* (see Figure 1.2) [38], and that treadmilling can play a major role in MT patterning. In particular, in studies of fish melanophor fragments, short MTs, nucleated by pigment granules, are found to be transported through the cytoplasm of cells by treadmilling leading to astral configurations [53]. Also, as epithelial cells polarize, MTs move between a centrosomal configuration, to one where MTs align parallel to the apico-basal surface of the cell (described in Figure 1.5(c)). It has been hypothesized that MT reorganization during polarization is aided by MT treadmilling [29].

Recently, Allard *et al.* have developed a computational model to describe the spatial and temporal organization of cortical MTs in plant cells [1]. In such systems, many MTs have free negative ends so that they can treadmill at the cell cortex. During cell elongation, MTs predominantly orient transverse to the elongation axis (as in Figure 1.5(d)). Using the key assumption that MTs treadmill, Allard was able to predict MT patterns that are similar to those found in real plant cells. In particular, Allard showed that MTs form parallel (and dispersed) arrays of MTs that align transverse to the axis of elongation of the plant. Also, computational studies completed to describe the astral patterns of MTs found is fish melanophore, have found that nucleation of MTs and MT treadmilling is sufficient to form asters within a confined geometry [37].

In fish melanophore cells, pigment granules aggregate to the center of cells via dynein motor transport along MTs. As stated above, MTs are organized in a centrosomal fashion (as in Figure 1.5(a)), so that when granules aggregate to the center of a cell along MTs, only a single spot of color is found at the center of each cell. Pigment granules are signalled to aggregate to the center of cells along MTs when a fish requires camouflage from predators [42]. Recently, a 1-dimensional theoretical model ($-L < x < L$), given by equations (2.3) through (2.6), has been developed to describe how these aggregates form in melanophore fragments (such fragments do not contain a centrosome) [9].

$$\frac{\partial p_{r,l}}{\partial t} = \pm v_p \frac{\partial p_{r,l}}{\partial x} + n(g) \tag{2.3}$$

$$\frac{\partial m_{r,l}}{\partial t} = \pm \frac{\partial(v(g)m_{r,l})}{\partial x} + n(g) \tag{2.4}$$

$$\frac{\partial g_{r,l}}{\partial t} = -k_{off}g_{r,l} + k_{on}N_{r,l} \mp v_g \frac{\partial g_{r,l}}{\partial x} \tag{2.5}$$

$$\frac{\partial g_s}{\partial t} = k_{off}(g_r + g_l) - k_{on}(N_r + N_l)g_s. \tag{2.6}$$

Such equations are used to track the spatial and temporal evolution of right and left moving positive densities $p_{r,l}(x,t)$, and right and left moving negative densities $m_{r,l}(x,t)$ of MTs through space x and time t. Here, right (left) orientations correspond to negative ends located to the right (left) of the positive ends. The variable $g_{r,l}$ is the local concentration of the right- and left- moving granules, respectively, and g_s is the local concentration of the static granules (those that are not attached to MTs). The first term on the right-hand side of the equations (2.3) and (2.4) describes advection of positive ends at a constant rate v_p and of negative ends at a rate $v(g)$ (and is thus used to describe treadmilling). The second terms describe nucleation with a rate $n(g)$. Equations (2.5) and (2.6) are used to keep track of the density of pigment granules $g(x,t)$ at each point in space and time (here, $g = g_s + g_r + g_l$). The last term in equation (2.5) describes the gliding of the granules along MTs with speed v_g. The first terms in the equations (2.5) and (2.6) are responsible for the dissociation of the granules from the MTs with the constant rate k_{off}, while the second terms describe the attachment of the static granules to the MTs at a rate k_{on}. The rates of attachment to the right- and left-oriented MTs are proportional to the corresponding MT polymer densities, $N_{r,l}(x,t)$.

2.3　Models of MT-motor interaction

In the last two sections, we described how MT dynamic instability, as well as MT treadmilling, contribute to MT organization. Both these mechanisms are important in describing how MTs can change length, as well as how they can be transported in one direction through a cell, respectively. However, they do

not explain how MTs can change orientation within a cell. Here we describe the mechanism of motor protein action on MTs. Such a mechanism provides an explanation for how MTs can change orientation within cells.

Recent experiments have provided evidence that simple systems consisting of only motor proteins and MTs are enough to construct patterns such as asters, bundles, and vortices (see Figure 1.6) [44, 43, 58]. Recall from the previous section, that asters are found in dividing cells, as well as cells in interphase (Figures 1.5(a) and (b)). Also, bundles are found in dividing cells (i.e., the mitotic spindle shown in Figure 1.5(b)). However, vortices are not found in nature.

In vitro experiments show that MT patterning is dependent on motor type. In particular, MT orientation can be affected by motor directionality [63, 59], processivity [19], motor speed [19], as well as the time a motor spends at the MT end. Also, MT patterning is affected by motor concentration [58].

Studies highlighting MT patterning in systems of MTs and motors, where motors have different directionality, date back to the early 1990s [63]. During this time, gliding assays were completed to better understand the overlap of antiparallel MTs in the mitotic spindle. These experiments involve using immobilized motors (absorbed on a coverslip), where it is proposed (from lose-of-function experiments) that the anti-parallel structure is a result of balanced activities of motors with opposite directionality. In particular, such structures require two types of motors (each with different directionality). For example, in an early gliding assay completed by Vale *et al.* [63], the author uses an artificially constructed kinesin-1 motor (positive-directed), and cytoplasmic dynein. To test whether or not naturally occurring motors could be used to obtain more biologically realistic results, a recent study by Tao *et al.* [59] use both naturally occurring mitotic motors kinesin-14 (negative-directed motor also referred to as NCD) and kinesin-5 (positive-directed). In both studies, anti-parallel structures form, however, these structures are not stable.

In the gliding experiments described above, motors are immobile. In real cells, motors are able to move freely within the cell. To test whether new MT patterns would be observed with moving motors, a recent study involving the naturally occurring mitotic motors kinesin-14 and kinesin-5 was completed by Hentrich and Surrey [19]. Such results show how motor processivity and

24

motor speed affect MT patterning. Similar to the gliding assays described above, results show that anti-parallel MT patterns do exist in such a system. However, results also show that kinesin-14 is able to focus MTs into asters, whereas the kinesin-5 is not [19]. The reason for this has to do with the different properties of each motor. In particular, kinesin-5 moves at rates between $0.01 - 0.04 \ \mu m/s$, while kinesin-14 moves much more quickly at rates approximate to $0.1 \ \mu m/s$ [59]. Also, the kinetics of kinesin-14 are found to be very fast, whereas those of kinesin-5 are not [19]. That is, kinesin-14 attaches and detaches from MTs very quickly, and as a result is not processive (kinesin-5 is found to be weakly processive).

Before the studies of Hentrich and Surrey [19], similar studies describing MT patterning in the presence of freely moving motor proteins were completed using artificially constructed motors [44, 58]. In these studies, it was found that artificially constructed NCD was able to form negative-focused asters at medium and high motor concentrations, whereas a positive-directed oligomeric kinesin was able to form vortices at moderate motor concentrations, and positive-focused asters at higher concentrations. In this experiment, the motors forming only asters were highly processive and had long residence times at MT ends.

Over the past few decades, both local and non-local theoretical models have been proposed to describe how MT patterning occurs in systems comprised of motor proteins and MTs. In general, MT gliding can be described by advection (directed movement), placing these models in the category of transport-type models. Transport type models are defined as models where the particles of interest are defined by their position in space, time, and velocity [49]. Defining a model as local or non-local generally has do to with the redistribution part of the model, in our case this corresponds to MT reorientation (governed by motor proteins). Most models of MT evolution describe MT reorientation using local diffusion-type terms [30, 32, 24]. For example, the model of Lee and Kardar [32] suggests that MTs undergo small reorientations in the presence of motor proteins. However, we know from recent *in vitro* studies that large reorientations are possible [44, 43], and so non-local models (models that use integral terms to describe MT angular redistribution) are more desirable from a biological perspective. Such non-local models that describe redistribution in

terms of probabilities are referred to as velocity-jump models [45], and have a rich history in the study of large-scale animal movement governed by certain cues that can exist over large distances [46]. More recently, such models have been used to describe the evolution of cellular systems [21]. An interesting example of such a model used in MT/motor systems is a recent study by Aranson and Tsimring [2]. This model uses a diffusion term (to describe small scale fluctuations of MTs in the absence of motors), but also includes a non-local term to describe alignment of MTs as they collide with one another. The action of the motor proteins is implicit here, and suggests that motors are dispersed uniformly throughout space, so that when two MTs interact they instantaneously align due to motor protein action. Below we describe the model of Lee and Kardar [32] and Aranson and Tsimring [2] in detail.

Model 1: A first model that describes MT patterns formed by interacting MTs and motors is a partial differential equation (PDE) model by Lee and Kardar [32]. Such a model, given by equations (2.7) and (2.8), describes the time and spatial evolution of MT orientations $(\vec{T}(x,t))$ in the presence of motor proteins $(m(x,t))$.

$$\frac{\partial m}{\partial t} = \nabla^2 m - \vec{\nabla} \cdot (m\vec{T}), \tag{2.7}$$

$$\frac{\partial \vec{T}}{\partial t} = C\vec{T}(1 - T^2) + \vec{\nabla} \cdot (m\vec{\nabla}\vec{T}). \tag{2.8}$$

The equation for motor protein evolution, given by equation (2.7), states that motors diffuse freely in the absence of MTs, but are transported along the orientation of MTs (at a density dependent rate) when in the presence of MTs. The first term in equation (2.8) states that, in the absence of motors, MTs grow at a constant rate C when they are short, but are then stabilized at unit length (potentially representing their stabilization by the MT stabilizing drug Taxol [71]). The last term in equation (2.8) describes the reorientation of MTs by motor proteins. It is a diffusion-like term and describes random fluctuations of the MT orientation in the presence of motor proteins.

An important feature of this model is that it qualitatively describes MT patterns such as vortices, asters, as well as combinations of asters and vortices. In particular, at low motor densities, combinations of asters and vortices are

formed, while at slightly higher motor densities, asters dominate the system. These results are consistent with *in vitro* experimental results [44]. However, at high motor densities, the model predicts only a single large vortex. This result is not observed experimentally. In particular, in experiments, MTs tend to form tight bundles at high motor densities [44]. A second important feature of this model is that it describes how MTs move into configurations such as asters and vortices starting from other configurations. In particular, initially, MTs are dispersed uniformly in space and given random orientations, and over time they form more complex configurations.

Although this model is very useful in describing some of the MT patterns that are found in experiment, it also has limitations. One limitation is that reorientations of MTs are described using a diffusion-like term. Diffusion is local, meaning that only small perturbations of MT orientation occur over time. In other words, this model does not take into account larger reorientations that could potentially occur. For example, experiments suggest that MTs can be reoriented over large angular distances in the presence of motor proteins, not just the angles that are closest to its present orientation. To take all possible reorientations into account, it may be useful to use non-local models, such as those involving integral terms [45, 46].

A second limitation of the above model is the description for MT growth. In real cells, MTs are able to grow and shrink (and may or may not be stabilized). Also, in some cases, MTs may undergo dynamic instability and may also treadmill. To make this model more biologically realistic, it might be important to use a different description for MT growth and to include terms that account for MT treadmilling. In this thesis, we include MT treadmilling into our new model. However, we do not include MT growth dynamics (for ease in the mathematical analysis of the model). However, in the last chapter, Chapter 8, we describe a method for including MT growth into our model.

Model 2: A second model that describes MT organization in systems of MTs and motors is that of Aranson and Tsimring [2]. This model is different from the above model because it uses non-local terms to help describe large reorientations of MTs. This is an important feature that is lacking in the previous model of Lee and Kardar. This newer model, given by equation

(2.9), describes the temporal and angular evolution of MT densities $p(t, \theta)$.

$$\frac{\partial p}{\partial t} = \frac{\partial^2 p}{\partial \theta^2} + g \int p(\theta_1)p(\theta_2)[k(\theta, \theta_1, \theta_2)]d\theta_1 d\theta_2. \tag{2.9}$$

Here, p is a function of angle θ and time t and so describes the density of MTs that are located at an orientation θ at time t. The angles θ_1 and θ_2 are orientations of MTs before interaction, and $k(\theta, \theta_1, \theta_2)$, called an interaction kernel, is the probability that MTs interacting at the angles θ_1 and θ_2 will align to an angle θ.

The first term (a diffusion term with diffusion coefficient equal to 1) in equation (2.9) represents small reorientations due to thermal fluctuations, and the second, non-local term represents alignment of MTs caused by a "collision" between MTs that occurs at a rate g. In particular, this model suggests that the interaction between two MTs is described as an inelastic collision that instantaneously aligns two MTs to some mean orientation. The author suggests that it is not actually the collision between MTs that causes realignment, but rather the simultaneous connection between two MTs by motor proteins. In particular, the author is describing the alignment of MTs by motor proteins using physical equations that describe inelastic collisions of particles (like the Bolztmann equation that describes inelastic collisions of gas molecules used in physics (reference)).

Like the model of Lee and Kardar, simulation of this model produces qualitatively similar results to that found in experiment. In particular, the model shows different parameter regimes in which asters and vortices, as well as combinations of the two, are found. Unlike the previous model, this model predicts MT bundling for some parameter regimes. A primary difference between this model and the last is that it does not include spatial variations in MT densities. As well, MT length variation is not taken into account. Also, unlike the previous model, the action of motor proteins is not explicit in the model (they do not consider spatial and temporal changes in motor proteins, but rather consider the action of a homogenous density of motors). Some of these limitations are removed in a later extension of the model completed by Aranson and Tsimring [3]. Such an extension includes spatial variation in MT density, as well as a model that describes the time evolution for bound and unbound

motor densities. When space is included into the model, the only changes to equation (2.9) include a translational diffusion term (MTs can diffuse parallel or perpendicular to their axis), as well as a different reorientation kernel k, which depends on the spatial location of MTs relative to one another, as well as the angular displacement of MTs relative to one another. Inclusion of the motor density evolution ($m(t, x)$) results in equation (2.10),

$$\frac{\partial m}{\partial t} = D\nabla^2 m - \nu\nabla m. \tag{2.10}$$

Here, the first term corresponds to motor diffusion at a constant rate D in the absence of MTs, and the second term corresponds to motor advection at a constant rate ν, along the direction of the MTs. The extended model is more realistic because it accounts for MT location and motor evolution. Analysis of the new model qualitatively describes aster, vortex, and bundling patterns that are found in experiment.

This newer extension to the model given by equation (2.10) is more realistic, because it is able to capture MT patterning found in experiments. However, it still lacks biological realism due to its description of the interaction kernel k. Here, MT interaction is treated as a binary inelastic collision such that only two interacting MTs align along a common axis. In reality, MT reorientation will depend on the interactions of many MTs within a cluster. Also, this model does not describe how patterns can be affected by MT length variation (dynamic instability), as well as MT treadmilling. Both of these dynamics are commonly found in cells and most likely play a role in how MTs are organized [38, 65].

2.4 Summary of successes and limitations in past theoretical modelling efforts

The theoretical models described in the last section do not completely describe MT reorganization in cells. However, each model is successful in capturing some of the important features involved in this process.

For example, the model of Dogterom and Leibler, given by equations (2.1) and (2.2), describe the qualitative length distributions for MTs found in some

cells. In particular, for certain values of the MT growth parameters, exponentially decreasing MT length distributions were found. Also, results for MT organizations found in fish malanophore cells (described by equations (2.3) through (2.6)), show the potential for MT treadmilling as a major contributor in MT organization. Finally, the non-local models for MT organization, described by equations (2.9) and (2.10), were successful in describing the more complex patterns that are found in systems of motors and MTs (patterns like asters, vortices, and bundles).

Although there have been successes in previous modeling efforts, there is no single model that was able to fully describe MT organization. In particular, there is no model that describes how MT patterning is influenced by all three contributions: dynamic instability, treadmilling, and MT/motor interactions, as well as by motor properties such as motor speed, motor directionality, motor processivity, and motor concentration. In the next Chapter, Chapter 3, we develop a model that takes MT treadmilling, MT/motor interactions, and specific motor properties into consideration. In the final Chapter, Chapter 8, we show how to incorporate MT dynamics into the model developed in Chapter 3.

Chapter 3

A New Model for MT Organization

In this chapter, we describe the development of our model for MT organization, which extends and improves on the previously proposed models of Chapter 2. The model components we consider from previous models include

(A) the use of non-local terms to describe large angular displacements of MTs as in equation (2.9),

(B) an explicit description for motor density movement as in equation (2.10), and

(C) an advection-type term to describe MT treadmilling as in equations (2.3) and (2.4).

Later, in Chapter 8 we will also consider

(D) a term that describes MT length variation, similar to the MT growth term from equation (2.8).

In this chapter, we will develop a model that incorporates (A), (B), and (C), as well as adding some new components. The new components we introduce include two equations for motor movement, one for bound motors, and one for unbound motors. These terms are used to describe the two possible states that motors can be in. As well, we introduce an advection term for MTs which depends on the MT direction in 2D (equations (2.3) and (2.4) describe advection
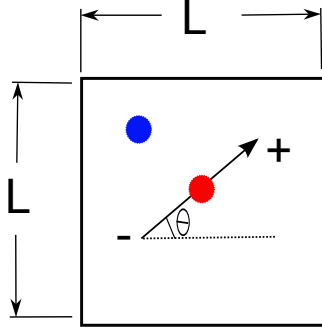
Figure 3.1: Schematic of microtubules in a 2D square domain of length L. Microtubules are shown in black, where the arrow represents the positive end. Also, microtubule orientation is measured from the horizontal of the negative end of the microtubule. Bound motors are red, and unbound motors are blue.

in only 1D). This advection term not only describes MT treadmilling, but also describes MT sliding (in the case where motors are stationary, as described in Chapter 4). Also, we introduce a probability distribution to describe how MTs reorient in the presence of motors. This distribution is based on biological interactions between MTs and motors, and will be incorporated into a non-local term that will describe large angular variations in MTs. Finally, other models have used either parallel or perpendicular type boundary conditions, forcing MTs to take on particular orientations at the boundary of the domain [30]. In our model, a novel bounce back boundary condition is used that allows MTs to reorient more naturally at the boundary. The goal of building such a model is to not only describe MT patterns, but to do so in a way that is biologically reasonable and mathematically tractable.

First, in Section 3.1, we describe the model set-up and assumptions and in Section 3.2 we describe the model variables, parameters, and functions. Then, in Section 3.3 we describe the model equations. Finally, in Section 3.4, we describe the numerical details of our modelling efforts.

3.1 Model set-up and assumptions

To start developing our model, we first provide a schematic of the set up (shown in Figure 3.1). Here, we consider a square domain (where $\Omega = (0, L) \times (0, L)$) to represent a simplification of the cross section through a cell. The cross section of most cells is circular, however, here we choose a rectangle domain

since it easiest to run simulations on such a domain. However, such a domain would work well to describe the cross section of a columnar epithelial cell (shown in Figure 1.5(c)) [13].

From Figure 3.1, we show that each MT has a positive end and a negative end, where its orientation θ is measured from the horizontal of the negative end to the positive end. We also consider time $t > 0$ and $-\pi < \theta < \pi$.

Also, we consider one type of motor protein. In particular, we consider modeling the interaction of MTs in the presence of either negative-directed motors (like dynein) or positive-directed motors (like kinesin). Here, we show a modelling framework for negative-directed motors, although, it could just as easily be done for positive-directed motors. From Figure 3.1, we see that each motor is in one of two states, bound or unbound. Since we are considering negative-directed motors, motors that are attached to MTs move towards the MTs negative end.

The following assumptions will be made regarding the dynamics of interacting as well as non-interacting MTs and motors:

(1) In the absence of MTs, motors are free to diffuse in the cytoplasm.

(2) Bound motors move with constant velocity along MTs. Bound motors become unbound by falling off MTs at a constant rate.

(3) Treadmilling accounts for directed motion of MTs along their axis. In particular, the positive end of a MT grows at the same rate as the negative end of a MT shrinks. Another means of directed transport includes sliding (in the presence of stationary motors).

(4) We assume that the diffusion process for MTs is much slower than the time it takes for MT rearrangement (hence we neglect MT diffusion).

(5) MTs can be aligned with one another in the presence of motors. The more motors that are present, the more likely alignment occurs.

(7) Alignment tends to the mean MT orientation μ (described below by equation (3.9)).

33

3.2 Model variables, parameters, and functions

Next, we give a list of the independent and dependent model variables (with units in brackets).

- t $[s]$: time.

- $\vec{x}$ $[\mu m \times \mu m]$: space.

- θ $[rad]$: angular orientation.

- $m_b(\vec{x}, t)$ $[mass/\mu^2]$: the density of bound motors at time t and position $\vec{x}$.

- $m_u(\vec{x}, t)$ $[mass/\mu^2]$: the density of unbound motors at time t and position $\vec{x}$.

- $p(\vec{x}, t, \theta)$ $[mass/\mu^2]$: the density of MTs at time t, and at position $\vec{x}$, and orientation θ.

As well, we give a list of other model parameters and functions (with units in brackets). The values of each parameter are summarized in Table 3.1.

- $\mathbf{v_b}$ $[\mu m/s]$: Represents the velocity of bound motors. In particular, bound motors move with a constant speed $||\mathbf{v_b}||$, along the mean MT orientation μ (described in equation (3.9)).

- $k_{on}(p)$ $[1/s]$: Represents the rate at which an unbound motor becomes a bound motor. This rate depends on the MT density p.

- k_{on}^{max} $[1/s]$: Represents the maximum rate at which an unbound motor becomes a bound motor.

- k_{off} $[1/s]$: Represents the constant rate at which a bound motor becomes an unbound motor.

- D_u $[\mu m^2/s]$: The diffusion constant for unbound motors.

- S_{MT} $[\mu m/s]$: Constant treadmilling speed.

- $k(\theta, \tilde{\theta}, m_b)$: A probability density function describing the probability that a MT at an angle $\tilde{\theta}$ will be recruited to have angle θ. This probability depends on m_b, as described later.

- $\lambda(m_b)$ $[1/s]$: The rate at which a MT switches orientation. This rate depends on bound motors m_b.

- λ_{max} $[1/s]$: The maximum rate at which a MT switches orientation.

- $\alpha(m_b)$: Alignment function. This rate depends on bound motors m_b.

- C: Motor activity parameter.

- μ $[rad]$: mean angular orientation.

- $\hat{\mu}$: mean angular orientation unit vector.

- $\hat{\theta}$: angular orientation unit vector.

parameter	value	meaning	source
$\| \mathbf{v_b} \|_{fast}$	$0.09 - 0.1\ \mu m s^{-1}$	Speed of NCD motor *in vitro*	[19]
$\| \mathbf{v_b} \|_{slow}$	$0.01 - 0.04\ \mu m s^{-1}$	Max speed kinesin-5 *in vitro*	[19]
k_{on}^{max} high	$10\ s^{-1}$	Max attachment rate for processive motors	[58]
k_{on}^{max} med	$5\ s^{-1}$	Max attachment rate for weakly processive motors	This Thesis
k_{on}^{max} low	$0.1\ s^{-1}$	Max attachment rate for non-processive motors	This Thesis
k_{off} low	$0.1\ s^{-1}$	Dissociation rate of processive motors	[58]
k_{off} med	$5\ s^{-1}$	Dissociation rate of weakly processive motors	This Thesis
k_{off} high	$10\ s^{-1}$	Dissociation rate of non-processive motors	This Thesis
D_u	$20\ \mu m^2 s^{-1}$	Diffusion constant for NCD motors *in vivo*	[38]
S_{MT} high	$0.12\ \mu m s^{-1}$	Treadmilling speed of interphase MTs released from	[54]
S_{MT} low	$0.04 \mu m s^{-1}$	Typical Treadmilling speed of MTs grown *in vitro*	[54]
		centrosome of fibroblastic cells *in vitro*	
λ_{max}	$40\ s^{-1}$	Switching rate of MTs	This Thesis
C low	0.1	Motor activity parameter	This Thesis
C high	25	Motor activity parameter	This Thesis

Table 3.1: Model parameter values and sources for the full model

3.3 Model equations

Equations (3.1), (3.2), and (3.3) describe the dynamic interaction between bound motors m_b (motors attached to MTs), unbound motors m_u (motors not attached to MTs), and MTs p, respectively

$$\frac{\partial m_b(\vec{x}, t)}{\partial t} + \nabla_{\vec{x}} \cdot (\mathbf{v_b} m_b(\vec{x}, t)) = k_{on}(\tilde{p})m_u(\vec{x}, t) - k_{off}m_b(\vec{x}, t) \qquad (3.1)$$

$$\frac{\partial m_u(\vec{x}, t)}{\partial t} - D_u \Delta_{\vec{x}} m_u(\vec{x}, t) = -k_{on}(\tilde{p})m_u(\vec{x}, t) + k_{off}m_b(\vec{x}, t) \qquad (3.2)$$

$$\frac{\partial p(\vec{x}, t, \theta)}{\partial t} + S_{MT}\hat{\theta} \cdot \nabla_{\vec{x}} p(\vec{x}, t, \theta) = -\lambda(m_b)p(\vec{x}, t, \theta)$$
$$+ \lambda(m_b) \int_{-\pi}^{\pi} k(\theta, \tilde{\theta}, m_b)p(\vec{x}, t, \theta)d\tilde{\theta}. \qquad (3.3)$$

Here, we consider either periodic boundary conditions,

$$m_b(0, y, t) = m_b(L, y, t)$$
$$m_u(0, y, t) = m_u(L, y, t) \qquad (3.4)$$
$$p(0, y, t, \theta) = p(L, y, t, \theta);\ p(x, 0, t, \theta) = p(x, L, t, \theta),$$

or no-flux (Neumann) boundary conditions for motors and a novel *bounce back* boundary condition for MTs. The numerical implementation of the bounce back condition for MTs is described in detail in Section 3.4 by equations 3.18 and 3.19. An explicit mathematical expression for this new boundary condition is still work in progress.

For simplicity in reading, we write $p(\vec{x}, t, \theta) = p(x, y, t, \theta)$ in the above boundary conditions. Here, $\tilde{p}(\vec{x}, t) = \int_{S^1} p(\vec{x}, t, \theta)d\theta$ is to total MT density at each point in space $\vec{x}$ and time t. Equations (3.1) and (3.2) describe motor movement. Like the model of Aranson and Tsimring (from equation (2.10)), we are explicitly describing the movement of motors within our domain.

Equation (3.1) states that bound motors move with constant speed $\| \mathbf{v_b} \|$ along the mean orientation of the MT network μ. Also, bound motors fall off of MTs at a rate k_{off} and unbound motors become bound motors by attaching to MTs at a rate $k_{on}(\tilde{p})$. Here, the rate k_{off} is constant, whereas the rate $k_{on}(\tilde{p})$ may depend on the MT density $\tilde{p}$ (the more MTs present the more likely it is

for a motor to attach). For simplicity, we assume that k_{on} is a Hill function of the second kind with respect to the total MT negative-end density $\tilde{p}$. That is,

$$k_{on}(\tilde{p}) = k_{on}^{max} \frac{\tilde{p}}{1 + \tilde{p}} \tag{3.5}$$

where k_{on}^{max} is the max rate of attachment and its value is found in Table 3.1.

It has been found that motor speed depends on whether the motor is carrying a light or heavy load (i.e., the smaller the load the faster the motor) [43]. Also, it has been found that motor speed may be dependent on the number of motors present (i.e., the more motors present the slower the speed) [SMB reference]. However, for now we will neglect load mass and motor density and write the velocity $\mathbf{v_b}$ in the following way,

$$\mathbf{v_b} = -||\mathbf{v_b}||\hat{\mu} = -||\mathbf{v_b}|| \begin{pmatrix} \hat{\mu}_x \\ \hat{\mu}_y \end{pmatrix}. \tag{3.6}$$

Here, the speed $||\mathbf{v_b}||$ is constant, where the negative sign accounts for the fact that motors move in a direction that is opposite to the mean MT orientation vector $\hat{\mu}$ (the 'hat' symbol represents the unit vector). If we were to consider positive-directed motors (like kinesins), we change this sign to positive. The x and y components of this vector, $\hat{\mu}_x$ and $\hat{\mu}_y$, are given in equations (3.7) and (3.8), respectively, and describe the integral mean of the x and y components of the orientation, where $x = \cos(\theta)$ and $y = \sin(\theta)$. The mean orientation μ can then be written as an angle using the equation (3.9).

$$\hat{\mu}_x = \frac{\int_{-\pi}^{\pi} \cos(\theta) p(\vec{x}, t, \theta) d\theta}{\int_{-\pi}^{\pi} p(\vec{x}, t, \theta) d\theta} \tag{3.7}$$

$$\hat{\mu}_y = \frac{\int_{-\pi}^{\pi} \sin(\theta) p(\vec{x}, t, \theta) d\theta}{\int_{-\pi}^{\pi} p(\vec{x}, t, \theta) d\theta} \tag{3.8}$$

$$\mu = \arctan(\mu_x/\mu_y) + j\pi \tag{3.9}$$

Here $j = 0$ if $\hat{\mu}_x > 0$, $j = -1$ if $\hat{\mu}_x < 0$ and $\hat{\mu}_y < 0$, and $j = 1$ if $\hat{\mu}_x < 0$ and $\hat{\mu}_y > 0$.

The second equation for motor movement, equation (3.2) states that un-

bound motors diffuse freely in the absence of MTs with diffusion constant D_u. In the presence of MTs, we have similar switching terms as the bound motors in equation (3.1). That is, unbound motors attach to MTs at rate $k_{on}(\tilde{p})$ and bound motors become unbound motors at rate k_{off}. Switching terms such as these are used in many types of models where an object (e.g., proteins) can be in one of two states. For example, recall the switching terms in equations (2.5) and (2.6), used to describe static and moving pigment granules in fish melanophores.

Finally, the equation for MT movement given by equation (3.3), describes the time evolution of MTs due to the fact that MTs can treadmill and realign. The expression on the left side of equation (3.3) accounts for directed MT motion along the axis of the MT $\hat{\theta}$, where $\hat{\theta} = \begin{pmatrix} \cos(\theta) \\ \sin(\theta) \end{pmatrix}$, due to MT treadmilling. It is an advection-type term, similar to the term used in equations (2.3) and (2.4) to describe treadmilling of MTs in fish melanophores. In our model, such a term is also used to describe MT treadmilling. In particular, it describes MT movement along its axis with constant speed S_{MT}.

The last terms on the right-hand side of equation (3.3) represent non-local interactions between MTs. In particular, it is the stochastic part of the model and describes a velocity jump process [45, 46] for MT reorientation. Such processes are commonly used to describe systems that exhibit a sequence of 'runs' (directed motion) separated by reorientations. As stated above, we want to incorporate a non-local term, similar to that of equation (2.9), since in many cell types MT motion is directed for variable lengths of time (due to treadmilling). However, at any instance the MT can change its orientation when in the presence of motor proteins, and does so at the rate $\lambda(m_b)$. Here we choose $\lambda(m_b)$ to be a Hill function of the second kind with respect to the bound motor density m_b. That is,

$$\lambda(m_b) = \lambda_{max} \frac{m_b}{1 + m_b} \tag{3.10}$$

where λ_{max} is given in Table 3.1. We choose this type of function since it is a saturating function, and we expect the switching rate to saturate at some maximum value.

Each random orientation switch is the result of a Poisson process of inten-

sity λ (where λ is described above by equation (3.10)) [25]. A Poisson process is characterized by its parameter λ, which is the expected number of events that occur per unit time (in our case each event is a switch in MT orientation). Such a process has the property that each event does not depend on the previous state of the system. In particular, the process is independent in increments, meaning that the number of events that happen within a small interval of time are independent from one another. A Poisson process follows a Poisson distribution given by equation (3.11).

$$P(k) = \frac{\exp(-\lambda\tau)(-\lambda\tau)^k}{k!} \tag{3.11}$$

Here, k is the number of events (number of MT switches) that occur within a small time interval $[t, t + \tau]$. As stated above, λ describes the rate of MT switching. Here, we will define λ to be a linear function of the bound motor density m_b, so that when the bound motor density in zero, there is no switching, and when the bound motor density is high, λ is high.

The term $k(\theta, \theta), \tilde{\,} m_b$ is a probability density function for a reorientation of a MT from the angle $\tilde{\theta}$ to θ (and depends on m_b). If $\Theta(t)$ is a random variable giving the MTs orientation at time t, then given that a reorientation occurs at T,

$$k(\theta, \tilde{\theta}, m_b)d\theta = Pr\{\theta \leq \Theta(T^+) \leq \theta + d\theta \mid \Theta(T^-) = \tilde{\theta}\}.$$

We assume that the probability of recruitment of a MT at a point $\vec{x}$ to an angle θ depends only on how close that angle is to the mean MT orientation μ (described in equation (3.9)). In particular, the probability of recruitment does not depend on the angle from which the MT came, $\tilde{\theta}$. This assumption can be better understood from Figure 3.2 and suggests that, at every time step, the MT network tends to align towards its mean μ.

Since we would like the MT network to align towards the mean μ, we would like k to have the property that if the difference $\theta - \mu$ is large, then the probability of recruitment is small, whereas if this difference is small, the probability of recruitment is large. Also, since k is a probability distribution over θ, it must have the property that

$$\int_{-\pi}^{\pi} k(\theta)d\theta = 1. \tag{3.12}$$

(a)   (b)   (c)
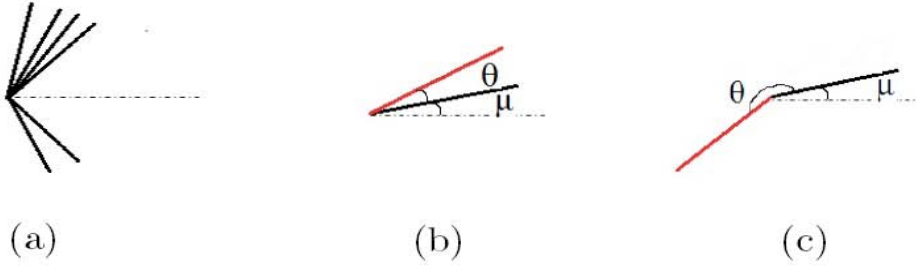
Figure 3.2: (a) MTs centered at a point. (b) The mean orientation of MTs μ in (a) is shown in black and a possible angle of reorientation θ is shown in red. (c) The mean orientation of MTs μ in (a) is shown in black and a second possible angle of reorientation θ is shown in red. From (b) and (c) we see that it is more likely for MTs to be reoriented to the angle θ in (b).
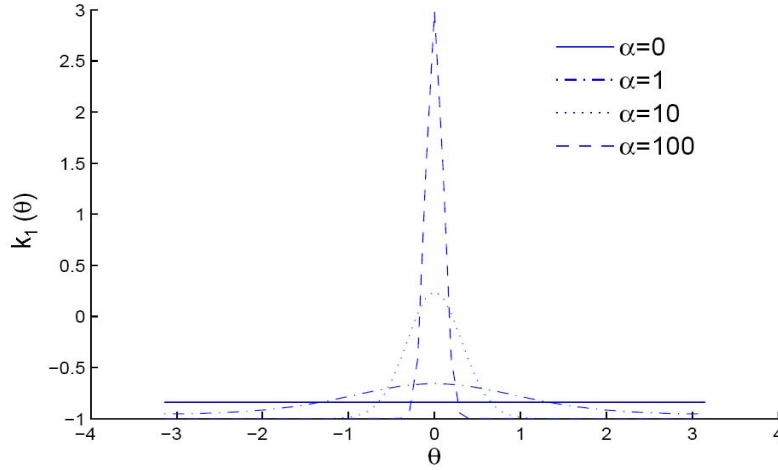
Figure 3.3: MT redistribution kernel k_1 centered at mean $\mu=0$ for different values of α.

One choice for k, which we denote as k_1, is the Von Mises distribution [25, 46],

$$k_1(\theta, \tilde{\theta}, m_b) \frac{1}{2\pi I_0(\alpha(m_b))} \exp(\alpha(m_b)\cos(\theta - \mu)). \tag{3.13}$$

where $I_0(\alpha(m_b))$ is the modified Bessel function of order 0 and parameter $\alpha(m_b)$, and μ and $1/\alpha$ are the mean and variance of the distribution, respectively. Figure 3.3 shows a description of $k_1(\theta)$ centered at mean $\mu = 0$ for various values of the variance $1/\alpha$.

Since we have assumed that MTs tend to align to the mean MT orientation μ in the presence of bound motors m_b (and that there is no alignment

41
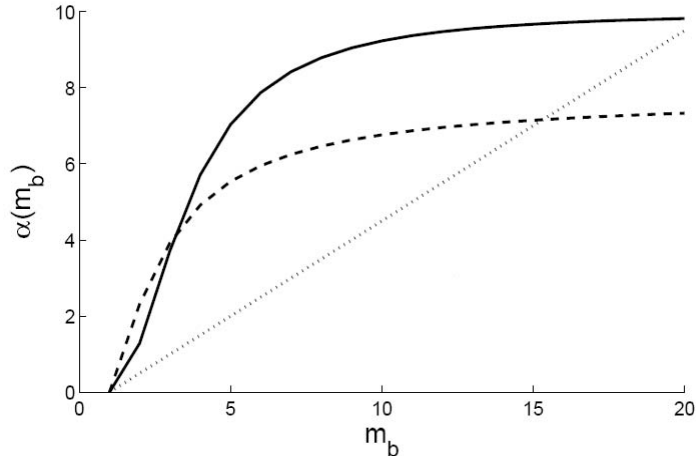
Figure 3.4: The solid line represents a sigmoidal response function of order 2 (with saturating max at $\alpha = 10$), the dashed line represents the arc tangent function (with max reached at $\alpha = 6.5$), and the dotted line is an example of a linear function.

when there are no motors present), we choose $\alpha(m_b)$ to be some monotonically increasing function of m_b, so that when many bound motors are present, the distribution is concentrated about the mean μ, and alignment is more likely. Also, if m_b is very small, the distribution is close to uniform, and alignment is less likely. We call $\alpha(m_b)$ the alignment function, where Figure 3.4 describes several possible choices for this monotonically increasing function $\alpha(m_b)$. For simplicity we choose the alignment function $\alpha(m_b)$ to be a linear function with respect to m_b so that,

$$\alpha(m_b) = Cm_b, \tag{3.14}$$

where we call C the motor activity parameter. Here, we see that for fixed C, by increasing m_b alignment is more likely, and by decreasing m_b alignment is less likely. However, we can also consider fixing m_b, and changing C, where the higher the motor activity C, the more likely alignment is (and vice versa).

A second choice for k, which we denote as k_2, is similar to that of equation (3.9). In particular, we choose k_2 to also be a circular normal distribution such that

$$k_2(\theta, \tilde{\theta}, m_b) = \frac{1}{2\pi I_0(\alpha(m_b))} \exp(\alpha(m_b) \cos(\tilde{\theta} - \theta)). \tag{3.15}$$

In this case, MTs that have a small angular displacement from one another are more likely to align than MTs that have a larger angular displacement from one another (in the presence of motors).

As stated above, the model given by equation (3.3) is in a class of models that are derived from a velocity jump process. Such a process is described in earlier works by Othmer [46]. In particular, such processes describe how a population evolves in time due to changes in an individuals velocity. The general form for such a process, as stated by Othmer [46], is given by

$$\frac{\partial p}{\partial t} + \nabla_{\mathbf{x}} \cdot \mathbf{v}p + \nabla_{\mathbf{v}} \cdot \mathbf{F}p = R, \tag{3.16}$$

where $\mathbf{F}$ denotes the external force acting on the individuals and R is the rate of change of the population p due to reaction, random choices in velocity, etc. The velocity jump process is analogous to the Bolztmann equation in the kinetic theory of gases, which describes how a gas or fluid transports physical quantities such as heat or momentum.

Assuming that there are no external forces acting on the individuals ($\mathbf{F} = 0$), and that the only process that contributes to changes in the right-hand side of equation (3.16) is due to random changes in velocity (i.e., a stochastic process), equation (3.16) can be rewritten as

$$\frac{\partial p}{\partial t} + \nabla_{\mathbf{x}} \cdot \mathbf{v}p = -\lambda p + \lambda \int k(v, \tilde{v}) p(\mathbf{x}, \tilde{v}, t) d\tilde{v}, \tag{3.17}$$

which is of the same form as our model in equation (3.3). Here, it is assumed that the random velocity changes are due to a Poisson process [25] of intensity λ. Also, $k(v, \tilde{v})$ gives the probability for a change in velocity from $\tilde{v}$ to v and so satisfies the normalization condition

$$\int k(v, \tilde{v}) dv = 1.$$

Besides our model in equation (3.3) and the model of Aranson and Tsimring in equation (2.9), there are also many other non-local models that have been used extensively in the literature to describe pattern formation in other biological systems. Examples of such models include animal movement models, developed to describe the movement of animals in relation to their interactions with other animals over large length scales and/or large angular scales [14, 46].

Patterns formed by changes in angular distributions include flocks of flying birds and schools of fish. Also, patterns arising from angular and spatial interactions of rod-like molecules (liquid crystals) have been extensively studied in physics [12].

3.4 Details of numerical scheme

We discretize the space-time plane choosing an equal space step in the x and y-direction $\Delta x = \Delta y = h$, and a time step $\Delta t = k$. We discretize angular space by choosing an angle step $\Delta \theta = w$. Also, we define the discrete mesh points $(x_j, y_l, t_n, \theta_\tau) = (jh, lh, nk, \tau w)$, $j, l, n, \tau \in \mathbb{N}$.

To simulate the advection part of the model (the left-hand side of equation (3.3)), we use a first order upwind scheme at each location. The direction of the unwind velocity at each point depends on the MT direction θ. For example, if $\theta = 3\pi/4$, the direction vector $\hat{\theta} = \begin{pmatrix} \cos(\theta) \\ \sin(\theta) \end{pmatrix} = \begin{pmatrix} -0.7071 \\ 0.7071 \end{pmatrix}$, and so we perform upwinding in the negative x direction and upwinding in the positive y direction.

To simulate the integral term on the right-hand side of equation (3.3), we use the trapazoid method. In particular, we use the trapz command in Matlab. Such a method is fine to use because of the nice properties of our kernel k.

There is a single type of instability associated with this numerical scheme. In particular, for the advection part of the model, when the Courant-Friedrichs Lewy (CFL) condition is not satisfied, the scheme becomes unstable. Since we have advection in both the x and y directions, this condition must be satisfied for both directions. In particular, we must have $S_{MT}|\cos(\theta)|k/h < 1$ for the x direction, and $S_{MT}|\sin(\theta)|k/h < 1$ for the y direction. Throughout each simulation we use a space step size $h = 0.01\bar{6}$ and a time step $k = 0.25$.

Also, we use an angle step size of $w = 2\pi/64$. Choosing smaller step sizes than this does not change the outcome of solutions. It is computationally faster to choose a larger angle step size, and so this is the step size we choose.

As stated in the previous section, we study equations (3.1) through (3.3) first using periodic boundary conditions, given by equation (3.4). Periodic boundary conditions in two-dimensions are not biologically realistic, since the
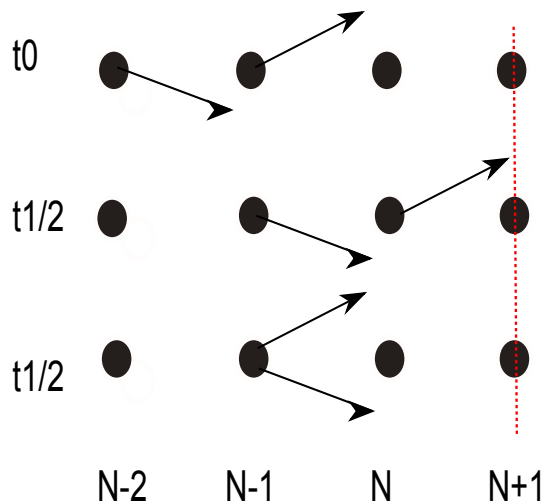
Figure 3.5: An example of how no-flux boundary conditions work in 1-D for an upwind scheme. Red line represents the boundary. (a) We start with zero MTs at the last two mesh points (N and N+1). For simplicity we choose only one MT per mesh point, however in simulations we can have many MTs at each mesh point. At each time step, the following two operations are performed: (b) MTs move forward according to the upwind scheme and fill all mesh points except N+1 (since that is the boundary), (b) MTs at the N mesh point are moved back one mesh point (to N-1), leaving zero MTs at the last two mesh points once again.

domain we are affectively simulating the movement of MTs on is a torus. However, these boundary conditions are generally used for simulating models similar to equation (3.3) because they are relatively easy to simulate. We also simulate our model using a no-flux boundary condition for motors and a novel *bounce back* condition for MTs. Such a condition in two-dimensions in more biologically realistic, since MT movement at the domain boundary is treated similar to how MTs might behave at a cell boundary. No-flux type boundary conditions can be difficult to simulate for integral equations such as ours, and so often either parallel or normal boundary conditions are used instead [30]. For these conditions, when a MT (a fixed length rod at a particular orientation) reaches the boundary, it is instantaneously oriented parallel or perpendicular with respect to the boundary. This boundary condition, though easier to simulate, does not allow for a natural (smooth) movement of MTs along boundaries. Here, we use a new approach to calculate the orientation of MTs once the reach the boundary, which allows for a more natural movement of the MT. Such a method can be described by Figure 3.5.

Let us just consider the 1-dimensional case where we look at only the last

few mesh points near the right boundary. Initially, as shown in Figure 3.5(a), we start with zero MTs on the boundary and one mesh point behind the boundary. During the first half of each time step, we move all MTs according to the appropriate upwind scheme. For simplicity, we just consider the upwind scheme and so all MTs move forward as in Figure 3.5(b). In Figure 3.5(c), we show how MTs in second last mesh point, N, are moved back into the N-1 mesh point during the second half of each time step. Now there are zero MTs again at the last two mesh points. If we let $p_{j,t,\theta}$ represent the density of MTs at location j, at time t, and orientation θ, we can describe movement of MTs at the boundary during the second half of each time step by,

$$p_{N-1,t+1,\theta} = p_{N-1,t+1/2,\theta} + p_{N,t+1/2,\theta}, \qquad (3.18)$$

$$p_{N,t+1,\theta} = 0. \qquad (3.19)$$

If motors are located at the mesh points defined above, the next step would be to perform reorientation of the MTs according to the integral part of the equation (3.3). However, if motors are not located at these points, the process described in Figure 3.5 would be repeated, and the two MTs that are at the N-1 mesh point will move to the N mesh point, but will be moved back into the N-1 mesh point with the MTs that have moved forward from the N-2 mesh point. In affect, we have a build up of MTs on the boundary, since MTs keep being bounced back and forth between the last two mesh points with new MTs coming in from the N-2 mesh point.

Chapter 4

The Transport Model: Part 1

In this chapter, we describe MT patterns formed when motors are stationary. In this case, the equations (3.1) to (3.3) are reduced to the following,

$$m_b = \frac{k_{on}}{k_{off}} m_u, \tag{4.1}$$

$$\frac{\partial p(\vec{x}, t, \theta)}{\partial t} + S_{MT}\hat{\theta} \cdot \nabla_{\vec{x}} p(\vec{x}, t, \theta) = -\lambda(m_b) p(\vec{x}, t, \theta)$$
$$+ \lambda(m_b) \int_{-\pi}^{\pi} k(\theta, \tilde{\theta}, m_b) p(\vec{x}, t, \tilde{\theta}) d\tilde{\theta}. \tag{4.2}$$

Here, motors are fixed in space $\vec{x}$ and time t, and so we look at the different types of MT patterns that are formed by fixing motors in different configurations and allowing only MTs to move. This situation can be experimentally reproduced by absorbing (sticking) motors to a two-dimensional surface (like a slide) at their cargo domain [69, 15], where its free legs are able to attach to a MT. Since the motor remains stationary, when a negative (positive)-directed motor moves along a MT, the motor pushes the MT along the MTs own axis towards its positive (negative) end. Here, S_{MT} is not only a treadmilling rate, but it also incorporates MT sliding. A mathematical description of sliding is similar to MT treadmilling in that both types of motion describe directed movement of MTs along their axis. The only difference is that MT treadmilling can occur when motors are not present (MT sliding requires motors).

In this chapter, we will focus on three simplifications of the above model.

In particular, in Section 4.1, we describe analytical and numerical results for a Fredholm model that is derived under the assumption that MTs do not glide ($S_{MT} = 0$), and that the MT distribution is at steady state ($\partial/\partial t = 0$). In Section 4.2, we describe numerical results for an equation which we call the turning equation. This equation is derived under the assumption that MTs do not glide ($S_{MT} = 0$). Finally, in Section 4.3 we consider a limiting case to the full non-local integro-differential equation model for MT movement so that we can rewrite it as a local diffusion model. Later, in Chapter 5, we will consider results of the full model given by equations (4.1) and (4.2).

4.1   The Fredholm Model

Here we describe the results for the Fredholm Model. That is, we describe results for the model given by equation (4.1) and (4.2) in the case when $S_{MT} = 0$ and the system is at steady state. The model is given by

$$m_b = \frac{k_{on}}{k_{off}} m_u, \tag{4.3}$$

$$p(\theta) = \int_{-\pi}^{\pi} k(\theta, \tilde{\theta}, m_b) p(\tilde{\theta}) d\tilde{\theta}. \tag{4.4}$$

Here the bound and unbound motor populations, m_b and m_u, are constant with respect to space $\vec{x}$ and time t, and the MT density p only depends on orientation θ. Such an equation is classified as a Fredholm Equation of the Second Kind [50]. In particular, this equation is of the form

$$p(\theta) - \gamma \int_a^b k(\theta, \tilde{\theta}) p(\tilde{\theta}) d\tilde{\theta} = f(\theta), \tag{4.5}$$

with $f(\theta) = 0$ and $\gamma = 1$. Also, a and b (which must be finite), are given by $a = -\pi$ and $b = \pi$. Recall from Chapter 3 that one choice for the reorientation kernel k is given by

$$k(\theta, m_b) = \frac{1}{2\pi I_0(\alpha(m_b))} \exp(\alpha(m_b) \cos(\theta - \mu)),$$

where μ is the mean MT orientation and $\alpha(m_b) = Cm_b$, where C is the motor activity parameter. For this particular choice of k, we can pull k outside the integral sign since it is not a function of $\tilde{\theta}$ and so equation (4.4) can be written as

$$p(\theta) = k(\theta, m_b) \int_{-\pi}^{\pi} p(\tilde{\theta}) d\tilde{\theta}, \qquad (4.6)$$

where $\int_{-\pi}^{\pi} p(\tilde{\theta}) d\tilde{\theta}$ is constant and without loss of generality we can let this constant equal to 1. Thus, solutions to equation (4.6) are given by

$$p(\theta) = k(\theta, m_b). \qquad (4.7)$$

In the limits of α going to zero and infinity we get,

$$\lim_{\alpha \to 0} p(\theta) = \frac{1}{2\pi} \qquad (4.8)$$

$$\lim_{\alpha \to \infty} p(\theta) = \delta(\mu), \qquad (4.9)$$

Where $\delta(\mu)$ is the dirac delta functional and can loosely be defined by

$$\delta(\theta) = \left\{ \begin{array}{ll} \infty & \text{if } \theta = \mu \\ 0 & \text{if } \theta \neq \mu. \end{array} \right\}$$

Since $\alpha(m_b) = Cm_b$ and m_b is constant, the limits above show that if the motor activity C is low $(0 < C \ll 1)$, we have a uniform distribution of MTs, and if C is high $(C \gg 1)$, we have alignment of MTs towards some mean angle μ. Figure 4.1 shows solution curves for the equation (4.7) for various values of α.

From Figure 4.1 we see that higher values of α correspond to sharper peaked solutions, whereas if α is low we have flatter solutions.

4.2 The Turning Equation

Here we describe the results for the Turning Equation. That is, we describe results for the model given by equation (4.1) and (4.2) in the case when $S_{MT} = 0$. The model is given by
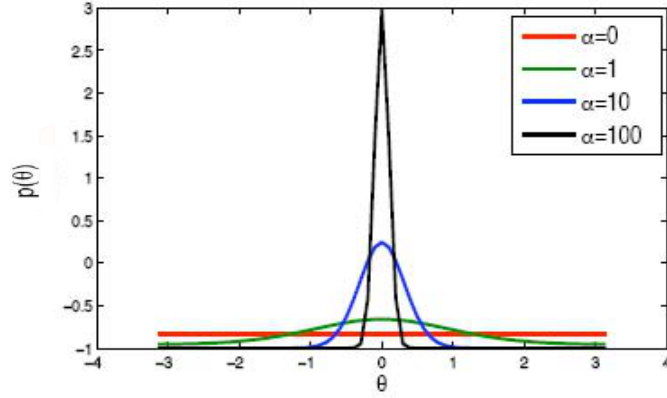
Figure 4.1: $p(\theta) = k(\theta, m_b)$ with mean $\mu=0$ and $\alpha = 0, 1, 10,$ and 100

$$m_b = \frac{k_{on}}{k_{off}} m_u, \tag{4.10}$$

$$\frac{\partial p(\theta, t)}{\partial t} = -\lambda p(\theta, t) + \lambda \int_{-\pi}^{\pi} k(\theta, \tilde{\theta}, m_b) p(\tilde{\theta}, t) d\tilde{\theta}. \tag{4.11}$$

Figure 4.2 describes numerical simulations for the equation (4.11). Figure 4.2(top row) describes the MT distribution $p(\theta, t)$ at four different time steps when the motor activity parameter C is low ($C = 0.1$). In particular, Figure 4.2(top row)(a) shows the initial distribution $p(\theta, 0)$, which is chosen at random. Figure 4.2(top row)(d) shows distribution at large time t, in particular it shows $p(\theta, 50)$. These results show that the distribution eventually becomes uniform and is consistent with the results of Section 4.1. In particular, from 4.8, we have that the steady-state of the equation (4.11) for very low alpha is a uniform distribution.

Figure 4.2(bottom row) describes the MT distribution $p(\theta, t)$ for different time steps when the motor activity parameter C is high ($C = 25$). Figure 4.2(bottom row)(a) shows the initial distribution $p(\theta, 0)$, which is again chosen at random, and Figure 4.2(bottom row)(d) shows the distribution after long time t, $p(\theta, 50)$. The results show that the distribution is eventually centered about mean μ (here, $\mu \cong -1.9$ radians). The angle μ is determined by the

50
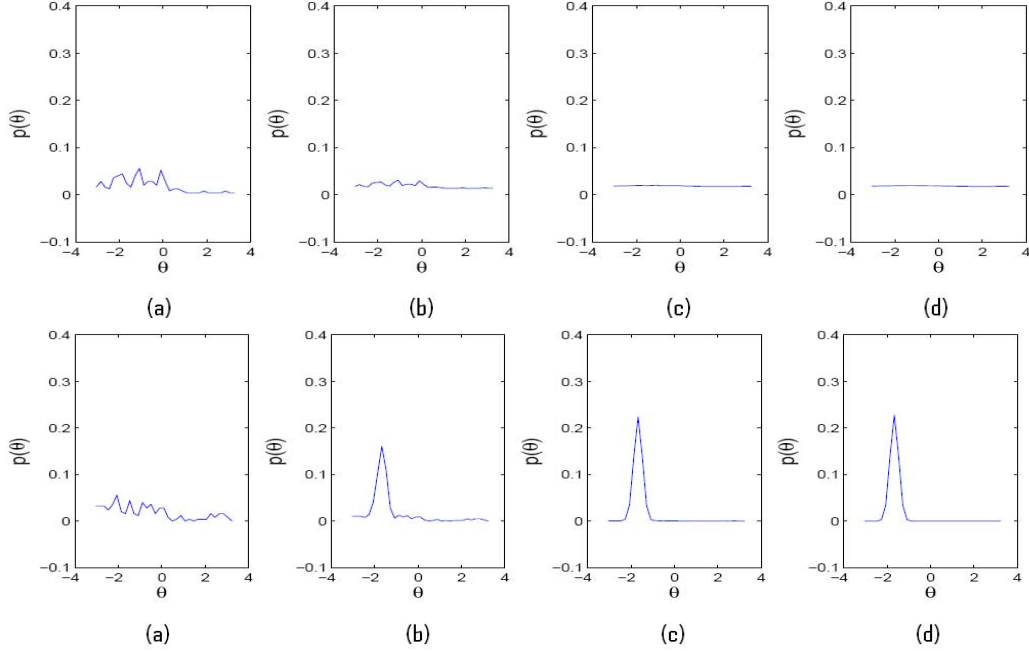
Figure 4.2: Top row: Evolution of the MT distribution $p(\theta, t)$ for C low ($C = 0.1$). (a) Initial distribution of MTs $p(\theta, 0)$ is random, (b) $p(\theta, 5)$; (c) $p(\theta, 15)$; (d) $p(\theta, 50)$. Bottom row: Evolution of the MT distribution $p(\theta, t)$ for C high ($C = 25$). (a) Initial distribution of MTs $p(\theta, 0)$ is random, (b) $p(\theta, 5)$; (c) $p(\theta, 15)$; (d) $p(\theta, 50)$.

initial conditions; it is the angle at which the majority of MTs are located at time $t = 0$ (see Figure 4.2(bottom row)(a)). Again, this result is consistent with the results of Section 4.1. In particular, from 4.9, we have that the steady-state of the equation (4.11) for very high alpha is the Dirac Delta Functional, centered around the mean MT orientation μ.

4.3 The Diffusion Limit

When working with transport equations such as equation (4.2), it is often useful to consider different scalings. In particular, under certain assumptions, such an equation can be scaled in a way that makes it easier to analyze. The three most popular types of scalings include the parabolic scaling, the hyperbolic scaling, and the moment closure method. A nice description of each method can be found in a recent paper by Hillen and Painter [34].

The parabolic scaling, which we outline in detail below, refers to the case where we consider slow velocities (in our case this refers to slow treadmilling

speed S_{MT}), and very fast switching rates (in our case this refers to fast MT switching rate λ_{max}). This scaling leads to an isotropic diffusion equation, where orientation is an implicit part of the model, being radial at each point in space (i.e., the mean orientation is necessarily zero in this case, as will be discussed in detail below). The other scalings (hyperbolic and moment closure) will not be considered here.

We outline the steps taken to re-scale the equation for MT movement given by (3.3) using the parabolic scaling method, so that we can reformulate the integro-differential model as a diffusion model. Again, this method is outlined in [34].

First, we scale the variables in the equation for MT minus-end density p in the following way:

$$\tilde{\theta} = \frac{\theta}{\theta^*},$$
$$\tilde{x} = \frac{x}{l^*},$$
$$\tilde{t} = \frac{t}{\sigma^*}.$$

Here, θ^* is the characteristic speed ($\approx 0.01 \mu m/s$), l^* is the characteristic length ($\approx 1 \mu m$), and σ^* is the macroscopic time of observation ($\approx 1 \to 10$ hrs **or** $\approx 10^3 \to 10^4 s$). By substituting these scalings into equation (3.3) we obtain

$$\frac{1}{\sigma^*}\frac{\partial p(\vec{x}, t, \theta)}{\partial \tilde{t}} + \frac{\tilde{\theta}^*}{l^*}\theta^* \cdot \nabla_{\vec{\tilde{x}}} p(\vec{x}, t, \theta) = Lp(\vec{x}, t, \theta), \tag{4.12}$$

where L is the turning operator defined by
We define the turning operator L as

$$L(p(\theta)) = \lambda p(\theta) + \lambda K(p(\theta)), \tag{4.13}$$

and its adjoint as

$$L^*(p(\theta)) = \lambda p(\theta) + \lambda K^*(p(\theta)), \tag{4.14}$$

52

where the linear operator $K : L^2([-\pi, \pi]) \longrightarrow L^2([-\pi, \pi])$ is defined as

$$K(p(\theta)) = \int_{S^1} k(\theta, \widetilde{\theta}, m_b) p(\widetilde{\theta}) d\widetilde{\theta}. \tag{4.15}$$

The kernel of L is given by the linear space $\langle k(\theta) \rangle$ (i.e., $L\phi(\theta) = 0$ for $\phi(\theta) \in \langle k(\theta) \rangle$). Also, we define

$$\frac{\theta^*}{l^*} = \varepsilon, \text{ and so } \frac{1}{\sigma^*} = \varepsilon^2.$$

Substituting for ε in equation (4.12) and removing the ˜ signs we obtain a singular perturbation problem

$$\varepsilon^2 p_t(\vec{x}, t, \theta) + \varepsilon \theta \cdot \nabla_x p(\vec{x}, t, \theta) = L p(\vec{x}, t, \theta). \tag{4.16}$$

For ε small, we study a perturbation expansion of the solution p so that

$$p(\vec{x}, t, \theta) = p_0(\vec{x}, t, \theta) + \varepsilon p_1(\vec{x}, t, \theta) + \varepsilon^2 p_2(\vec{x}, t, \theta) + \dots \tag{4.17}$$

The leading term of the expansion is $p_0(\vec{x}, t, \theta)$, and the higher-order terms are small deviations (perturbations) from the exact solution (since ε is a very small parameter). Here we study the perturbation expansion up to second order. In particular,

$$p(\vec{x}, t, \theta) = p_0(\vec{x}, t, \theta) + \varepsilon p_1(\vec{x}, t, \theta) + \varepsilon^2 p_2(\vec{x}, t, \theta). \tag{4.18}$$

By substituting (4.18) into (4.16) and comparing order ε^0, ε^1, and ε^2 terms, we will approximate (4.16), which is an equation for $p(\vec{x}, t, \theta)$ in terms of $\vec{x}$, t and θ, by an equation for $p(\vec{x}, t)$ in terms of $\vec{x}$ and t (thus reducing the number of independent variables).

$$\varepsilon^0 : \qquad 0 = L p_0(\vec{x}, t, \theta), \tag{4.19}$$

$$\varepsilon^1 : \qquad \hat{\theta} \cdot \nabla p_0(\vec{x}, t, \theta) = L p_1(\vec{x}, t, \theta), \tag{4.20}$$

$$\varepsilon^2 : \qquad \frac{\partial p_0(\vec{x}, t, \theta)}{\partial t} + \hat{\theta} \cdot \nabla p_1(\vec{x}, t, \theta) = L p_2(\vec{x}, t, \theta). \tag{4.21}$$

53

The order ε^0 equation (4.19) reads

$$0 = \lambda p_0(\vec{x}, t, \theta) - \lambda k(\theta) \int_{S^1} p_0(\vec{x}, t, \tilde{\theta}) d\tilde{\theta}.$$

Here, we arrive at $p_0(\vec{x}, t, \theta) = k(\theta) \int_{S^1} p_0(\vec{x}, t, \theta) d\theta$. We define $\bar{p}_0(\vec{x}, t) = \int_{S^1} p_0(\vec{x}, t, \theta) d\theta$, and so

$$p_0(\vec{x}, t, \theta) = k(\theta) \bar{p}_0(\vec{x}, t). \tag{4.22}$$

Next we look at the order ε^1 equation (4.20). This equation can be solved on $\langle k \rangle^{\perp}$ if the right-hand side of (4.20) satisfies the solvability condition $\hat{\theta} \cdot \nabla p_0(\vec{x}, t, \theta) \in \langle k \rangle^{\perp}$. That is, if

$$\int_{S^1} (\hat{\theta} \cdot \nabla) p_0(\vec{x}, t, \theta) d\theta = 0.$$

From equation (4.22), we find that the above simplifies to

$$\int_{S^1} (\hat{\theta} \cdot \nabla) k(\theta) \bar{p}_0(\vec{x}, t) d\theta = \bar{p}_0(\vec{x}, t) \nabla \cdot \int_{S^1} \hat{\theta} k(\theta) d\theta.$$

This term will only equal zero for arbitrary $\bar{p}_0$ if

$$\int_{S^1} \hat{\theta} k(\theta) d\theta = 0. \tag{4.23}$$

In other words, equation (4.23) states that the mean orientation is zero (and so the probability of moving in any direction at each spatial location is equal). Now, since $\hat{\theta} \cdot \nabla p_0(\mathbf{x}, t, \theta) \in \langle k \rangle^{\perp}$, we say that $L \mid_{\langle k \rangle^{\perp}}$ has a linear inverse F such that

$$p_1(\vec{x}, t, \theta) = F(\hat{\theta} \cdot \nabla p_0(\vec{x}, t, \theta)).$$

Finally, we look at the ε^2 equation (4.21). Integrating the order ε^2 equation over θ we arrive at the equation

$$\int_{S^1} \frac{\partial p_0(\vec{x}, t, \theta)}{\partial t} d\theta + \int_{S^1} \hat{\theta} \cdot \nabla p_1(\vec{x}, t, \theta) d\theta = \int_{S^1} L p_2(\vec{x}, t, \theta) d\theta.$$

Since the right-hand side of this equation gives us

$$\int_{S^1} L p_2(\vec{x}, t, \theta) d\theta = -\lambda \int p_2(\vec{x}, t, \theta) d\theta + \lambda \int_{S^1} k(\theta) d\theta \int_{S^1} p_2(\vec{x}, t, \theta) d\tilde{\theta} = 0,$$

54

we have that

$$\int_{S^1} \frac{\partial p_0(\vec{x}, t, \theta)}{\partial t} d\theta + \int_{S^1} \hat{\theta} \cdot \nabla p_1(\vec{x}, t, \theta) d\theta = 0.$$

Substituting equation (4.22) and $p_1(\vec{x}, t, \theta) = F(\hat{\theta} \cdot \nabla p_0(\vec{x}, t, \theta))$ we can write this equation as

$$\frac{\partial}{\partial t} \int_{S^1} p_0(\vec{x}, t, \theta) d\theta + \int_{S^1} \hat{\theta} \cdot \nabla(F(\hat{\theta} \cdot \nabla p_0(\vec{x}, t, \theta))) d\theta = 0,$$

which simplifies to

$$\frac{\partial \bar{p}_0(\vec{x}, t)}{\partial t} + \int_{S^1} \hat{\theta} \cdot \nabla(F(\hat{\theta} \cdot \nabla p_0(\vec{x}, t, \theta))) d\theta = 0. \tag{4.24}$$

Before we move further, we will determine the inverse function F of the turning operator L. To do this we must solve the following problem:

Given some function $\phi \in \langle k \rangle^\perp$, find $p \in \langle k \rangle^\perp$ such that $Lp = \phi \Rightarrow p = F\phi$.

We start by considering $Lp(\theta) = \phi(\theta)$.

$$Lp(\theta) = -\lambda p(\theta) + \lambda \int_{S^1} k(\theta) p(\tilde{\theta}) d\tilde{\theta}$$

$$= -\lambda p(\theta) + 0.$$

Here $\int_{S^1} k(\theta) p(\tilde{\theta}) d\tilde{\theta} = 0$ since $p \in \langle k \rangle^\perp$. Now, since we assumed $-\lambda p(\theta) = \phi(\theta)$, rearranging we get $p(\theta) = \frac{-1}{\lambda} \phi(\theta)$, and so $F = \frac{-1}{\lambda}$.

Substituting F and equation (4.22) into equation (4.24), we arrive at

$$\frac{\partial \bar{p}_0(\vec{x}, t)}{\partial t} - \frac{1}{\lambda} \int_{S^1} (\hat{\theta} \cdot \nabla) \hat{\theta} \cdot \nabla(k(\theta) \bar{p}_0(\vec{x}, t)) d\theta$$

$$= \frac{\partial \bar{p}_0(\vec{x}, t)}{\partial t} - \frac{1}{\lambda} \nabla \cdot \int_{S^1} \hat{\theta} \hat{\theta}^T \nabla(k(\theta) \bar{p}_0(\vec{x}, t)) d\theta$$

$$= \frac{\partial \bar{p}_0(\vec{x}, t)}{\partial t} - \nabla \nabla (D(\vec{x}) \bar{p}_0(\vec{x}, t))$$

$$= 0.$$

Thus we arrive at a diffusion-type equation for the MT density $\bar{p}_0$ that can be written as,

$$\frac{\partial \bar{p}_0(\vec{x}, t)}{\partial t} = \nabla\nabla(D(\vec{x})\bar{p}_0(\vec{x}, t)), \tag{4.25}$$

with diffusion tensor

$$D(\vec{x}) = -\frac{1}{\lambda} \int_{S^1} \hat{\theta}\hat{\theta}^T k(\vec{x}, \theta) d\theta. \tag{4.26}$$

Chapter 5

The Transport Model: Part 2

In this section, we consider the case where MTs are free to glide ($S_{MT} \neq 0$). Here we simplify the full model given by equations (3.1), (3.2), and (3.3) to the following system of equations:

$$m_b = \frac{k_{on}}{k_{off}} m_u \tag{5.1}$$

$$\frac{\partial p(\vec{x}, t, \theta)}{\partial t} + S_{MT}\hat{\theta} \cdot \nabla_{\vec{x}} p(\vec{x}, t, \theta) = -\lambda(m_b) p(\vec{x}, t, \theta)$$
$$+ \lambda(m_b) \int_{-\pi}^{\pi} k(\theta, \tilde{\theta}, m_b) p(\vec{x}, t, \tilde{\theta}) d\tilde{\theta}. \tag{5.2}$$

where we use periodic boundary conditions given by,

$$p(0, y, t, \theta) = p(L, y, t, \theta); \ p(x, 0, t, \theta) = p(x, L, t, \theta), \tag{5.3}$$

or we use bounce back boundary conditions (described in detail at the end of Section 3.4), where $\vec{x} \in R^2$, $t > 0$, and $\theta \in S^1 = [-\pi, \pi]$. In Section 5.1, we state an existence and uniqueness result for the transport equation (5.2) in $\mathbb{R}^2$, and in Section 5.2 we describe the numerics used to simulate equation (5.2). Then, in Section 5.3, we show results of simulations for the case where $S_{MT} =$ constant everywhere in the domain. In this case, we consider a non-processive motor type (one that does not walk along MTs), but is able to cross-link MTs, aiding in MT realignment. Finally, in Section 5.4, we show results for the case

where MT sliding and treadmilling occur at different rates. Here, we consider the case where we have either one type of processive motor, or two types of processive motors (motors with opposite directionality). In both sections 5.3 and 5.4, we run simulations using either periodic boundary conditions as in equation (5.3) (representing a very large domain), or bounce back boundary conditions, as described by equations (3.18) and (3.19)(representing a smaller domain with boundary).

5.1 Existence and uniqueness result for the transport model in $\mathbb{R}^2$

We begin by defining the shift operator (also referred to as the advection operator) as

$$A = S_{MT}(\hat{\theta} \cdot \nabla),$$

where the domain of A is defined by

$$D(A) = \{\varphi \in L^2(R^2 \times \hat{\theta}) : \varphi(\cdot, \hat{\theta}) \in H^1(R^2)\},$$

and consider the transport equation (5.2) without the turning terms (i.e., $\lambda(m_b) = 0$),

$$\frac{\partial p(\vec{x}, t, \theta)}{\partial t} = Ap(\vec{x}, t, \theta). \tag{5.4}$$

Equation (5.4) is called an advection equation, and the following theorem (taken from Pazy [48]) is an existence and uniqueness result based on semigroup methods for such an equation.

Theorem 5.1: *(Existence and Uniqueness of Solutions to Advection Equation) The operator A generates a strongly continuous semigroup on $L^2(R^2 \times \hat{\theta})$ which solves the advection model $\frac{\partial p}{\partial t} = Ap$ (i.e., $p_t + \hat{\theta} \cdot \nabla p = 0$). The semi-group (solution for positive time) is given by $S(\vec{x}, t; f(\vec{x})) = f(\vec{x} - \hat{\theta}t)$.*

Recall that L and K are defined in the previous chapter by equations (4.13) and (4.15), respectively. Since the turning operator L is linear and bounded, a perturbation result (method outlined in Appendix A) can be applied to

$p_t = Ap + Lp$ to determine an existence and uniqueness result for the full transport model in equation (5.2). The result is given by a second theorem by Pazy [48] (Chapter 3, Theorem 1.1).

Theorem 5.2: *(Existence and Uniqueness of Solutions to Transport Equation)*
Assume $k(\theta, \tilde{\theta}) \geq 0$ (k is a positive function), $\int_{S^1} k(\theta, \tilde{\theta})d\tilde{\theta} = 1$ (k has the normalization property), and $\int_{S^1} \int_{S^1} k(\theta, \tilde{\theta})^2 d\theta d\tilde{\theta} = ||K||^{L^2}_{L^2(S^1 \times S^1)} < \infty$ (K is a Hilbert-Schmidt operator), then for each initial condition $p(0) \in D(A) \; \exists$ a unique solution of the transport equation given (5.2) in the space $X = C^1([0, \infty), L^2(R^2 \times \hat{\theta})) \cap C([0, \infty), D(A))$.

Recall that our choice for k is

$$k(\theta, \tilde{\theta}) = \frac{1}{2\pi I_0(\alpha(m_b))} \exp(\alpha(m_b)\cos(\theta - \mu)). \tag{5.5}$$

Showing that k is positive, and that k has the normalization property is trivial, and so we are left to show that k is a Hilbert Schmidt Operator. That is,

$$\int_{S^1} \int_{S^1} [\frac{1}{2\pi I_0(\alpha(m_b))} \exp(\alpha(m_b)\cos(\theta - \mu))]^2 d\theta d\tilde{\theta}$$

$$= \int_{S^1} d\tilde{\theta} \int_{S^1} [\frac{1}{2\pi I_0(\alpha(m_b))} \exp(\alpha(m_b)\cos(\theta - \mu))]^2 d\theta$$

$$= 2\pi [\frac{1}{2\pi I_0(\alpha(m_b))}]^2 \int_{S^1} \exp(2\alpha(m_b)\cos(\theta - \mu))d\theta$$

$$< \infty.$$

5.2 Set-up for numerical simulations of the transport model

Here we describe the numerical set-up for simulation of the transport equation given by equation (5.2). Table 5.1 gives a list of model parameters used in simulation of this simplified model. Here, we fix the maximum MT switching parameter λ_{max} (see Table 5.1 for value), and describe MT patterns formed for high and low motor activity parameter C, as well as for varying gliding speeds S_{MT}. In this case, the gliding speed is comprised of treadmilling and

sliding speeds, $S_{treadmill}$ and S_{slide}, respectively. In particular, where motors are not present, $S_{MT} = S_{treadmill}$, and where motors are present (and they are processive motors), $S_{MT} = S_{treadmill} + S_{slide}$ (again, see Table 5.1 for these values).

Table 5.1: Table of model parameters for stationary motors.

Model parameter	value	source
high treadmilling speed $S_{treadmill}$ (*in vivo*)	$0.12\mu/sec$	[54]
low treadmilling speed $S_{treadmill}$ (*in vitro*)	$0.04\mu/sec$	[54]
low sliding speed S_{slide} (by kinesin-5)	$0.04\mu/sec$	[59]
medium sliding speed S_{slide}	$0.08\mu/sec$	took $\approx$ average
high sliding speed S_{slide} (by NCD)	$0.1\mu/sec$	[59]
High activity parameter C	25	This paper
Low activity parameter C	0.1	This paper
Max switching rate λ_{max}	$0.05/sec$	This paper

Figure 5.1 represents different types of motor distributions, where red represents the presence of motors (at a density of $1.0\mu m^{-2}$), and blue represents the absence of motors. Figures 5.1(a) and (b) illustrate different cytoplasmic motor distributions, while Figure 5.1(c) illustrates motors only at the cell center, Figure 5.1(d) illustrates motors at the boundary, and Figure 5.1(e) illustrates motors at the center and at the boundary. The reason why we choose distributions is that, in certain cells and for various cell-cycle stages, motors are found to be distributed throughout the cell cytoplasm (as shown in Figures 5.1(a) and (b)). However, for other cell types (and during particular cell-cycle stages), certain motors are found to reside primarily at the centrosome (the center of the cell) [8] and/or at the cell boundary [27] (as shown in Figures 5.1(c), (d), and (e)). Note that if there are no motors on the boundary, MTs will stick to the boundary once they reach it because they are not able to change orientation.

For MTs, we consider the initial condition as shown in Figure 5.2. This initial condition for MTs will be used in all simulations. Figure 5.2(a) illustrates the initial MT density, which is chosen to be approximately uniform throughout the entire domain ($\approx 5 \ \mu m^{-2}$), Figure 5.2(b) illustrates the initial mean MT orientation at each spatial location, and Figure 5.2(c) illustrates the orientational distribution at each spatial location (each MT is assigned a random
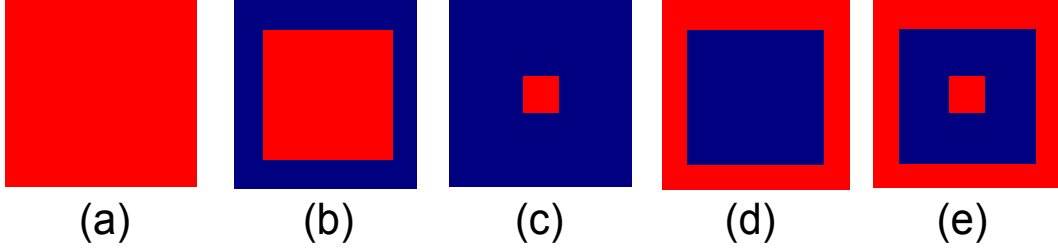
Figure 5.1: Schematic of different configurations for motors. Red describes the presence of motors and blue describes the absence of motors. (a) A uniform distribution of motors throughout the entire domain, (b) MTs absent at the boundaries, (c) MTs at the center of the domain, (d) MTs only at the boundaries, and (e) MTs at the boundary and center of the domain.
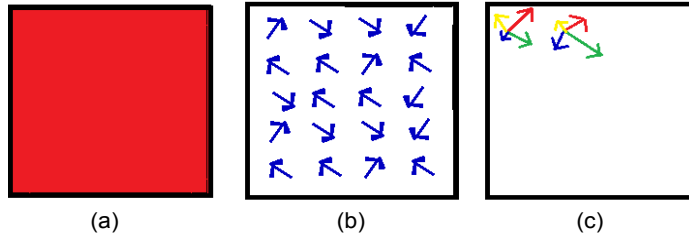
Figure 5.2: A schematic of the initial condition for MTs. (a) MT density (approximately uniform), (b) mean MT orientation at each point in space, (c) and the full MT orientation distribution at each point in space (only two spatial locations chosen as an example).

orientation between π and $-\pi$). Each color represents a different orientation, and the length of the vector is proportional to the density of MTs oriented along that direction. To keep the schematic less clustered, we only show four possible orientations, and 20 spatial locations. However, for our simulations, we allow a total of 64 possible orientations for MTs at each spatial location (each unit is 1.0 μm, so we are looking at a typical cell of size $60 \times 60 \mu m^2$).

5.3 Transport with constant gliding speed S_{MT}

Here we describe results for MT density and alignment patterns that result from large-time simulations of equation (5.2) for constant gliding speed S_{MT}. Recall that MT gliding corresponds to directed transport of MTs along their own axis, and is comprised of two mechanisms, that is, MT treadmilling and MT sliding (caused by motors that are 'stuck' to the domain). We first consider a motor that is not processive, but is still able to crosslink MTs. In this case, the gliding speed is equal to the treadmilling speed everywhere and is constant.

Here, we fix λ_{max} for all simulations, and change the parameters C, S_{MT}, as well as the motor configuration, for each simulation.

We give an illustration, shown in Figure 5.3, of the types of MT patterns that can be observed by simulation of equation (5.2) when S_{MT} is constant. Figure 5.3 Row 1 describes the MT density patterns. In particular MTs can form tight clusters (Row 1(a)), can spread out uniformly in space (Row 1(b)), can form fingering patterns (Row 1(c)), can accumulate completely on the boundary (Row 1(d)), or can accumulate almost completely on the boundary, where some MTs spread out uniformly on the interior (Row 1(e)).

Also, six different global MT alignment patterns are observed, as shown in Figure 5.3 Row 2. MTs can align towards the same angle everywhere in space (Row 2(a)), MTs can align to the zero angle everywhere in space (Row 2(b)), MTs can form patches of alignment (Row 2(c)), they can have mixed orientation (Row 2(d)), can form astral patterns (Row 2(e))(arrows correspond to positive ends), and they can form vortices (Row 2(f)).

Only two different local patterns are found (see Figure 5.3 Row 3). That is, MTs can be bundled, or MTs can form asters at each spatial location (in all results, local alignment is not shown).

All results of simulations for S_{MT} constant are summarized in Tables 5.2 and 5.3. Table 5.2 describes results for periodic MT boundary conditions, and Table 5.3 describes results for bounce back MT boundary conditions. Again, results differ according to variations in the MT treadmilling speed S_{MT}, the alignment parameter C, and the type of motor configuration.

5.3.1   Periodic Boundary Conditions

We first describe results for simulation of equation (5.2) using periodic boundary conditions, described in equation (5.3). Results are shown in Figure 5.4 and 5.5. In this situation, we only consider motor configurations given by Figure 5.1(a) and (c). That is, we consider motors everywhere in the domain, or at a small patch in the domain.

We first investigate the effect of the motor activity C on MT patterning (when treadmilling speed is low). In Figures 5.4(a1) and (b1), we show MT patterns found for low motor activity C and low gliding speed S_{MT} using
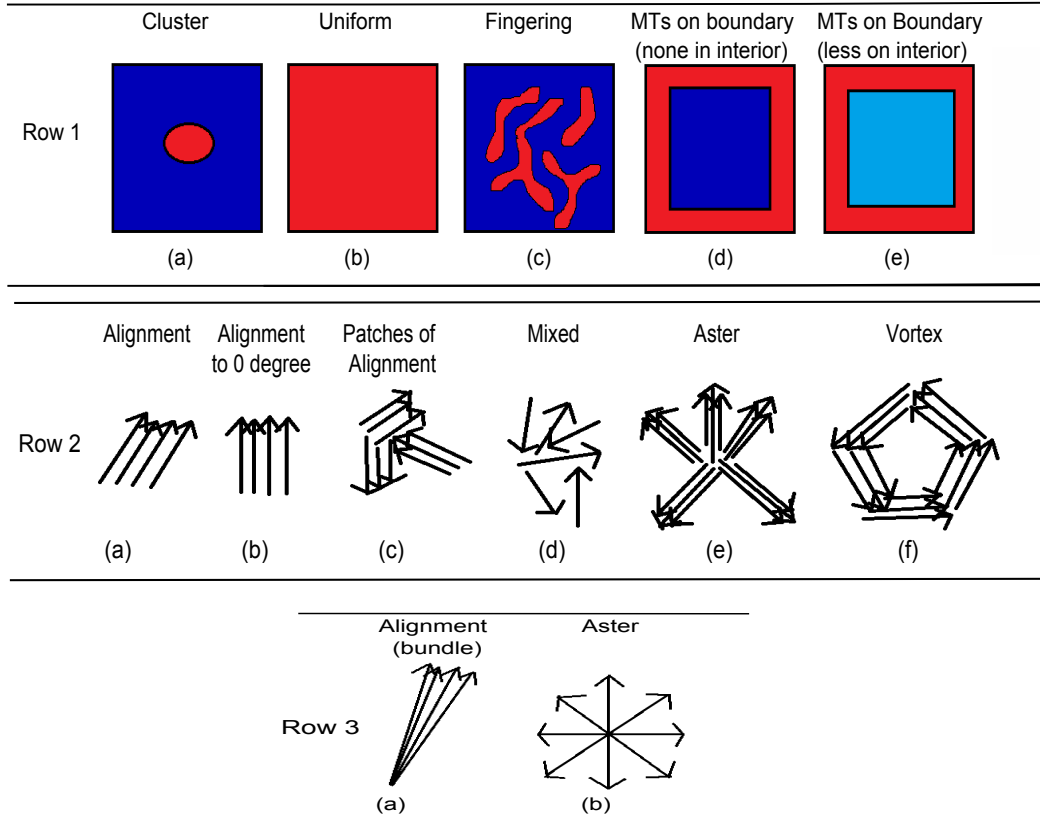
Figure 5.3: Schematic of final MT density patterns (Row 1), global alignment (Row 2), and local alignment (Row 3). Row 1: (a) A single MT cluster, (b) uniform density of MTs, (c) fingering of MTs, (d) all MTs on boundary, and (e) most MTs on boundary, but some MTs on the inside. Row 2: (a) Global alignment of MTs (b) Global alignment to 0 radians (c) patches of alignment, (d) mixed alignment, (e) global aster (all vectors pointing to boundary), and (f) vortices. Row 3: (a) local alignment (bundles), and (b) local asters (uniform distribution).

the motor configuration given by Figure 5.1(a). Here, MTs are located in stationary patches, where they form bundles at high MT density locations and vortices in low MT density locations. This result is consistent with the idea that where more MTs are located, crosslinking (and thus alignment) is able to occur. In Figures 5.4(a2) and (b2), we show results for an increase in C to its high value, keeping all other model inputs the same. Here the patches of alignment become more defined forming what we call 'fingers'. If we increase motor activity, we increase the alignment function α, thus increasing the probability that bundles, such as the fingers seen in Figures 5.4(a2) and (b2), form. This result is similar to that found by Painter in [47].
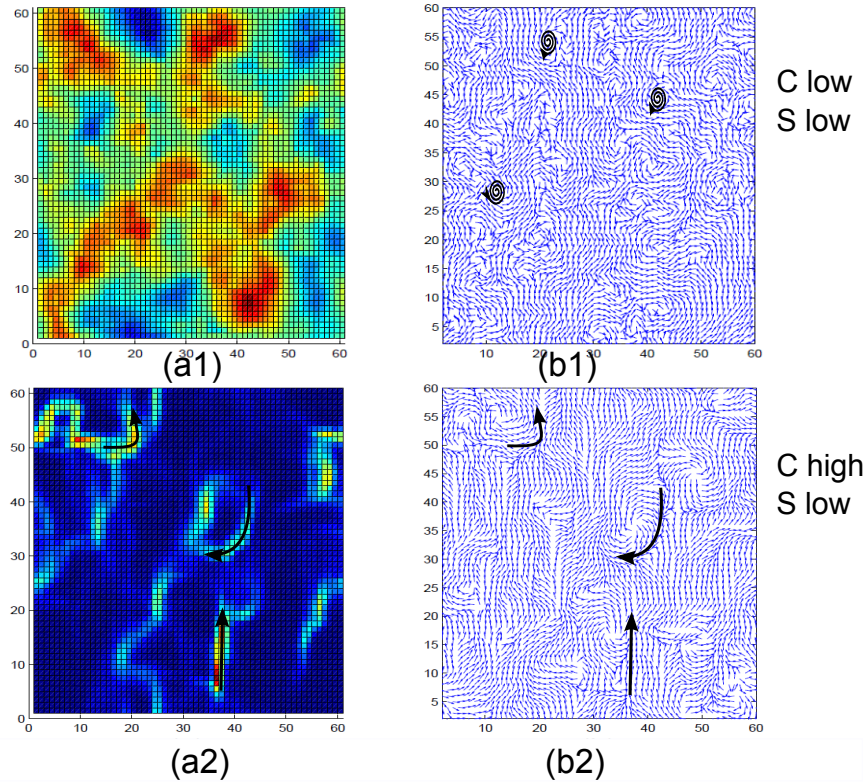
Figure 5.4: (a1) and (b1): Patchy vortex patterns formed for low C, low S_{MT} and motor configuration Figure 5.1(a). (a2) and (b2): Fingering patterns formed for high C, low S_{MT} and motor configuration Figure 5.1(a). Red represents high density and blue represents low density in (a1) and (a2).

Next, we investigate the effect of an increase in gliding speed (treadmilling) on MT pattering, comparing Figure 5.5 (results with high S_{MT}), to the previous Figure 5.4 (results with low S_{MT}). In Figures 5.5(a1) and (b1), we show results for high MT gliding speed S_{MT} and high motor activity parameter C. MTs move quickly, and so stationary patterns like those found in Figure 5.4 are not observed. Instead, MTs group together into a single cluster and travel together along a single direction. This result shows that MT movement (whether MTs are stationary or not) depends on the MT gliding speed (for the motor configuration in Figure 5.1(a)). That is, for high gliding speeds the MTs move, and for low gliding speeds they remain stationary.

Finally, we investigate the effect of motor configuration on MT patterning, comparing Figures 5.5(a1) and (b1) (where motors are distributed throughout
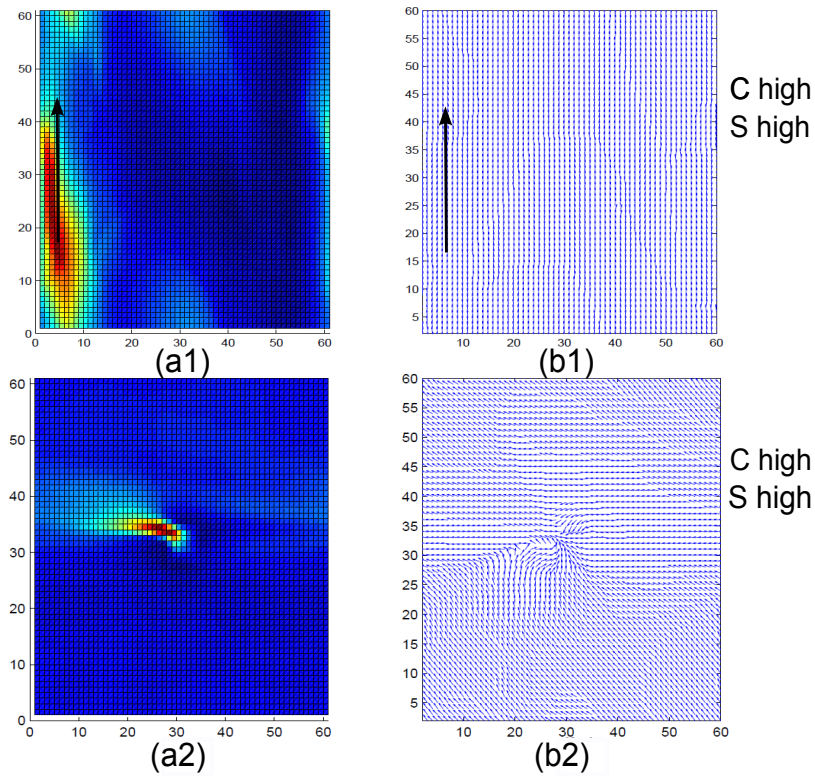
Figure 5.5: (a1) and (b1): Moving cluster formed for high C, high S_{MT} and motor configuration Figure 5.1(a). (a2) and (b2): Stationary cluster formed for high C, high S_{MT} and motor configuration Figure 5.1(c).

the entire domain) with Figures 5.5(a2) and (b2) (where motors are distributed in a small patch at the center of the domain). In Figures 5.5(a2) and (b2), we observe MT patterns for high C, high gliding speed S_{MT}, and using the motor configuration given by Figure 5.1(c). We observe a single stationary MT cluster that is correlated with the location of the motor patch. If we increase the size of this patch, so that it is closer to the patch size shown in Figure 5.1(b), we lose the stability of the stationary cluster, and again have a moving MT cluster similar to that shown in Figures 5.5(a1) and (b1) (results not shown).

(a1) (b1) C low / S low

(a2) (b2) C low / S high
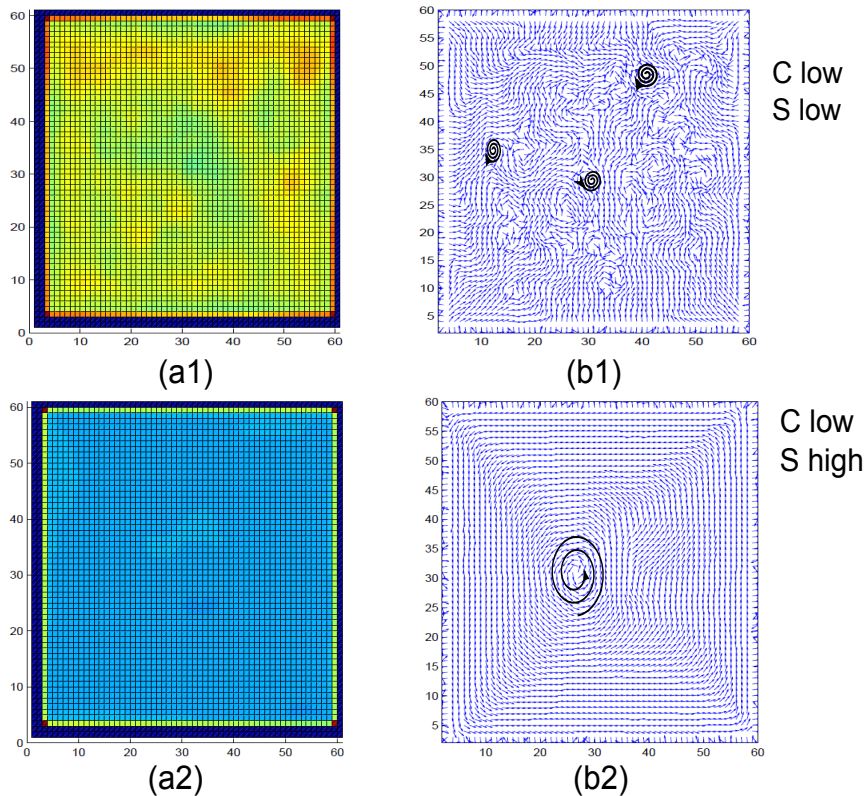
Figure 5.6: (a1) and (b1): Uniform distribution of MTs forming vortex patterns for low C, low S_{MT} and motor configuration Figure 5.1(a). (a2) and (b2): Global vortex formed for low C, high S_{MT} and motor configuration Figure 5.1(c).

5.3.2   Bounce Back Boundary Conditions

In Figures 5.6 and 5.7, we describe long-time patterns found using bounce back boundary conditions described by equations (3.18) and (3.19). First, in Figure 5.6, we explore the effect of gliding (treadmilling) speed on MT patterning. In Figures 5.6(a1) and (b1), we show results for low motor activity C and low gliding speed S_{MT}, using the motor configuration in Figure 5.1(a). Here, a uniform distribution of MTs is found throughout the interior of the domain and these MTs form vortex patterns, where a slightly higher MT density is found on the boundary. In fact, using any of the motor configurations found in Figure 5.1, we find similar results. That is, we find vortex patterns, where vortex location corresponds to motor location (results not shown). If we increase the gliding speed S_{MT}, and place motors at the center of the domain and on the boundary (as shown in Figure 5.1(e)), we produce results as shown in
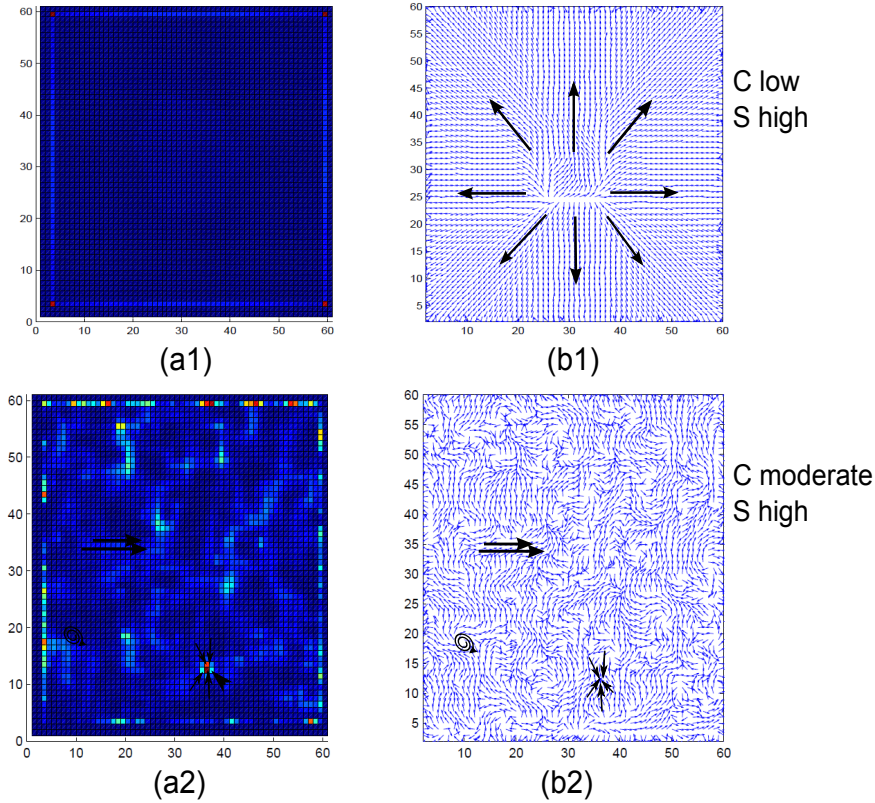
Figure 5.7: (a1) and (b1): Global vortex formed for low C, high S_{MT} and motor configuration Figure 5.1(e). (a2) and (b2): Moving patches of MTs with mixed orientation formed for moderate C, high S_{MT} and motor configuration Figure 5.1(a).

Figures 5.6(a2) and (b2). That is, we find that MTs distribute uniformly on the interior of the domain (with more MTs located on the boundary), and form a global vortex.

Next, in Figures 5.7(a1) and (b1), we show the effect of motor distribution on MT patterning. Here, we show results for low C, high S_{MT}, and the motor configuration described by Figure 5.1(b). In this case, all MTs are found on the boundaries, and the global orientation is an aster. That is, all MTs point towards the boundary. This resulting pattern is found whenever S_{MT} is high and when there are no motors on the boundary of the domain. Also, for any combination of C and S_{MT}, MTs always end up on the boundaries, however the overall orientation may not be an aster (results not shown). When there are no motors on the boundary, MTs are unable to reorient.

Finally, in Figures 5.7(a2) and (b2), we show the effect of motor activity

of MT patterning. In the results shown by Figures 5.6(a1,a2), (b1,b2), and 5.7(a1,b1), we find uniform distributions of MTs located on the interior of the domain. In some cases the MT density is high (as in Figure 5.6(a1)), and in some cases it is very low, even close to zero (as in Figure 5.7(a1)). In fact, for any combination of C and S_{MT} summarized in Table 5.1, and for any motor configuration, we find similar results. To test whether different MT distributions can be observed, we use different motor activity parameters C. In Figures 5.7(a2) and (b2), we choose a moderate value for the motor activity, $C = 10$, high gliding speed, and motor configuration 5.1(a). Here, MTs form transient patches with mixed orientation. These patches are continuously moving, never reaching stability.

Case	S_{MT}	Motor configuration	C	MT density	Global Alignment	Local Alignment
A	high	all	high	Cluster	Alignment	Bundle
B	high	all	low	Uniform	Alignment to 0	Aster
C	low	all	high	Fingering	Mixed	Bundle
D	low	all	low	Fingering	Vortex	Aster

Table 5.2: MTs patterns formed when periodic boundary conditions applied. Descriptions in Figure 5.3.

Case	S_{MT}	Motor configuration	C	MT density	Global Alignment	Local Alignment
E	high	Motors on boundary	high	MTs on boundary (none on interior)	Patches of Alignment	Bundle
F	high	Motors on boundary	low	MTs on boundary (less on interior)	Vortex	Aster
G	high	Motors not on boundary	high	MTs on boundary (none on interior)	Aster	Bundle
H	high	Motors not on boundary	low	MTs on boundary (less on interior)	Aster	Aster
I	low	Motors on boundary	high	MTs on boundary (none on interior)	Patches of Alignment	Bundle
J	low	Motors on boundary	low	MTs on boundary (less on interior)	Mixed	Aster
K	low	Motors not on boundary	high	MTs on boundary (none on interior)	Patches of Alignment	Bundle
L	low	Motors not on boundary	low	MTs on boundary (less on interior)	Mixed	Aster

Table 5.3: MTs patterns formed when bounce back conditions applied. Descriptions in Figure 5.3.

5.4 Transport with spatially dependent gliding speed $S_{MT}(\mathbf{x})$

Here we discuss the effect of a spatially dependent gliding speed on MT patterning, as compared to the case where S_{MT} is constant everywhere. That is, we describe MT patterning in systems where processive motors are present. In this case, MT gliding is a function of MT treadmilling and MT sliding. Similar to the last section, in all cases we show long-time patterns, which refer to steady-state patterns, patterns that are stable and do not change with time.

We first consider the case where we have a single type of processive motor. Here, we assume that the type of motor used is a negative-directed motor (m^-) so that both treadmilling and sliding occur in the same direction (towards the positive end). For this case, we can write the gliding speed $S_{MT}(\mathbf{x})$ as

$$S_{MT}(\mathbf{x}) = S_{treadmill} + S_{slide} * I_D(\mathbf{x}), \tag{5.6}$$

where $I_D(\mathbf{x})$ is the indicator function on the motor domain D, defined by

$$I_D(\mathbf{x}) = \begin{cases} 1 \text{ if } m^-(\mathbf{x}) \neq 0 \\ 0 \text{ if } m^-(\mathbf{x}) = 0 \end{cases},$$

$S_{treadmill}$ is the constant treadmilling speed, and S_{slide} is the constant speed at which motors slide MTs. Values for possible sliding speeds and the treadmilling speed are found in Table 5.1. For simplicity, we only consider the cases where we have motors distributed throughout the entire domain (either randomly, as shown in Figure 5.8(c), or in a checkerboard fashion, as shown in Figure 5.8(a)). Here, the motor density is $1.0 \mu m^{-2}$ where motors are located, and there is an equal ratio of motors to no motors.

As a second example, we consider the case where we have two types of processive motors present (positive- (m^+) and negative- (m^-) directed motors). Here, we consider the gliding speed function given by

$$S_{MT}(\mathbf{x}) = S_{treadmill} - S_{slide} * I_{D+}(\mathbf{x}) + S_{slide} * I_{D-}(\mathbf{x}), \tag{5.7}$$

where S_{slide} is the sliding speed of each motor (either can be low, moderate, or high), and the minus sign accounts for positive-directed motors. Here, $I_{D-}(\mathbf{x})$
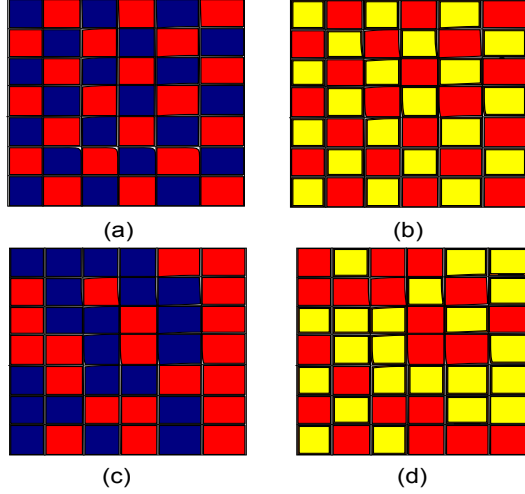
Figure 5.8: Schematic of different configurations for motors. Each square represents one grid point. Here, only 42 grid points are shown (for ease in reading), but in simulations we have 1200. (a) One motor type distributed in a checkerboard fashion. Red describes the presence of motors and blue describes the absence of motors. Each grid point has a constant value. (b) Two motor types distributed in a checkerboard fashion. Red describes one motor type and yellow describes a second motor type with the opposite directionality. (c) One motor type distributed in a random fashion, with an equal ratio of motors to no motors. Red describes the presence of motors and blue describes the absence of motors. (d) Two motor types distributed in a random fashion, with an equal number of each motor type. Red describes one motor type and yellow describes a second motor type with the opposite directionality.

and $I_{D+}(\mathbf{x})$ are defined by,

$$I_{D+}(\mathbf{x}) = \begin{cases} 1 \text{ if } m^+(\mathbf{x}) \neq 0 \\ 0 \text{ if } m^+(\mathbf{x}) = 0 \end{cases},$$

and

$$I_{D-}(x) = \begin{cases} 1 \text{ if } m^-(\mathbf{x}) \neq 0 \\ 0 \text{ if } m^-(\mathbf{x}) = 0 \end{cases}.$$

Again, for simplicity, we only consider the cases where we have each motor distributed throughout the entire domain (either randomly, as shown in Figure 5.8(b), or in a checkerboard fashion, as shown in Figure 5.8(d)). Again, the motor density is $1.0 \mu m^{-2}$, and there is an equal number of each type of motor.

5.4.1 Periodic Boundary Conditions

We first select one motor type (i.e., a negative-directed motor) and distribute motors according to either Figure 5.8(a) or (c). Here, we find that the results

71
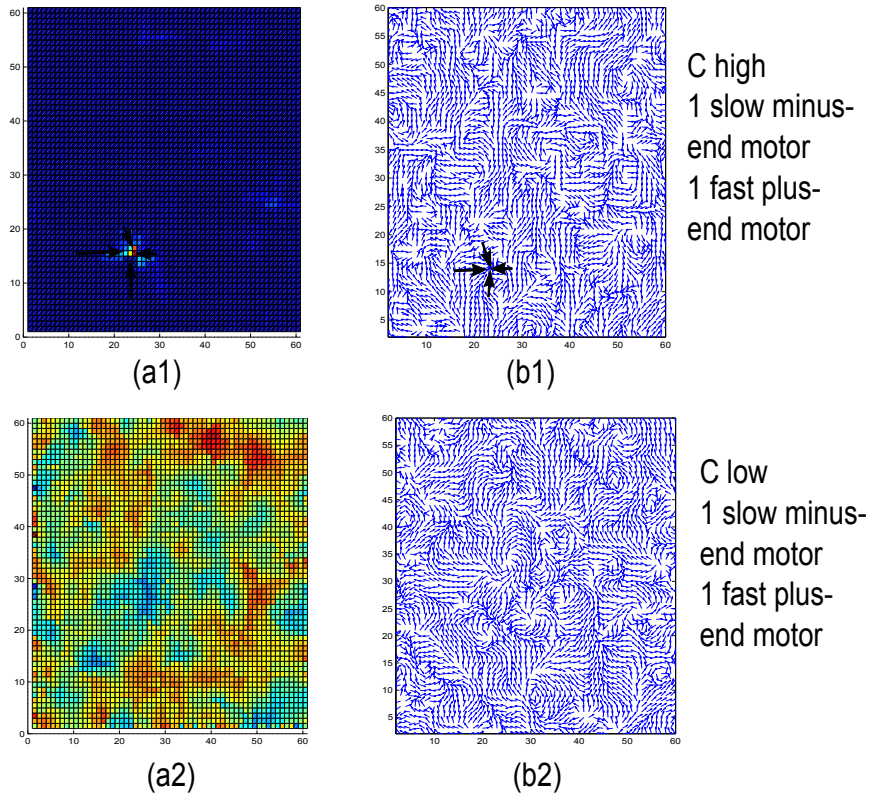
Figure 5.9: (a1) and (b1): Global aster for high C, and fast positive-directed motors and slow negative-directed motors, under the influence of motor configuration Figure 5.8(d). (a2) and (b2): vortices for low C, fast positive-directed motors and slow negative-directed motors, under the influence of motor configuration Figure 5.8(d).

are almost identical to those found in Section 5.3.1. For low C and low sliding speed S_{slide}, we obtain vortices (as in Figures 5.4(a1) and (b1)) (results not shown). For high C and moderate sliding speed, we obtain fingering patterns (as in Figures 5.5(a1) and (b1)) (results not shown). Finally, for a moderate sliding speed, and motors located randomly throughout just the center of the domain (similar to the motor configuration in 5.1(c))), and obtain a result similar to that found in Figure 5.5(a2) and (b2) (results not shown).

When we choose two types of motors with different directionality, we obtain results that are very different from those found in Section 5.3.1. In Figure 5.9, we show results for two types of motors distributed according to either Figures 5.8(b) or (d). Here, using either type of distribution gives similar results, and so we use the motor configuration Figure 5.8(d) for all results illustrated in

72
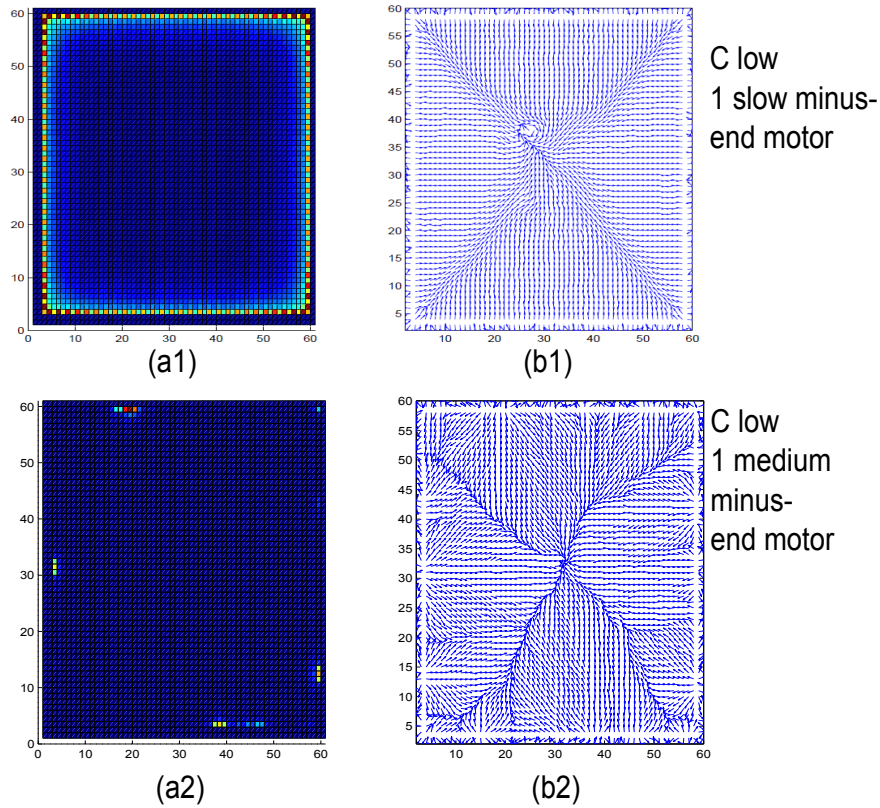
Figure 5.10: (a1) and (b1): Global Vortex for low C, low treadmilling, and one motor type moving MTs at a slow sliding speed under the influence of motor configuration Figure 5.8(a). (a2) and (b2): Global Vortex for low C, low treadmilling, and one motor type moving MTs at a slow sliding speed under the influence of motor configuration Figure 5.8(c).

Figure 5.9. In particular, we obtain asters, or arrays of vortices. When we choose a high motor activity C, a high sliding speed S_{slide} for the positive-directed motors, and a low sliding speed S_{slide} for the negative-directed motors, we get a single stable aster, as shown by Figures 5.9(a1) and (b1). If we choose a fast positive-directed motor type and a slow minus-directed motor type, but this time choose a low motor activity C, we get an array of vortices, as shown in Figure 5.9(a2) and (b2). Also, the results found here are qualitatively similar if we choose two opposite directed motors with the same sliding speed S_{slide}, either low or moderate (results not shown).
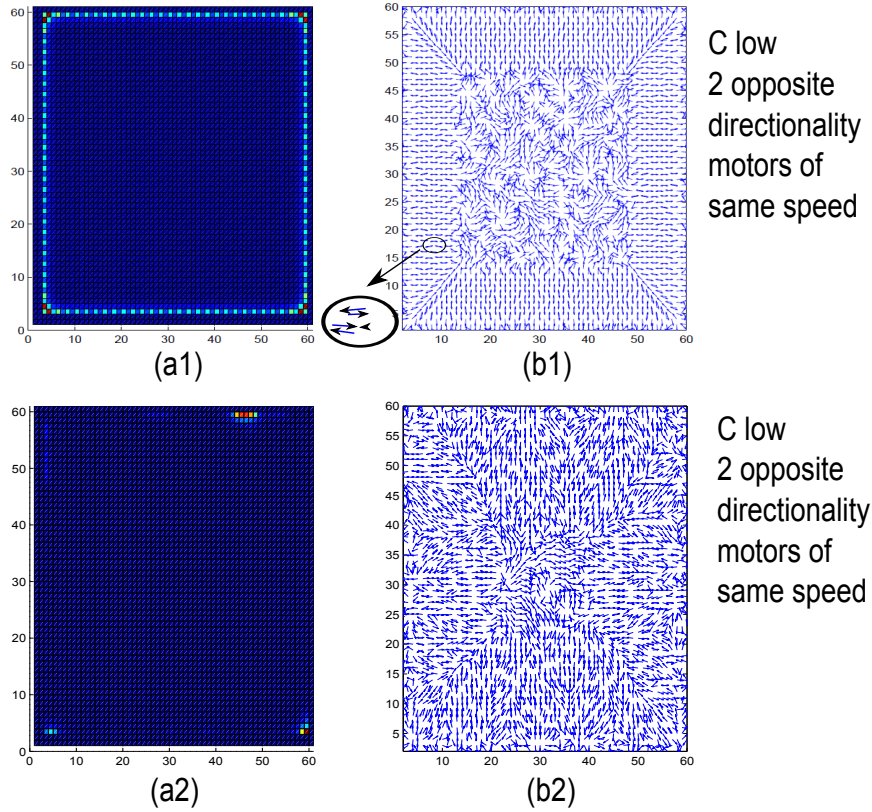
Figure 5.11: (a1) and (b1): Anti-parallel bundling for low C, low treadmilling and two motors (as in Figure 5.8(b)) moving MTs at the same moderate sliding speeds but with opposite directionality. (a2) and (b2): Anti-parallel bundling for low C, low treadmilling and two motors (as in Figure 5.8(d)) moving MTs at the same moderate sliding speeds but with opposite directionality.

5.4.2 Bounce Back Boundary Conditions

We first show results for when one type of motor is present (minus-end directed motors, so that sliding occurs in the positive direction) as in Figure 11(a) or 11(c). Using either motor distribution gives us similar results, so it does not matter which one we choose (results not shown). Figures 5.10(a1) and (b1) show results for when the motor activity C is low, the motor speed is low, and the motor distribution corresponds to a checkerboard pattern as in Figure 5.8(a). Figures 5.10(a2) and (b2) show results for when the motor activity is low, the motor speed is moderate, and motors are distributed at random as described in Figure 5.8(c). Here, we see that as you increase the motor speed the global pattern changes from a stable vortex to a stable aster.

In Figure 5.11, we show results for simulations on domains that have two motor types. We first choose two motors of the same sliding speed (here we choose moderate sliding speeds), but with different directionality. Figures 5.11(a1) and (b1) show results for low motor activity C, using a checkerboard motor distribution as in Figure 5.8(b). We obtain MT distributions where anti-parallel bundles exist close to the boundary of the domain (and a mixed orientation of MTs exists on the interior). Experiments have shown similar results. In particular, gliding assays comprised of two motors with opposing directionality have shown that similar patterns of MTs exist [63, 59, 19]. Figures 5.11 (a2) and (b2) show similar results. Here, we use the same model parameters, but choose a random motor distribution as in Figure 5.8(d). Again, this shows that results are not dependent on the exact organization of the motors.

In Figure 5.12, we show results for simulations on domains with two types of motors that have different speeds. In particular, we choose fast positive-directed motors and slow negative-directed motors. From Figures 5.12 (a1) and (b1), we see that when the motor activity C is low, MTs form astral arrays and are distributed uniformly throughout the interior of domain, where more are located at the boundaries. These results are independent of whether a checkerboard (Figure 5.8(c)) or random motor distribution (Figure 5.8(d)) are used. In Figures 5.12(a2) and (b2), we choose a high motor activity. Here, we see that MTs form mixed distributions of MTs with random orientations.

C low
1 slow minus-
end motor
1 fast plus-
end motor

C high
1 slow minus-
end motor
1 fast minus-
end motor
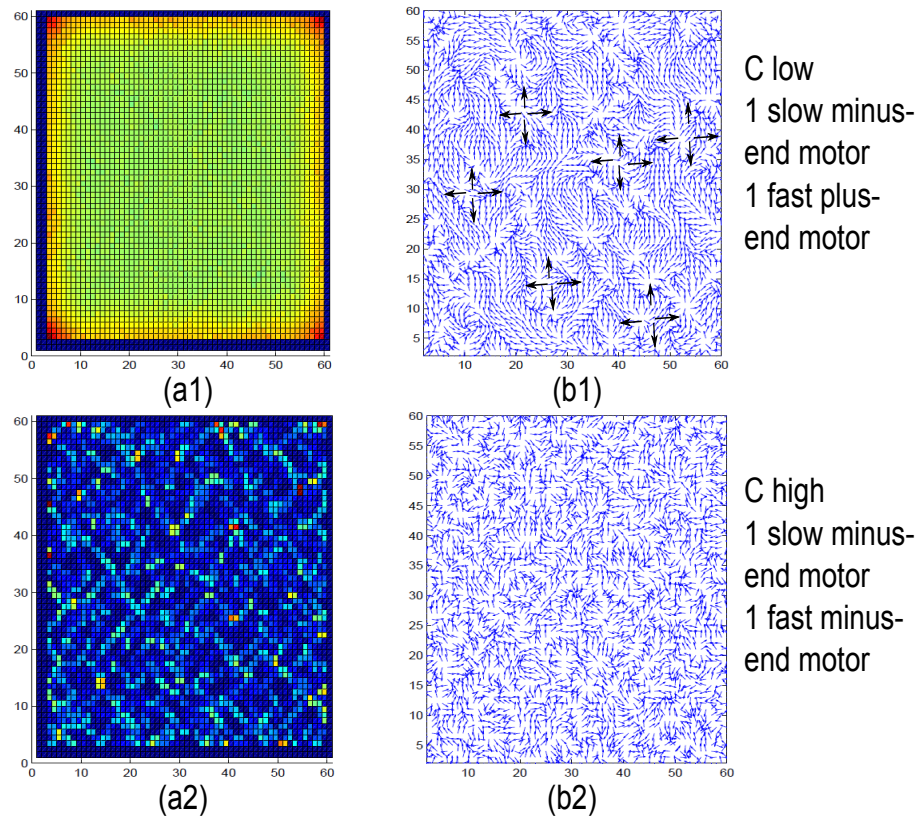
Figure 5.12: (a1) and (b1): Array of asters formed by two motors (as in Figure 5.8(b)) with low C and low treadmilling. Positive-directed motors are moving MTs at high sliding speeds and negative-directed motors are moving MTs at low sliding speeds. (a2) and (b2): Mixed MTs for high C, low treadmilling and two motors (as in Figure 5.8(b)). Similar to above case, positive-directed motors are moving MTs at high sliding speeds and negative-directed motors are moving MTs at low sliding speeds.

Chapter 6

Existence and Uniqueness Result for the Full Model

In this section, we describe an existence and uniqueness result for the full model (described in detail in Chapter 3) given by equations

$$\frac{\partial m_b(\vec{x}, t)}{\partial t} + \nabla_{\vec{x}} \cdot (\mathbf{v}_b m_b(\vec{x}, t)) = k_{on}(\tilde{p}) m_u(\vec{x}, t) - k_{off} m_b(\vec{x}, t), \qquad (6.1)$$

$$\frac{\partial m_u(\vec{x}, t)}{\partial t} - D_u \Delta_{\vec{x}} m_u(\vec{x}, t) = -k_{on}(\tilde{p}) m_u(\vec{x}, t) + k_{off} m_b(\vec{x}, t), \qquad (6.2)$$

$$\frac{\partial p(\vec{x}, t, \theta)}{\partial t} + s_{MT} \hat{\theta} \cdot \nabla_{\vec{x}} p(\vec{x}, t, \theta) = -\lambda(m_b) p(\vec{x}, t, \theta)$$

$$+ \lambda(m_b) \int_{-\pi}^{\pi} k(m_b, \theta, \tilde{\theta}) p(\vec{x}, t, \theta) d\tilde{\theta}, \qquad (6.3)$$

where function $\mathbf{v_b} = ||\mathbf{v_b}|| \int_{S^1} \theta p(\vec{x}, t, \theta) d\theta$ is the bound motor velocity, $k_{on}(\tilde{p}) = k_{on}^{max} \frac{\tilde{p}}{1+\tilde{p}}$ is the density dependent attachment rate of motors to MTs ($k_{on}^{max} > 0$ is the max attachment rate), $\tilde{p}(\vec{x}, t) = \int_{S^1} p(\vec{x}, t, \theta) d\theta$ is the total MT density at each point in space $\vec{x}$ at time t, and $\lambda(m_b) = \lambda_{max} \frac{m_b}{1+m_b}$ is the MT switching rate ($\lambda_{max} > 0$ is the max switching rate). The constant $k_{off} > 0$ is the detachment rate of motors from MTs, $D_u > 0$ is the diffusion rate of unbound motors, and $S_{MT} > 0$ is the constant treadmilling rate.

Here, we consider only periodic boundary conditions on $[0, L] \times [0, L]$,

$$m_b(0, y, t) = m_b(L, y, t),$$
$$m_u(0, y, t) = m_u(L, y, t), \tag{6.4}$$
$$p(0, y, t, \theta) = p(L, y, t, \theta); \ p(x, 0, t, \theta) = p(x, L, t, \theta).$$

The following Theorem 6.1 is a statement of the existence and uniqueness result.

Theorem 6.1: *Consider the model given by equations (6.1) through (6.3) with boundary condition (6.4). If $k_{on}(\tilde{p})$ is Lipschitz continuous in $\tilde{p}$, $\lambda(m_b)$ is Lipschitz continuous in m_b, and if $k(\theta, \theta, m_b)$ is Lipschitz in m_b, there exists a $T > 0$ such that we have a unique solution for $m_b \in L^\infty(\mathbb{D})$, $m_u \in L^\infty(\mathbb{D})$, and $p \in C^1((0, T], L^\infty(\Omega))$ where $\mathbb{D} = (R^2 \times (0, T])$ and $\Omega = R^2$.*

In Section 6.1 we give a brief outline of the proof of Theorem 6.1, and in Sections 6.2 to 6.5 we give a detailed sketch of the proof. For a review of important function spaces, as well as theorems and lemmas used throughout this chapter, please see Appendix A.

6.1 Outline of proof of Theorem 6.1

The coupling of a hyperbolic equation (6.1), a parabolic equation (6.2), and a transport equation (6.3) leads to interesting mathematical challenges. We address those by using the appropriate estimates for each type of equation separately. We define three maps between the Banach spaces

$$X = L^\infty(\mathbb{D}) \quad \text{and } Y = C^1([0, T], L^\infty(\Omega))$$

where $\mathbb{D} = (R^2 \times (0, T])$ and $\Omega = R^2$, as follows:

$$\mathbf{A} : X \times Y \longrightarrow X$$
$$(m_u, \tilde{p}) \longmapsto m_b,$$
$$\mathbf{B} : X \times Y \longrightarrow X$$
$$(m_b, \tilde{p}) \longmapsto m_u, \text{ and}$$
$$\mathbf{C} : X \longrightarrow Y$$
$$m_b \longmapsto \tilde{p}.$$

We write

$$\mathbf{A}(m_u, \tilde{p}) = m_b,$$
$$\mathbf{B}(m_b, \tilde{p}) = m_u, \text{ and}$$
$$\mathbf{C}(m_b) = \tilde{p}.$$

The composition $\mathbf{T}(m_b) = \mathbf{A}(\mathbf{B}(m_b, \mathbf{C}(m_b)), \mathbf{C}(m_b))$ will be a contraction in X for t small enough $(t > 0)$, which leads to existence of a unique solution. The following Sections 6.2 through 6.5 present an outline of the necessary estimates. For all sections that follow, we use the common symbol c for all bounded constants that arise in the estimates. Also, it is important to note that we require slightly higher regularity in the initial condition for p. That is, we consider following initial conditions:

$$m_b(x, 0) \in L^\infty(\Omega), \tag{6.5}$$
$$m_u(x, 0) \in L^\infty(\Omega), \text{ and} \tag{6.6}$$
$$p(x, 0, \theta) \in C^1(\Omega \times S^1). \tag{6.7}$$

6.2   An estimate for m_b

As a first step, we derive an expression for m_b. We begin by considering the case where we are given an $m_u \in X$ and $\tilde{p} \in Y$, and assume that m_b^* is a

79

solution to the equation (6.1). In particular,

$$\frac{\partial m_b^*(\vec{x}, t)}{\partial t} + \nabla \cdot (\mathbf{v_b} m_b^*(\vec{x}, t)) = k_{on}(\tilde{p}) m_u(\vec{x}, t) - k_{off} m_b^*(\vec{x}, t). \tag{6.8}$$

Since $\nabla \cdot (\mathbf{v_b} m_b^*) = \mathbf{v_b} \cdot \nabla m_b^* + (\nabla \cdot \mathbf{v_b}) m_b^*$, we can rewrite equation (6.8) as

$$\frac{\partial m_b^*(\vec{x}, t)}{\partial t} + \mathbf{v_b} \cdot \nabla m_b^*(\vec{x}, t) = -(\nabla \cdot \mathbf{v_b}) m_b^*(\vec{x}, t) + k_{on}(\tilde{p}) m_u(\vec{x}, t) - k_{off} m_b^*(\vec{x}, t). \tag{6.9}$$

The left-hand side of equation (6.9) is an advection term and the right-hand side of equation (6.9) is a reaction term. Such an equation is classified as a hyperbolic equation and so the method of characteristics can be used as a method for describing solutions along characteristics. The characteristic equation is given by

$$\frac{d\vec{x}}{dt} = \mathbf{v_b} = \mathbf{v_b}(\vec{x}, t). \tag{6.10}$$

This equation is a non-autonomous ordinary differential equation (ODE) (an ODE where the right-hand side is a function of the independent variable, in this case t). From local existence results for ODEs, it is sufficient that the right-hand side, $\mathbf{v_b}(\vec{x}, t)$, be Lipschitz in not only the dependent variable $\vec{x}$, but also the independent variable t. Since the motor velocity $\mathbf{v_b}$ is a function of p, as long as $p(\vec{x}, t, \theta)$ is Lipschitz in $\vec{x}$ and t, $\mathbf{v_b}(\vec{x}, t)$ is too.

From the general theory of ODEs, we can define a unique solution operator (sometimes referred to as a flow operator) Φ for the equation (6.10) that takes every initial condition $\vec{x_0}$ to a new spatial position $\vec{x}$. The initial value problem (IVP) for such a solution operator is given by

$$\Phi'(\vec{x_0}) = \mathbf{v_b}, \quad \Phi(\vec{x_0}, 0) = \vec{x_0} \tag{6.11}$$

We substitute the solution $\Phi(\vec{x_0}, t)$ of the IVP (6.11) into equation (6.9) to obtain

$$\frac{dm_b^*(\Phi(\vec{x_0}, t), t)}{dt} = -(\nabla \cdot \mathbf{v_b}(\Phi(\vec{x_0}, t), t)) m_b^*(\Phi(\vec{x_0}, t), t)$$
$$+ k_{on}(\tilde{p}(\Phi(\vec{x_0}, t), t)) m_u(\Phi(\vec{x_0}, t), t) - k_{off} m_b^*(\Phi(\vec{x_0}, t), t). \tag{6.12}$$

The left-hand side of equation (6.12) is called the *material derivative* (i.e., $\frac{dm_b^*(\Phi(\vec{x_0},t),t)}{dt} = \frac{\partial m_b^*(\Phi(\vec{x_0},t),t)}{\partial t} + \mathbf{v_b}(\Phi(\vec{x}_0,t),t)) \cdot \nabla m_b^*(\Phi(\vec{x_0},t),t))$. Reorganizing this equation, by bringing together $m_b^*(\Phi(\vec{x_0},t),t)$ terms, we obtain

$$
\frac{dm_b^*(\Phi(\vec{x_0},t),t)}{dt} + [k_{off} + (\nabla \cdot \mathbf{v_b}(\Phi(\vec{x}_0,t),t))]m_b^*(\Phi(\vec{x_0},t),t)
$$
$$
= k_{on}(\tilde{p}(\Phi(\vec{x_0},t),t))m_u(\Phi(\vec{x_0},t),t). \tag{6.13}
$$

From equation (6.13) we define

$$
A(\Phi(\vec{x_0},t),t) = \exp(\int_0^t (k_{off} + (\nabla \cdot \mathbf{v_b}(\Phi(\vec{x}_0,t),t)))d\tau,
$$

which is uniformly bounded in L^∞. Multiplying the equation (6.13) through by $A(\Phi(\vec{x_0},t),t)$ we arrive at

$$
\frac{dm_b^*(\Phi(\vec{x_0},t),t)}{dt}A(\Phi(\vec{x_0},t),t) + [k_{off} - (\nabla \cdot \mathbf{v_b}(\Phi(\vec{x}_0,t),t)))]
$$
$$
\times m_b^*(\Phi(\vec{x_0},t),t)A(\Phi(\vec{x_0},t),t)
$$
$$
= k_{on}(\tilde{p}(\Phi(\vec{x_0},t),t))m_u(\Phi(\vec{x_0},t),t)A(\Phi(\vec{x_0},t),t), \tag{6.14}
$$

which can be simplified to

$$
\frac{d[m_b^*(\Phi(\vec{x_0},t),t)A(\Phi(\vec{x_0},t),t)]}{dt} = k_{on}(\tilde{p}(\Phi(\vec{x_0},t),t))m_u(\Phi(\vec{x_0},t),t)A(\Phi(\vec{x_0},t),t), \tag{6.15}
$$

a linear equation for m_b^*. Solving the above equation by integrating both sides with respect to t we obtain

$$
m_b^*(\Phi(\vec{x_0},t),t)A(\Phi(\vec{x_0},t),t) - m_b^*(\Phi(\vec{x_0},0),0)A(\Phi(\vec{x_0},0),0)
$$
$$
= \int_0^t k_{on}(\tilde{p}(\Phi(\vec{x_0},s),s))m_u(\Phi(\vec{x_0},s),s)A(\Phi(\vec{x_0},s),s)ds, \tag{6.16}
$$

and, after dividing through by $A(\Phi(\vec{x_0},t),t)$, equation (6.16) simplifies to

$$
m_b^*(\Phi(\vec{x_0},t),t) = m_b^*(\Phi(\vec{x_0},0),0)\frac{1}{A(\Phi(\vec{x_0},t),t)}
$$
$$
+ \int_0^t k_{on}(\tilde{p}(\Phi(\vec{x_0},s),s))m_u(\Phi(\vec{x_0},s),s)\frac{A(\Phi(\vec{x_0},s),s)}{A(\Phi(\vec{x_0},t),t)}ds, \tag{6.17}
$$

81

the solution m_b^* along characteristics (here, $A(\Phi(\vec{x_0}, 0), 0) = 1$ and $t \in (0, T]$). We write (6.17) as

$$
\begin{aligned}
m_b^*(\vec{x}, t) = {} & m_b^*(\Phi(\vec{x_0}, 0), 0) \frac{1}{A(\Phi(\vec{x_0}, t), t)} \\
& + \int_0^t k_{on}(\tilde{p}(\Phi(\vec{x_0}, s), s)) m_u(\Phi(\vec{x_0}, s), s) \frac{A(\Phi(\vec{x_0}, s), s)}{A(\Phi(\vec{x_0}, t), t)} ds,
\end{aligned}
\tag{6.18}
$$

,

where $\Phi(\vec{x_0}, 0)$ denotes the characteristic through $(\vec{x}, t)$, which starts at $\vec{x_0}$. Equation (6.18) defines a continuous map

$$
\mathbf{A} : L^\infty(D) \times C^1((0, T], L^\infty(\Omega)) \longrightarrow L^\infty(\mathbb{D})
$$
$$
(m_u, \tilde{p}) \longmapsto m_b.
$$

To simplify notation, in what follows we let $m_b^{(i)} = m_b^{(i)}(\vec{x}, t)$, $m_u^{(i)} = m_u^{(i)}(\Phi^{(i)}(t), t)$, $\tilde{p}^{(i)} = \tilde{p}^{(i)}(\Phi^{(i)}(t), t)$, $A^{(i)}(t) = A(\Phi^{(i)}(t), t)$, and $k_{on}^{(i)} = k_{on}(\Phi^{(i)}(t), t)$, for $i = 1$, and 2. To apply a contraction argument later, we first need a contraction-like estimate for m_b. For that we assume two pairs of functions $(m_u^{(1)}, \tilde{p}^{(1)})$ and $(m_u^{(2)}, \tilde{p}^{(2)})$ and denote by $m_b^{(i)}$ the corresponding solution of equation (6.18), for $i = 1$ and 2, respectively. Notice that, since $\mathbf{v_b}$ depends on $\tilde{p}^{(i)}$, the characteristics will differ. We denote them by $\Phi^{(1)} = \Phi^{(1)}(\vec{x_0}, t)$ and $\Phi^{(2)} = \Phi^{(2)}(\vec{y_0}, t)$. These two characteristics will stay close, as shown by following:

Integrating both sides of the IVP (6.11) with respect to t from 0 to T_{cross} gives

$$
\Phi(T_{cross}) - \Phi(0) = \| \mathbf{v_b} \| \int_0^{T_{cross}} \tilde{p}(\Phi(s), s) ds. \tag{6.19}
$$

We define T_{cross} to be the location where the characteristics $\Phi^{(1)}(\vec{x_0}, t)$ and $\Phi^{(2)}(\vec{y_0}, t)$ cross (see Figure 6.1).
Now,

$$
\Phi^{(i)}(T_{cross}) - \Phi^{(i)}(0) = \| \mathbf{v_b} \| \int_0^{T_{cross}} \tilde{p}^{(i)} ds,
$$

for $i = 1$ and 2, and so,
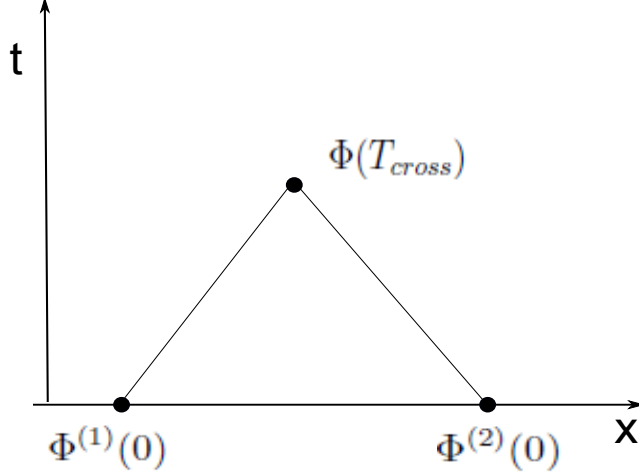
Figure 6.1: Characteristics $\Phi^{(1)}(t)$ and $\Phi^{(2)}(t)$, starting at $\Phi^{(1)}(0)$ and $\Phi^{(2)}(0)$, respectively, cross at time T_{cross} at location $\Phi(T_{cross})$.

$$\Phi^{(1)}(T_{cross}) - \Phi^{(2)}(T_{cross}) = \Phi^{(1)}(0) - \Phi^{(2)}(0) + \parallel \mathbf{v_b} \parallel \int_0^{T_{cross}} \left(\tilde{p}^{(1)} - \tilde{p}^{(2)}\right) ds.$$

Since $\Phi^{(1)}(T_{cross}) = \Phi^{(2)}(T_{cross})$,

$$0 = \Phi^{(1)}(0) - \Phi^{(2)}(0) + \parallel \mathbf{v_b} \parallel \int_0^{T_{cross}} \left(\tilde{p}^{(1)} - \tilde{p}^{(2)}\right) ds.$$

and so,

$$-(\Phi^{(1)}(0) - \Phi^{(2)}(0)) = \parallel \mathbf{v_b} \parallel \int_0^{T_{cross}} \left(\tilde{p}^{(1)} - \tilde{p}^{(2)}\right) ds,$$

or,

$$\Phi^{(1)}(0) - \Phi^{(2)}(0) = -\parallel \mathbf{v_b} \parallel \int_0^{T_{cross}} \left(\tilde{p}^{(1)} - \tilde{p}^{(2)}\right) ds.$$

Thus,

$$|\Phi^{(1)}(0) - \Phi^{(2)}(0)| \leq \parallel \mathbf{v_b} \parallel t |\tilde{p}^{(1)} - \tilde{p}^{(2)}|_{L^\infty}. \tag{6.20}$$

Now, we estimate the distance between two solutions $m_b^{(1)}$ and $m_b^{(2)}$ given $m_u^{(i)} \in L^\infty(\mathbb{D})$ and $\tilde{p}^{(i)} \in C^1((0,T], L^\infty(\Omega))$, for $i = 1$ and 2, using the initial conditions $m_b^{(1)}(\vec{x}, 0) = m_b^{(2)}(\vec{x}, 0) = b(\vec{x})$ (each solution shares the same initial

83

data), which we assume to be Lipschitz continuous and bounded, where

$$
\begin{aligned}
m_b^{(1)}(\vec{x}, t) &= \frac{b(\Phi^{(1)}(0))}{A^{(1)}(t)} \\
&+ \frac{1}{A^{(1)}(t)} \int_0^t A^{(1)}(s) k_{on}^{(1)} m_u^{(1)} ds
\end{aligned}
\tag{6.21}
$$

and

$$
\begin{aligned}
m_b^{(2)}(\vec{x}, t) &= \frac{b(\Phi^{(2)}(0))}{A^{(2)}(t)} \\
&+ \frac{1}{A^{(2)}(t)} \int_0^t A^{(2)}(s) k_{on}^{(2)} m_u^{(2)} ds.
\end{aligned}
\tag{6.22}
$$

That is, we estimate $|m_b^{(1)}(\vec{x}, t) - m_b^{(2)}(\vec{x}, t)|$ as,

$$\left| m_b^{(1)}(\vec{x},t) - m_b^{(2)}(\vec{x},t) \right|_{L^\infty} = \left| \frac{b(\Phi^{(1)}(0))}{A^{(1)}(t)} - \frac{b(\Phi^{(2)}(0))}{A^{(2)}(t)} \right|_{L^\infty}$$

$$+ \int_0^t \left| \frac{A^{(1)}(s)}{A^{(1)}(t)} k_{on}^{(1)} m_u^{(1)} - \frac{A^{(2)}(s)}{A^{(2)}(t)} k_{on}^{(2)} m_u^{(2)} \right|_{L^\infty} ds$$

$$= \left| \frac{b(\Phi^{(1)}(0))}{A^{(1)}(t)} + \frac{b(\Phi^{(2)}(0))}{A^{(1)}(t)} - \frac{b(\Phi^{(2)}(0))}{A^{(1)}(t)} - \frac{b(\Phi^{(2)}(0))}{A^{(2)}(t)} \right|_{L^\infty}$$

$$+ \int_0^t \left| \frac{A^{(1)}(s)}{A^{(1)}(t)} k_{on}^{(1)} m_u^{(1)} - \frac{A^{(2)}(s)}{A^{(2)}(t)} k_{on}^{(2)} m_u^{(2)} \right|_{L^\infty} ds$$

$$= \left| \frac{1}{A^{(1)}(t)} [b(\Phi^{(1)}(0)) - b(\Phi^{(2)}(0))] + b(\Phi^{(2)}(0))[\frac{1}{A^{(1)}(t)} - \frac{1}{A^{(2)}(t)}] \right|_{L^\infty}$$

$$+ \int_0^t \left| \frac{A^{(1)}(s)}{A^{(1)}(t)} k_{on}^{(1)} m_u^{(1)} - \frac{A^{(2)}(s)}{A^{(2)}(t)} k_{on}^{(2)} m_u^{(2)} \right|_{L^\infty} ds$$

$$\leq \frac{1}{min|A^{(1)}(t)|} \left| b(\Phi^{(1)}(0)) - b(\Phi^{(2)}(0)) \right|_{L^\infty} + b(\Phi^{(2)}(0)) \left| \frac{1}{A^{(1)}(t)} - \frac{1}{A^{(2)}(t)} \right|_{L^\infty}$$

$$+ \int_0^t \left| \frac{A^{(1)}(s)}{A^{(1)}(t)} k_{on}^{(1)} m_u^{(1)} - \frac{A^{(2)}(s)}{A^{(2)}(t)} k_{on}^{(2)} m_u^{(2)} \right|_{L^\infty} ds$$

$$\leq \underbrace{\frac{1}{A_{min}^{(1)}} L_b \left| \Phi^{(1)}(0) - \Phi^{(2)}(0) \right|}_{I} + \underbrace{\frac{|b(\Phi^{(2)}(0))|_{L^\infty}}{min|A^{(1)}(t)A^{(2)}(t)|} \left| A^{(1)}(t) - A^{(2)}(t) \right|_{L^\infty}}_{II}$$

$$+ \underbrace{\int_0^t \left| \frac{A^{(1)}(s)}{A^{(1)}(t)} k_{on}^{(1)} m_u^{(1)} - \frac{A^{(2)}(s)}{A^{(2)}(t)} k_{on}^{(2)} m_u^{(2)} \right|_{L^\infty} ds}_{III},$$

where L_b is the Lipschitz constant for b, and $A^{(i)}(t)$ is bounded so that $A^{(i)}(t) \in [A_{min}^{(i)}, A_{max}^{(i)}]$.

Simplifying **I**: Substitution of estimate (6.20) into **I** we obtain,

$$\frac{L_b}{A_{min}^{(1)}} \left| \Phi^{(1)}(0) - \Phi^{(2)}(0) \right| \leq \frac{L_b}{A_{min}^{(1)}} ||\mathbf{v_b}|| t \left| \tilde{p}^{(1)} - \tilde{p}^{(2)} \right|_{L^\infty} \tag{6.23}$$

$$= c_1 t \left| \tilde{p}^{(1)} - \tilde{p}^{(2)} \right|_{L^\infty}.$$

85

Simplifying **II**: The term $\left|A^{(1)}(t) - A^{(2)}(t)\right|$ from **II** can be simplified as

$$
\begin{aligned}
\left|A^{(1)}(t) - A^{(2)}(t)\right|_{L^\infty} &= \left|\exp(\int_0^t [k_{off} + \nabla \cdot \mathbf{v_b}^{(1)}(\Phi^{(1)}(s))]ds) \right.\\
&\quad \left. - \exp(\int_0^t [k_{off} + \nabla \cdot \mathbf{v_b}^{(2)}(\Phi^{(2)}(s))]ds)\right| \\
&\leq c\int_0^t \left|k_{off} + \nabla \cdot \mathbf{v_b}^{(1)}(\Phi^{(1)}(s))\right.\\
&\quad \left. - (k_{off} + \nabla \cdot \mathbf{v_b}^{(2)}(\Phi^{(2)}(s)))\right|_{L^\infty} ds \\
&\leq ct \left|\nabla(\mathbf{v_b}^{(1)}(\Phi^{(1)}(s)) - \mathbf{v_b}^{(1)}(\Phi^{(1)}(s)))\right|_{L^\infty}
\end{aligned}
$$

To finish this estimate, we need to integrate equation (6.3) over S^1. Doing this we obtain

$$
\frac{\partial}{\partial t}\tilde{p} = -S_{MT}\nabla \mathbf{v_b}.
$$

Now, since

$$
\left|\nabla(\mathbf{v_b}^{(1)}(\Phi^{(1)}(s)) - \mathbf{v_b}^{(1)}(\Phi^{(1)}(s)))\right|_{L^\infty} \leq \frac{1}{S_{MT}} \left|\tilde{p}_t^{(1)} - \tilde{p}_t^{(2)}\right|_{L^\infty},
$$

then **II** becomes

$$
\frac{|b|_{L^\infty}}{min\, |A^{(1)}(t)A^{(2)}(t)|} \left|A^{(1)}(t) - A^{(2)}(t)\right|_{L^\infty} \leq c_2 t \left|\tilde{p}_t^{(1)} - \tilde{p}_t^{(2)}\right|_{L^\infty}. \tag{6.24}
$$

Simplifying ***III***:

$$\int_0^t \left| \frac{A^{(1)}(s)}{A^{(1)}(t)} k_{on}^{(1)} m_u^{(1)} - \frac{A^{(2)}(s)}{A^{(2)}(t)} k_{on}^{(2)} m_u^{(2)} \right|_{L^\infty} ds$$

$$\leq c_3 t \left| A^{(1)}(t) - A^{(2)}(t) \right|_{L^\infty} + c_4 t \left| k_{on}^{(1)} - k_{on}^{(2)} \right|_{L^\infty} + c_5 t \left| m_u^{(1)} - m_u^{(2)} \right|_{L^\infty}$$

$$\leq \underbrace{c_1 t^2 \left| \tilde{p}_t^{(1)} - \tilde{p}_t^{(2)} \right|_{L^\infty}}_{\text{from estimate (6.24)}} + \underbrace{c_4 L_{k_{on}} t \left| \tilde{p}^{(1)} - \tilde{p}^{(2)} \right|_{L^\infty}}_{k_{on} \text{ is Lipschitz continous and bounded w.r.t } \tilde{p}}$$

$$+ c_5 t \left| m_u^{(1)} - m_u^{(2)} \right|_{L^\infty}.$$

Putting ***I***, ***II***, and ***III*** together we get

$$\left| m_b^{(1)}(\vec{x}, t) - m_b^{(2)}(\vec{x}, t) \right|_{L^\infty} \leq c_1 t \left| \tilde{p}^{(1)} - \tilde{p}^{(2)} \right|_{L^\infty} + c_2 t \left| \tilde{p}_t^{(1)} - \tilde{p}_t^{(2)} \right|_{L^\infty}$$

$$c_3 t \left| \tilde{p}_t^{(1)} - \tilde{p}_t^{(2)} \right|_{L^\infty} + c_4 t \left| \tilde{p}^{(1)} - \tilde{p}^{(2)} \right|_{L^\infty} + c_5 t \left| m_u^{(1)} - m_u^{(2)} \right|_{L^\infty},$$

and so,

$$\left| m_b^{(1)}(\vec{x}, t) - m_b^{(2)}(\vec{x}, t) \right|_{L^\infty} \leq$$
$$ct \left(\left| \tilde{p}_t^{(1)} - \tilde{p}_t^{(2)} \right|_{L^\infty} + \left| \tilde{p}^{(1)} - \tilde{p}^{(2)} \right|_{L^\infty} + \left| m_u^{(1)} - m_u^{(2)} \right|_{L^\infty} \right). \tag{6.25}$$

6.3   An estimate for m_u

Next, we derive an expression for m_u. We begin by considering the case where we are given an $m_b \in X$ and $\tilde{p} \in Y$, and assume that m_u^* satisfies the equation (6.2), That is,

$$\frac{\partial m_u^*(\vec{x}, t)}{\partial t} - D_u \Delta m_u^*(\vec{x}, t) = -k_{on}(\tilde{p}) m_u^*(\vec{x}, t) + k_{off} m_b(\vec{x}, t). \tag{6.26}$$

The general form of solutions to such a parabolic equation is known [60] and

is given by

$$m_u^*(\vec{x}, t) = \exp(tD_u\Delta)m_u^*(\vec{x}, 0) + \int_0^t \exp((t-s)D_u\Delta)[k_{on}(\tilde{p}(\vec{x}, s))m_u^*(\vec{x}, s)$$

$$+k_{off}m_b(\vec{x}, s)]ds.$$

$$(6.27)$$

Again, we estimate the distance between two solutions $m_u^{(1)}(\vec{x}, t)$ and $m_u^{(2)}(\vec{x}, t)$, for given $m_b^{(i)} \in X$ and $\tilde{p}^{(i)} \in Y$, and initial conditions $m_u^{(1)}(\vec{x}, 0) = m_u^{(2)}(\vec{x}, 0) = a(\vec{x})$.

$$\left| m_u^{(1)}(\vec{x}, t) - m_u^{(2)}(\vec{x}, t) \right|_{L^\infty} =$$

$$\left| \exp(tD_u\Delta)a(\vec{x}) - \exp(tD_u\Delta)a(\vec{x}) \right.$$

$$+ \int_0^t \exp((t-s)D_u\Delta)(k_{on}^{(1)}m_u^{(1)} + k_{off}m_b^{(1)} - k_{on}^{(2)}m_u^{(2)} + k_{off}m_b^{(2)})ds \Big|$$

$$\leq \int_0^t \left| \exp((t-s)D_u\Delta)(k_{on}^{(1)}m_u^{(1)} + k_{off}m_b^{(1)} - k_{on}^{(2)}m_u^{(2)} + k_{off}m_b^{(2)}) \right|_{L^\infty} ds.$$

Now, if we apply the estimate (6.28) (from Taylor [60])

$$|\exp(t\Delta)f|_{L^\infty} \leq c|f|_{L^\infty}, \qquad (6.28)$$

where c is a constant, we obtain

$$\left| m_u^{(1)}(\vec{x}, t) - m_u^{(2)}(\vec{x}, t) \right|_{L^\infty} \leq$$

$$c\int_0^t (c_1|k_{on}^{(1)} - k_{on}^{(2)}|_{L^\infty} + c_2|m_u^{(1)} - m_u^{(2)}|_{L^\infty} + c_3k_{off}|m_b^{(1)} - m_b^{(2)}|_{L^\infty})ds$$

$$\underbrace{ctL_{k_{on}}|\tilde{p}^{(1)} - \tilde{p}^{(2)}|_{L^\infty}}_{k_{on} \text{ is Lipschitz w.r.t } \tilde{p}} + ctk_{off}|m_b^{(1)} - m_b^{(2)}|_{L^\infty} + c\int_0^t |m_u^{(1)} - m_u^{(2)}|_{L^\infty}ds.$$

Gronwall's Lemma [52] then implies,

$$\left| m_u^{(1)}(\vec{x}, t) - m_u^{(2)}(\vec{x}, t) \right|_{L^\infty} \leq (ctL_{k_{on}} |\tilde{p}^{(1)} - \tilde{p}^{(2)}|_{L^\infty} + ctk_{off} |m_b^{(1)} - m_b^{(2)}|_{L^\infty}) \exp(ct). \tag{6.29}$$

Thus, we have our mapping **B** defined by

$$\mathbf{B} : L^\infty(\mathbb{D}) \times C^1((0, T], L^\infty(\Omega)) \longrightarrow L^\infty(\mathbb{D})$$
$$(m_b, \tilde{p}) \longmapsto m_u.$$

6.4 An estimate for p

We derive an expression for p using the equation (6.3). Here, we follow a similar method to that used by Hillen *et al.* [22] Similar to the equation (6.1) for bound motors m_b, this equation is hyperbolic, and so we can use the method of characteristics to determine an expression for p, given $am_b \in X$. For a given θ, we have the characteristic equation

$$\frac{dX_v(t)}{dt} = \vec{v}, \quad X_v(\vec{x}_0, 0) = \vec{x}_0, \tag{6.30}$$

where $\vec{v} = S_{MT}\hat{\theta}$.

Substituting the characteristic $X_v(t)$ into equation (6.3) and writing in terms of the material derivative we arrive at

$$\frac{dp(X_v(t), t, \vec{v})}{dt} + \lambda(m_b(X_v(t), t))p(X(t), t, \vec{v}) = \lambda(m_b(X_v(t), t))$$
$$\times k(m_b(X_v(t), t), \vec{v})\tilde{p}(X(t), t, \vec{v}). \tag{6.31}$$

Since the characteristics depend on $\vec{v} \in V = [S_{MT}^{low}, S_{MT}^{high}] \times S^1$, we cannot simply integrate over S^1. However, we can solve the equation (6.31) by using an integrating factor,

$$\bigwedge(t) = \exp(\int_0^t \lambda(m_b(X_v(s), s))ds).$$

89

Multiplying the equation (6.31) through by this integrating factor and reorganising we arrive at,

$$\frac{d}{dt}\left[p(X_v(t),t,\vec{v})\bigwedge(t)\right] = \bigwedge(t)\lambda(m_b(X_v(t),t))k(m_b(X_v(t),t),\vec{v})\tilde{p}(X_v(t),t).$$
(6.32)

Integrating with respect to time and multiplying through by $\bigwedge^{-1}(t)$, we arrive at

$$\begin{aligned}p(X_v(t),t,\vec{v}) &= \bigwedge^{-1}(t)p(X_v(0),0)\\ &+ \int_0^t \bigwedge(s)\bigwedge^{-1}(s)\lambda(m_b(X_v(s),s))k(m_b(X_v(s),s),v)\tilde{p}(X_v(s),s)ds.\end{aligned}$$
(6.33)

Now, we assume that $(\vec{x},t)$ is given, and that $X_v(t) = \vec{x}_0 + \vec{v}t$ denotes the characteristic through $(\vec{x},t)$. Then, $\vec{x}_0 = X_v(t)-\vec{v}t$ and $X_v(s) = X_v(t)-\vec{v}t+\vec{v}s$, and so our integrating factor is written as

$$\bigwedge(t) = \exp(\int_0^t \lambda(m_b(X_v - \vec{v}t + \vec{v}s,s))ds).$$

and

$$\begin{aligned}p(\vec{x},t,\vec{v}) &= \bigwedge^{-1}p_0(\vec{x}-\vec{v}t)+\\ &\int_0^t \lambda(m_b(\vec{x}-\vec{v}t+\vec{v}s,s))k(m_b(\vec{x}-\vec{v}t+\vec{v}s,s),\vec{v})\tilde{p}(\vec{x}-\vec{v}t+\vec{v}s,s)ds.\end{aligned}$$
(6.34)

This equation describes a continuous map

$$\tilde{\mathbf{C}} : L^\infty(\mathbb{D}) \longrightarrow C^1((0,T],L^\infty(\Omega) \times L^1(S^1))$$
$$m_b \longmapsto p,$$

provided the initial condition is C^1, which we have assumed (from equation (6.8)). Integrating p to $\tilde{p} = \int_V p(\vec{x},t,\vec{v})d\vec{v}$, we obtain a map

$$\mathbf{C} : L^\infty(\mathbb{D}) \longrightarrow C^1((0,T],L^\infty(\Omega))$$
$$m_b \longmapsto \tilde{p}.$$

90

Before obtaining a contraction, we estimate the difference between $\tilde{p}^{(1)}$ and $\tilde{p}^{(2)}$, and between $\tilde{p}_t^{(1)}$ and $\tilde{p}_t^{(2)}$, for a given $m_b^{(1)}$ and $m_b^{(2)} \in X$. We denote $\lambda^{(i)} = \lambda(m_b^{(i)})$, $k^{(i)} = k(m_b^{(i)})$, and $\bigwedge^{(i)} = \exp(\int_0^t \lambda(m_b^{(i)})ds)$, for $i = 1$ and 2, and we write $\bigwedge^{-1}(t)\bigwedge(s) = \bigwedge(s-t)$.

Estimating $\tilde{p}$ first (remember we will need an estimate for $\tilde{p}_t$, too) we obtain,

$$\left|\tilde{p}^{(1)} - \tilde{p}^{(2)}\right|_{L^\infty} \leq \int_V \left|p^{(1)} - p^{(2)}\right|_{L^\infty} dv$$

$$\leq \int_V \left[|p_0|_{L^\infty}\left|\overset{(1)^{-1}}{\bigwedge} - \overset{(2)^{-1}}{\bigwedge}\right|_{L^\infty} + \int_0^t \left|\overset{(1)}{\bigwedge}\lambda^{(1)}k^{(1)}\tilde{p}^{(1)} - \overset{(2)}{\bigwedge}\lambda^{(2)}k^{(2)}\tilde{p}^{(2)}\right|_{L^\infty} ds\right] dv$$

$$\leq \int_V \left[ct|m_b^{(1)} - m_b^{(2)}|_{L^\infty} + \int_0^t \left[c\left|\overset{(1)}{\bigwedge} - \overset{(2)}{\bigwedge}\right|_{L^\infty}\right.\right.$$

$$+ c|\lambda^{(1)} - \lambda^{(2)}|_{L^\infty} + c|k^{(1)} - k^{(2)}|_{L^\infty} + c|\tilde{p}^{(1)} - \tilde{p}^{(2)}|_{L^\infty}\right] ds\right] dv$$

[by repeated insertion and subtraction and the use of

bounds for $|\bigwedge^{(i)}|$, $|\lambda^{(i)}|$, $|k^{(i)}|$, and $|p^{(i)}| < \infty$.]

$$\leq \int_V \left[ct|m_b^{(1)} - m_b^{(2)}|_{L^\infty} + ct^2|m_b^{(1)} - m_b^{(2)}|_{L^\infty} + ct|m_b^{(1)} - m_b^{(2)}|_{L^\infty}\right.$$

$$+ ct|m_b^{(1)} - m_b^{(2)}|_{L^\infty} + c\int_0^t |\tilde{p}^{(1)} - \tilde{p}^{(2)}|_{L^\infty} ds\right] d\theta$$

[using Lipschitz continuity of λ and k]

$$\leq c_1 t|m_b^{(1)} - m_b^{(2)}|_{L^\infty} + c_2 \int_0^t |\tilde{p}^{(1)} - \tilde{p}^{(2)}|_{L^\infty} ds$$

[where $\int_V dv = |V| < \infty$ was added to each constant].

Now, Gronwall's Lemma applies and

$$|\tilde{p}^{(1)} - \tilde{p}^{(2)}|_{L^\infty} \leq c_1 t|m_b^{(1)} - m_b^{(2)}|_{L^\infty} \exp(c_2 t). \tag{6.35}$$

Next we estimate the time derivative $\tilde{p}_t$

$$\left| \tilde{p}_t^{(1)} - \tilde{p}_t^{(2)} \right| \leq \int_V |p_t^{(1)} - p_t^{(2)}| dv$$

$$\leq \int_V \left[|p_0|_{c^1} \left| \overset{(1)}{\bigwedge} - \overset{(2)}{\bigwedge} \right|_{L^\infty} + |p_0|^{L^\infty} \left| \overset{(1)}{\bigwedge}_t - \overset{(2)}{\bigwedge}_t \right|_{L^\infty} \right] dv$$

$$+ \int_V \left| \left[\lambda^{(1)} k^{(1)} \tilde{p}^{(1)} - \lambda^{(2)} k^{(2)} \tilde{p}^{(2)} \right] \right| dv.$$

Since $\bigwedge := \exp(\int_0^t \lambda(m_b(s))ds)$, and since $m_b \in L^\infty$, we have that $\int_0^t \lambda(m_b(s))ds$ is differentiable. Thus $\bigwedge(t)$ is differentiable with Lipschitz constant derivative and

$$\left| \tilde{p}_t^{(1)} - \tilde{p}_t^{(2)} \right|_{L^\infty} \leq ct |m_b^{(1)} - m_b^{(2)}|_{L^\infty} + c|m_b^{(1)} - m_b^{(2)}|_{L^\infty} +$$
$$c|\lambda^{(1)} - \lambda^{(2)}| + c|k^{(1)} - k^{(2)}|_{L^\infty} + c|\tilde{p}^{(1)} - \tilde{p}^{(2)}|_{L^\infty}$$

where again, $|V|$ is added to each constant. We finally arrive at

$$\left| \tilde{p}_t^{(1)} - \tilde{p}_t^{(2)} \right|_{L^\infty} \leq (c_3 t + c_4)|m_b^{(1)} - m_b^{(2)}|_{L^\infty} + \underbrace{cc_1 t |m_b^{(1)} - m_b^{(2)}|_{L^\infty} \exp(c_2 t)}_{\text{from equation (6.35)}}.$$

$$(6.36)$$

6.5 Defining a contraction mapping T

In this section, we define a contraction map **T**. first, we summarize the maps we have found in the previous sections. For $X = L^\infty(\mathbb{D})$ and $Y := C^1((0,T], L^\infty(\Omega))$ we have

$$\mathbf{A} : X \times Y \longrightarrow X$$
$$(m_u, \tilde{p}) \longmapsto m_b,$$
$$\mathbf{B} : X \times Y \longrightarrow X$$
$$(m_b, \tilde{p}) \longmapsto m_u, \text{ and}$$
$$\mathbf{C} : X \longrightarrow Y$$
$$m_b \longmapsto \tilde{p},$$

and we write

$$\mathbf{A}(m_u, \tilde{p}) = m_b,$$
$$\mathbf{B}(m_b, \tilde{p}) = m_u, \text{ and}$$
$$\mathbf{C}(m_b) = \tilde{p}.$$

Given m_b we define

$$\mathbf{T}(m_b) = \mathbf{A}(\mathbf{B}(m_b, \mathbf{C}(m_b)), \mathbf{C}(m_b)).$$

Theorem 6.2: *For $t > 0$ small enough, the map $\mathbf{T} : X \to X$ is a contraction.*

$$\left| \mathbf{T}m_b^{(1)} - \mathbf{T}m_b^{(2)} \right|_{L^\infty} \leq ct \left[|\mathbf{C}(m_b^1) - \mathbf{C}(m_b^2)|_{L^\infty} + (c_3 t + c_4)|m_b^{(1)} - m_b^{(2)}|_{L^\infty} \right.$$

$$\left. + c_1 t |m_b^{(1)} - m_b^{(2)}|_{L^\infty} \exp(c_2 t) + |\mathbf{B}(m_b^{(1)}, \mathbf{C}(m_b^{(1)})) - \mathbf{B}(m_b^{(2)}, \mathbf{C}(m_b^{(2)}))|_{L^\infty} \right]$$

[from equation (6.26) and (6.37)]

$$\leq ct \left[c_1 t |m_b^{(1)} - m_b^{(2)}|_{L^\infty} \exp(c_2 t) + (c_3 t + c_4)|m_b^{(1)} - m_b^{(2)}|_{L^\infty} \right.$$

$$+ c_5 t |m_b^{(1)} - m_b^{(2)}|_{L^\infty} \exp(c_2 t)$$

$$\left. + ct \left[L_{kon} c_1 t |m_b^{(1)} - m_b^{(2)}|_{L^\infty} \exp(c_2 t) + ct k_{off} |m_b^{(1)} - m_b^{(2)}|_{L^\infty} \right] \right]$$

[from equation (6.36)]

$$\leq (c_1 t^2 + c_2 t) \exp(c_3 t) |m_b^{(1)} - m_b^{(2)}|_{L^\infty}$$

$$= C(t)|m_b^{(1)} - m_b^{(2)}|_{L^\infty}$$

[from equation (6.30)],

where $C(t) < 1$ for t small enough. Since $\mathbf{T}$ is a contraction, by Banach's fixed point theorem [52] we have proved Theorem 6.1. That is, there is a unique local solution for $(m_b, m_b, \tilde{p}) \in X \times X \times Y$ for t small enough.

Chapter 7

Numerical Results for the Full Model

In this chapter, we describe numerical results for the full model given by equations (3.1), (3.2), and (3.3). We describe MT patterns that are observed from simulation of these equations using parameter values that represent motor proteins used in MT patterning experiments *in vitro* [58, 19]. The parameters specific to motors are bound motor speed $||\mathbf{v_b}||$, the max attachment rate k_{on}^{max}, and the detachment rate k_{off}. Values for these parameters are found in Table 3.1. Recall from Chapter 3 that the attachment rate $k_{on}(\tilde{p})$ is a function of the total MT density $\tilde{p} = \int_{S^1} p(\vec{x}, t, \theta)d\theta$. From the previous chapter, Chapter 6, we found that $k_{on}(\tilde{p})$ must be bounded with respect to $\tilde{p}$, and we choose

$$k_{on}(\tilde{p}) = k_{on}^{max} \frac{\tilde{p}}{\tilde{p}+1}. \tag{7.1}$$

The values choosen for k_{on}^{max} and k_{off} are based on parameters used in simulations by Nedéléc and Surrey [58]. The parameters in the study of Nedéléc and Surrey are higher than that allowed for stability of solutions (with the numerical scheme that we use), and so we scale them down (by a factor of 5) from their original values $k_{on}^{max} = 50 \ s^{-1}$ and $k_{off} = 1 \ s^{-1}$, keeping their ratio the same (50:1). All other values for k_{off} and k_{on}^{max} are based on these values (for processive motors). For non-processive motors we reverse the values of k_{on}^{max} and k_{off}, and for weakly processive motors we choose values that are roughly the average of the rates for processive and non-processive motors.

For MT dynamics, we choose the max switching rate λ_{max} to be constant, the treadmilling speed S_{MT} to be low, and the motor activity C to be low (values found in Table 3.1). The reason we choose a low C is that we describe MT patterns formed for various values of the motor density (low, moderate, and high), and since the alignment function $\alpha(m_b)$ depends directly on both C and m_b (alignment function given by equation (3.15)), an increase in m_b has a similar effect as an increase in C. Also, we simulate equations (3.1), (3.2), and (3.3) using periodic boundary conditions. The reason for this is that we wish to describe MT patterns in large domains (experiments we compare our simulation results to are completed in large domains). Also, when we describe patterns as being at steady-state, this means that patterns are stable and do not change with time. Such stability is verified by inspection of images after large time simulations.

In Section 7.1, we show results for processive motors. That is, we describe patterns found by simulating equations (3.1) through (3.3) using parameters specific to processive, fast moving, minus-end directed motors and processive, slow moving, positive-end directed motors. We then compare these results to *in vitro* experiments completed by Nedéléc and Surrey [58]. In Section 7.2, we show results for non-processive motors. In particular, we simulate our model using parameters specific to non-processive, fast moving, minus-end directed motors, and we compare these results to experiments completed by Hentrich and Surrey [19]. Finally, in Section 7.3, we show results for weakly processive motors. In particular, we simulate our model using parameters specific to weakly processive, slow moving, positive-end directed motors, and we compare these results to experiments completed by Hentrich and Surrey [19]. A summary of the chapter results is found in Table 7.1.

7.1   Processive motors

In this section, we investigate MT patterning under the influence of processive motors. We choose model parameters such that the bound motor speed $||\mathbf{v_b}||$ is either high or low, the max attachment rate k_{on}^{max} is high, and the detachment rate k_{off} is low.

Figures 7.1 and 7.2 show results for fast, processive, *minus-end* directed

motors. Figure 7.1 illustrates steady-state results for a low density of motors, and Figure 7.2 illustrates steady-state results for a high density of motors. Here we find that, for low or high motor density, MTs form stable, minus-focused asters at steady state, where motors are located at the center of the asters. As we increase the motor density, the number of asters is increased. These results are similar to the experiments of Surrey and Nedéléc [58, 43]. In these experiments, a particular NCD construct is used that is relatively fast (0.2 μ/s) [43] and processive. In these experiments, MTs form minus-end asters and motor proteins are located at the aster centers. Similar to these experimental results, simulated motors are located at the aster centers. However, in Figures 7.1 (a) and 7.2 (a), MT density is lowest at the aster centers. Our simulations produce such results due to the treadmilling term. In particular, MTs treadmill outwards from the aster centers, in the direction of their positive ends.

Similarly, we find that simulations for fast, processive, *positive*-directed motors produce stable positive-focused asters at steady state, where motors are located at the centers of the asters (results not shown). Again, as we increase motor density, the number of asters is increased, and the aster pattern is stable.

If we reduce motor speed $||\mathbf{v_b}||$ to its low value, choose a positive-directed motor, keeping k_{on}^{max} and k_{off} to be the same (high, and low, respectively, corresponding to a processive motor), we find that at small motor densities, MTs form vortex patterns at steady state (see Figure 7.3(b)), and at higher motor densities stable clusters form at steady state (see Figure 7.4(b)). From experiments by Nedéléc and Surrey [58], in systems comprised of a positive-directed kinesin motor, vortices are found at low motor densities, while positive-focused asters are found at higher densities. In this experiment, such a motor is described as being processive and fast. However, we find that vortex patterns are not formed unless the motor is relatively slow. Also, we do not find asters at high motor densities.

7.2 Non-processive motors

A common motor construct that moves very fast in the *negative* direction, but is not processive, is kinesin-14. We choose parameter values such that the bound motor speed $||\mathbf{v_b}||$ is high, the max attachment rate k_{on}^{max} is low, and the detachment rate k_{off} is high.

Figures 7.5 through 7.7 show results for a moderate density of kinesin-14 motors at short (50 time steps), medium (100 time steps), and large time (200 time steps), respectively. Here we see that minus-end focused asters form after short time (see Figure 7.5). At medium time, many of the asters merge to form fewer, larger asters (see Figure 7.6), and finally for large time the asters break down until there are no asters left in the system (see Figure 7.7).

Our simulation results are similar at higher motor densities (results not shown), and are consistent with results by Hentrich and Surrey [19]. The authors show how asters form in systems comprised of kinesin-14 and MTs. At short time there are many asters and, as time advances,the asters merge and so there are fewer of them (see Figure 7.8). It is unclear from this experiment whether the aster pattern becomes stabilized, or if it breaks down completely, as in our simulations.

7.3 Weakly processive motors

Motors that are found to be weakly processive include kinesin-5. Kinesin-5 is a slow moving, *positive*-directed motor [26, 19]. We choose parameters such that the bound motor speed $||\mathbf{v_b}||$ is low, the max attachment rate k_{on}^{max} is moderate, and the detachment rate k_{off} is moderate (parameter values are found in Table 3.1).

Figure 7.9 shows steady-state results for slow moving, weakly processive, positive-directed motors. We find that, for high motor density, motors are able to organize MTs into clusters as shown in Figure 7.9(a). Such clusters do not correspond to asters or vortices. Also, we find that motors correlate to MT location (as shown in Figures 7.9(c) and (d)).

Similar to our results, experiments of MT pattering in the presence of kinesin-5 show that motors are able to organize MTs into tight clusters, where

MTs take on an undefined organization (see Figure 7.10) [19]. In the experiment described in [19], motors correlate with MT location, similar to what we find in our simulations (again, see Figure 7.10).

In our simulations, we found that these clusters become very large, forming wide patches, if we decrease the motor density. Such a result has not been tested experimentally, but would be interesting to verify.
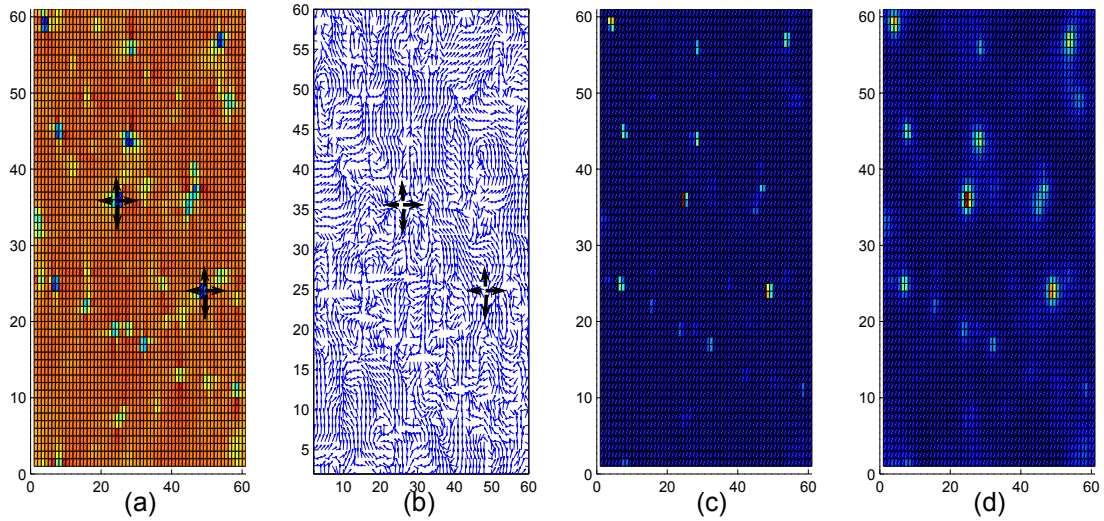
Figure 7.1: Steady-state asters for fast moving, processive, minus-directed motors. Here, $k_{on}^{max} = 10/s$, $k_{off} = 0.1/s$, and $||\mathbf{v_b}|| = 0.12 \ \mu m/s$ and total motor density is $0.5 \mu m^{-2}$. (a) MT density, (b) MT orientation. (c) bound motor density, and (d) unbound motor density.
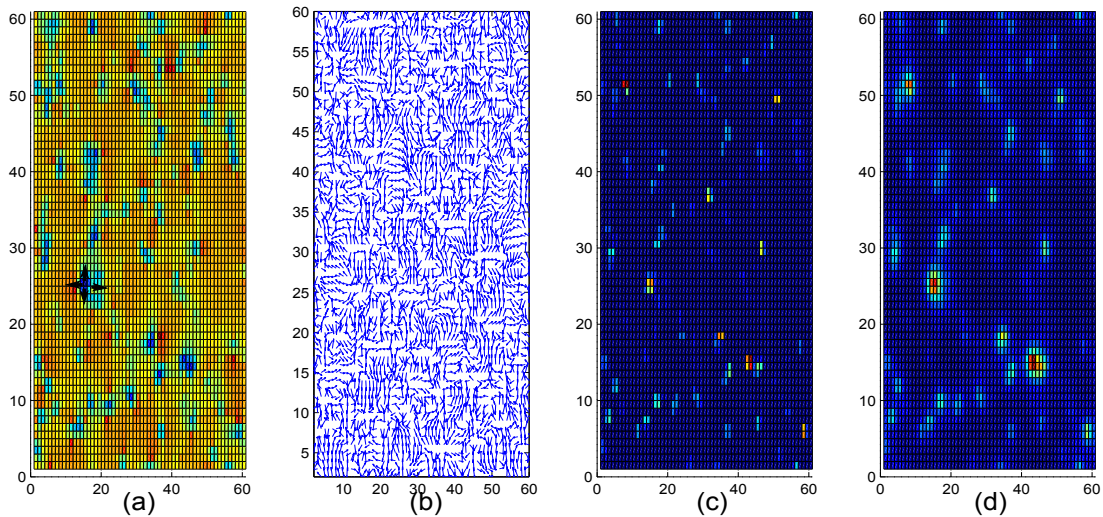

Figure 7.2: Steady-state asters for fast moving, processive, minus-directed motors. Here, $k_{on}^{max} = 10/s$, $k_{off} = 0.1/s$, and $||\mathbf{v_b}|| = 0.12 \mu m/s$ and total motor density is $5\mu m^{-2}$. (a) MT density. MTs are located everywhere in the domain, except at aster centers. (a) MT density, (b) MT orientation. (c) bound motor density, and (d) unbound motor density.
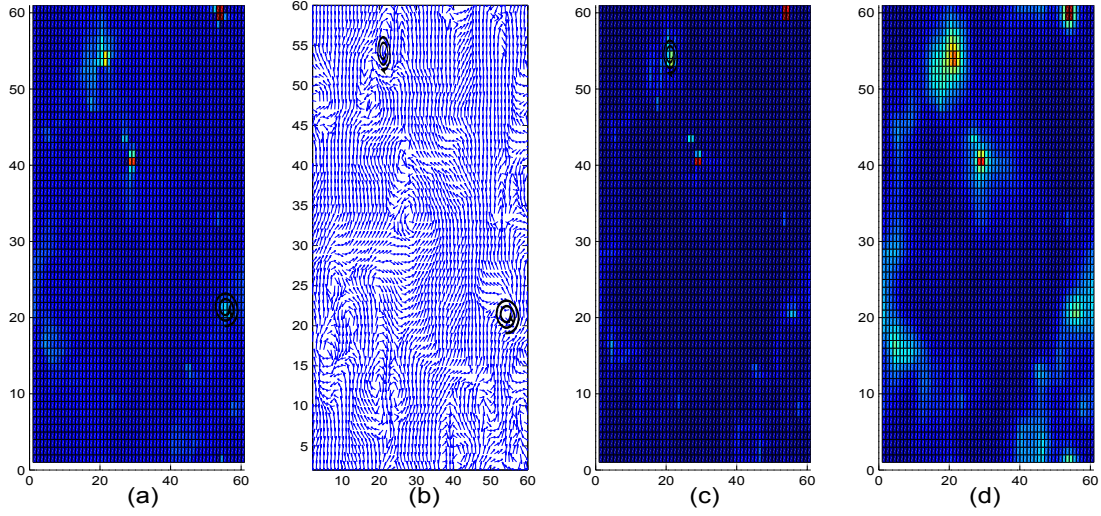
100

Figure 7.3: MTs form vortices in systems comprised of processive, slow moving, positive-directed motors at low motor density. Here, $k_{on}^{max} = 10/s$, $k_{off} = 0.1/s$, and $||\mathbf{v_b}|| = 0.04\mu m/s$ and total motor density is $0.5\mu m^{-2}$. (a) MT density, (b) MT orientation. (c) bound motor density, and (d) unbound motor density.
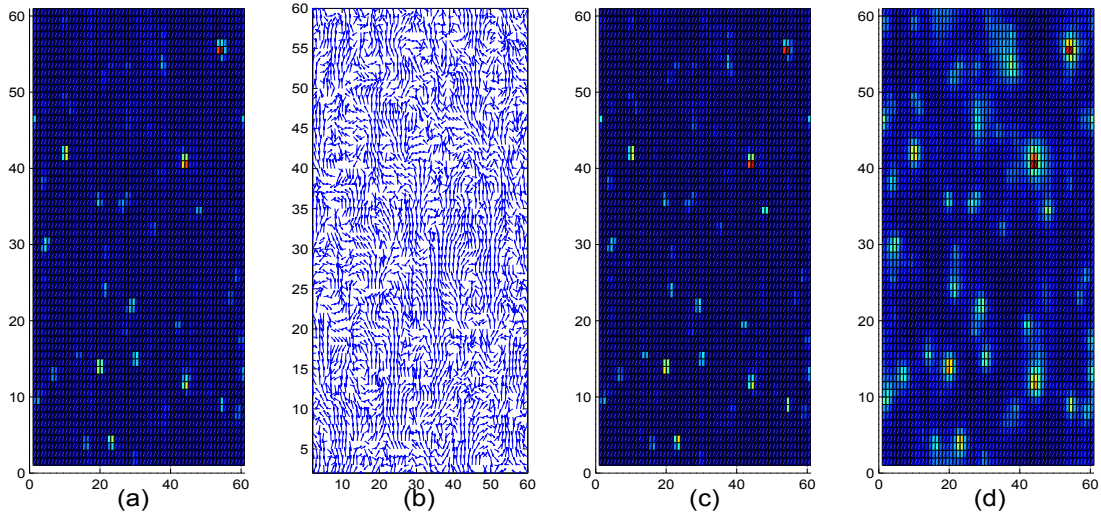

Figure 7.4: MTs form tight clusters in systems comprised of processive, slow moving, positive-directed motors at high motor density. Here, $k_{on}^{max} = 10/s$, $k_{off} = 0.1/s$, and $||\mathbf{v_b}|| = 0.04\mu m/s$ and total motor density is $5\mu m^{-2}$. (a) MT density, (b) MT orientation. (c) bound motor density, and (d) unbound motor density.
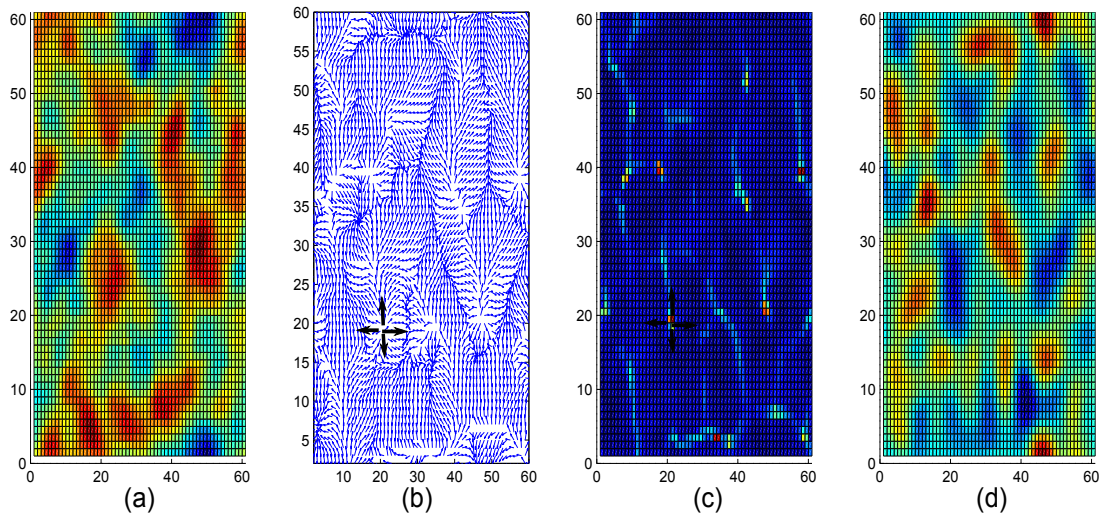
Figure 7.5: MTs form asters at short time (50 time steps) in systems comprised of non-processive, fast moving, negative-directed motors at moderate motor density. Here, $k_{on}^{max} = 0.1/s$, $k_{off} = 10/s$, and $||\mathbf{v_b}|| = 0.12\mu m/s$ and total motor density is $1\mu m^{-2}$. (a) MT density, (b) MT orientation. (c) bound motor density, and (d) unbound motor density.
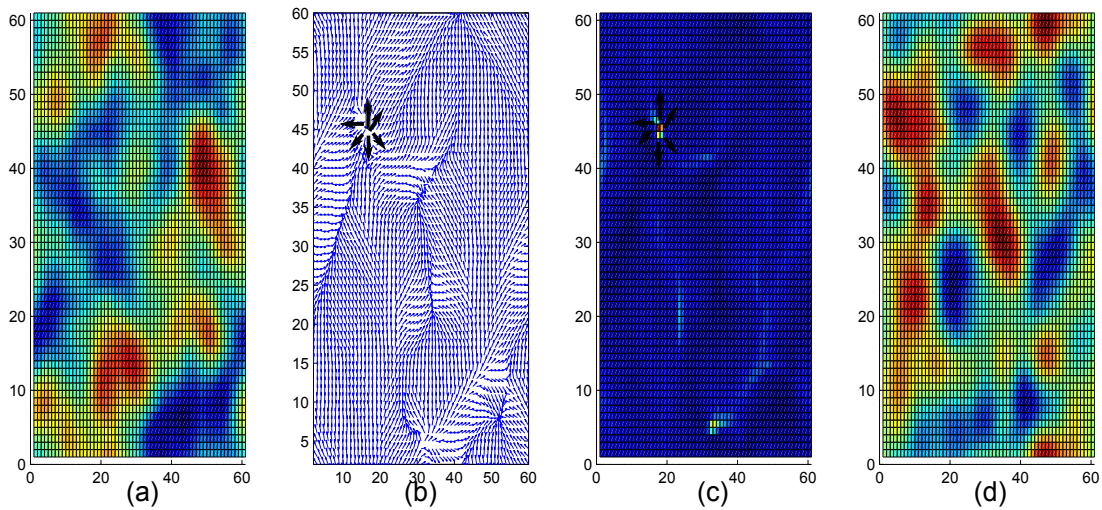
Figure 7.6: MT asters merge and form fewer asters at medium time (100 time steps) in systems comprised of non-processive, fast moving, negative-directed motors at moderate motor density. Here, $k_{on}^{max} = 0.1/s$, $k_{off} = 10/s$, and $||\mathbf{v_b}|| = 0.12\mu m/s$ and total motor density is $1\mu m^{-2}$. (a) MT density, (b) MT orientation. (c) bound motor density, and (d) unbound motor density.
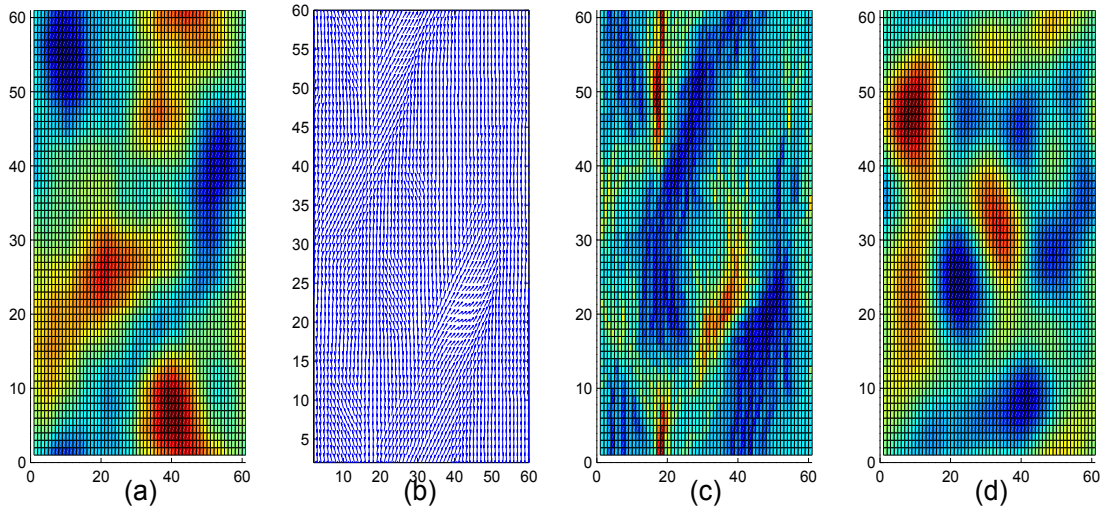
Figure 7.7: MTs disperse from aster configuration after long time (200 time steps) in systems comprised of non-processive, fast moving, negative-directed motors at moderate motor density. Here, $k_{on}^{max} = 0.1/s$, $k_{off} = 10/s$, and $||\mathbf{v_b}|| = 0.12 \mu m/s$ and total motor density is $1 \mu m^{-2}$. (a) MT density, (b) MT orientation. (c) bound motor density, and (d) unbound motor density.
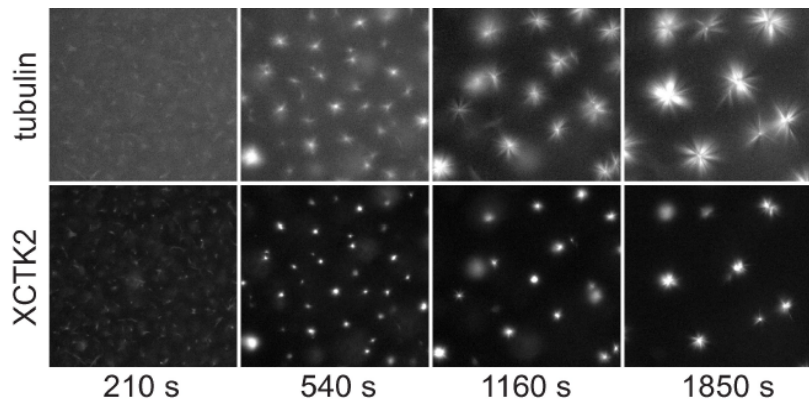

Figure 7.8: Experimental results of MTs form asters in the presence of kinesin-14, a fast moving, non-processive, negative-directed motor [19]. As time elapses, MTs merge, forming larger and fewer asters. Images created using epifluorescence microscopy.
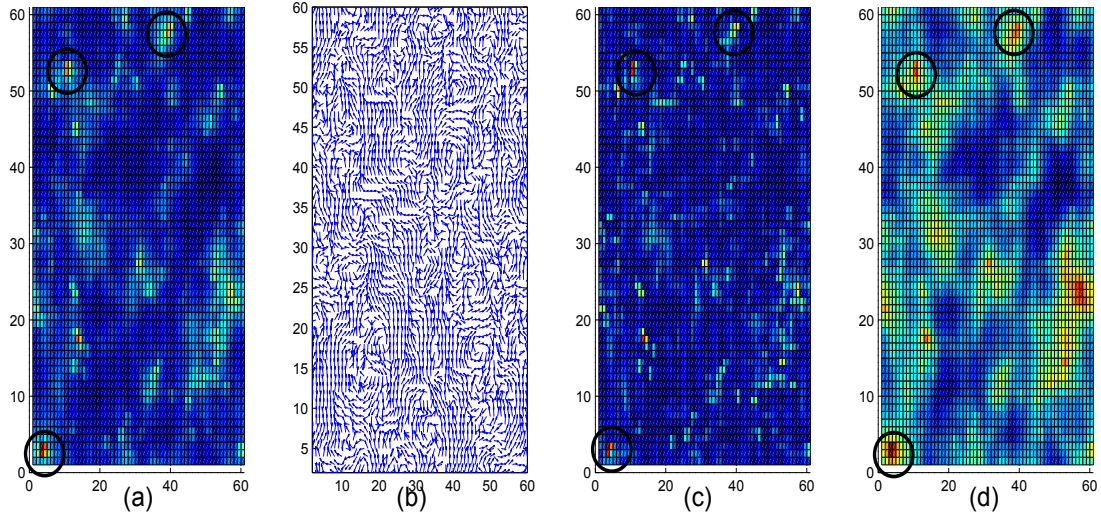
Figure 7.9: Clusters of MTs form at steady-state for slow-moving, weakly processive, plus-end directed motors. Circles highlight locations of MT and motor patches. Here, $k_{on}^{max} = 1.2/s$, $k_{off} = 1.2/s$, and $||\mathbf{v_b}|| = 0.04\mu m/s$ and total motor density is $10\mu m^{-2}$. (a) MT density, (b) MT orientation. (c) bound motor density, and (d) unbound motor density.
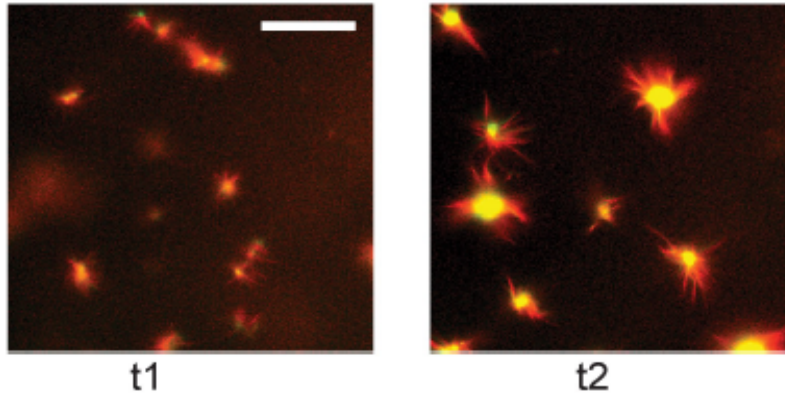

Figure 7.10: Experiments showing how MTs form clusters (with motors at cluster center) in the presence of kinesin-5, a slow moving, weakly processive, positive-directed motor at short time t1 and long time t2 [19]. Images for MTs and motors are merged and created using fluorescence microscopy.

104

Short time MT patterns	Steady-state MT patterns	Motor type	Motor density
negative-focused asters	negative-focused asters	processive, fast, and negative-directed	low or high
positive-focused asters	positive-focused asters	processive, fast, and positive-directed	low or high
vortices	vortices	processive, slow, and positive-directed	low
tight clusters	tight clusters	processive, slow, and positve-directed	moderate or high
negative-focused asters	large patches of aligned MTs	non-processive, fast, and negative-directed	moderate or high
tight clusters	tight clusters	weakly processive, slow, and positive-directed	moderate or high

Table 7.1: Summary of results for simulation of full model given by equation (3.1), (3.2), and (3.3).

105

7.4 Advantages of modelling

In this chapter, we have shown that our mathematical model, describing MT evolution in the presence of motor proteins, can describe MT patterns found *in vitro*. Now that we have made comparisons between our simulation results and experimental results, we can make further predictions for MT pattern formation in the presence of a variety of different motor proteins. Making such predictions takes a relatively short amount of time, and so we have the advantage of being able to come up with a very precise set of conditions under which certain MT patterns will form. Once a desired prediction is made, we can then run experiments to validate our model results. Not only is mathematical modeling time effective, it is also cost effective, as it takes little money to run simulations.

Besides cost and time effectiveness, there are also other advantages to mathematical modelling. One advantage is the ability to track each model variable (in our case MT density p, bound motors m_b, and unbound motors m_u) through space and time. Although imaging techniques have advanced to the point where individual MTs, as well as motor proteins, can be tracked through space and time, it is still very difficult to distinguish between the two different states that a motor can take on (bound or unbound). Using our model, it is easy to describe the locations of bound and unbound motors.

Chapter 8

Conclusion and Discussion

In this thesis, we develop a mathematical model to describe the movement of MTs in 2-dimensions as they interact with motor proteins. Motor proteins are either stationary, or are free to move. In Section 8.1 we outline results of our model when motor proteins are stationary, and in Section 8.2 we outline results corresponding to when motors are moving. Finally, in Section 8.3 we discuss limitations of our modeling approach and discuss future work.

8.1 Interactions of MTs with stationary distributions of motors

In the first part of this study (in Chapter 5), we consider the types of MT patterns that can be observed through simulation of the integro-differential equation (5.2) under the influence of either periodic boundary conditions (equation (5.3)) or bounce back boundary conditions (equations (3.18) and (3.19)), describing the evolution of MTs as they interact with stationary distributions of motor proteins. Such an equation describes how MTs glide, by a combination of MT treadmilling and sliding, and how they reorient in space due to their interactions with motor proteins.

Periodic boundary conditions, though not entirely biologically realistic in two dimensions on small domains, can give some insight into pattern formation on large domains. In the case when we have one motor type (negative directed) that is distributed throughout the entire domain, or is distributed in

a checkerboard or random fashion (as in Figure 5.8(a) or (c), respectively), if the motor activity C is low, and the gliding speed is low, we find MTs organized in wide patches forming arrays of vortices. In contrast, if the motor activity is high, we find fingering patterns. This result suggests that MTs can form stationary long bundles of MTs in large domains when the gliding speed of MTs is small, and the activity of the motor is high. In *vivo*, stationary bundles of MTs are found in systems such as plant cells and neurons [11]. For example, in neurons, the axon of the cell is very long, and along this axon, the majority of MTs are stationary and bundled parallel to one another. In addition to any geometric constraints imposed by the cell membrane, our results indicate that this bundling can occur in a number of ways. The first (described in Section 5.3.1) being through a combination of MT cross-linking by non-processive motors, the second (described in Section 5.4.1) being through a combination of MT sliding where motors are present, and treadmilling where motors are not present. There are a number of types of motors found in neurons, including the mitotic motor kinesin-5. This motor is weakly processive and is able to crosslink MTs, aiding in MT sliding and bundling [26], suggesting that the second mechanism (that described in Section 5.4.1) may be a reasonable theory to explain how MTs bundle in axons.

When periodic boundary conditions are used, it is only when two motor types of opposite directionality are used that an aster pattern, such as that described by Figures 5.9(a1) and (b1), is obtained. When only one motor type is included, only bundles or vortices can be found. This result suggests that a global aster may only form in a large domain if two opposing processive motor types are present.

In the case where bounce back boundary conditions are used, we find that for a single non-processive motor type, where motors are located on the boundary and the motor activity C is low, vortices develop. These vortices exist at low MT density locations. These results can be explained by our choice of the alignment function $\alpha(m)$. This function is directly dependent on MT cross-linking. That is, the higher the cross-linking capability, the more likely it is that MTs align. If fewer MTs are available, then less cross-linking occurs and MTs may move about more freely, being able to form vortex patterns. Also, we find that when a single type of processive negative-directed motor is used,

and motor activity is low, a global vortex forms for low sliding speeds and a global aster forms for moderate sliding speeds. In experiments by Nedélec *et al.* [44], in constrained domains (of different shapes), vortex patterns arise (aster patterns first develop, but due to MT buckling at the boundary, MTs eventually form vortices).

Also, under no conditions do MTs form anti-parallel bundles of MTs when periodic boundary conditions are used. However, we are able to obtain anti-parallel bundles using bounce back boundary conditions and two motor types that move in opposite directions. For our simulations, we chose two motors of similar speed, where MTs treadmill everywhere in space. Anti-parallel bundles do not exist if MT treadmilling is removed from the MT gliding term $S_{MT}(\mathbf{x})$ (results not shown). However, since the treadmilling speed is added to the MT sliding speeds everywhere in space, this result is identical to the result where a fast moving negative-directed motor and a slow positive-directed motor interact and treadmilling does not occur anywhere in space. Thus, our results suggest that there may be at least two possible mechanisms by which anti-parallel bundles form in constrained domains. The first possible mechanism is through the interaction of opposing equal-speed motors in combination with MT treadmilling. The second possible mechanism is through the interaction of fast negative-directed motors and slow positive-directed motors.

Anti-parallel bundles have been observed in *in vitro* gliding assays, where two directionally different motors are used [63, 19, 59]. Such studies are used to determine how the overlap of anti-parallel MTs in the mitotic spindle is formed. It is proposed (from loss-of-function experiments) that the anti-parallel bundles are a result of balanced activities of motors with opposite directionality. In each of these studies, anti-parallel bundles have been formed but not stabilized. Perhaps a reason for this could be that their domain size was too large (remember our simulations show that the boundary is necessary). Also, *in vivo*, anti-parallel bundles form the mitotic spindle as a cell prepares to divide. A number of mitotic motors have been discovered to act on MTs during mitosis. However, it is believed that the slow moving, positive-directed, weakly processive motor kinesin-5, as well as an opposing negative-directed motor type, act between overlapping MTs to form these anti-parallel arrays [55]. Kinesin-5 is able to form crosslinks and has been found to slide MTs relative to one another,

as well as bundle MTs. A possible candidate for the opposing negative-directed motor is kinesin-14 (commonly referred to NCD). Such a motor is very fast, but not processive. However, such a motor stably anchors itself along one MT and is able to generate force (non-processively) along a second MT, aiding in MT bundling. Similar to these experimental findings, our results suggest that systems comprised of an equal number of slow moving positive-directed motors and fast moving negative-directed motors are able to form stable anti-parallel bundles.

8.2 Interactions of MTs with moving motors

In the second part of this study (in Chapter 7), we consider the types of MT patterns that can be observed through simulation of the integro-differential equations (3.1) through (3.3) under the influence of periodic boundary conditions (equation (3.4)), describing the evolution of MTs as they interact with moving distributions of motor proteins. Such a system of equations describes how MTs treadmill, and how they reorient in space due to their interactions with either positive- or negative-directed motor proteins.

Other models have looked at long-term MT patterns that can be observed in systems of moving MTs and moving motors. However, these models differ from ours in that they do not account for motor processivity [2, 3, 24]. Also, the equations for motor movement are non-dimensionalized and do not take into account motor speed. From experiments, we know that processivity, speed, and directionality are important variables to consider [44, 58, 19]. Past theoretical models are similar to ours in that they do take motor density into account [2, 3, 24]. In particular, in such theoretical studies, results have shown that low motor density systems result in vortex patterning, while higher motor density systems result in asters. Also, for very high motor densities, bundled patterns of MTs exist. These results are consistent with past experimental studies in MT systems comprised of varying densities of a single kinesin motor type [44].

However, from other experimental studies of MT patterning, it has been observed that some motor types are not able to organize MTs into vortices at any reasonable motor density, while other motor types are able to orga-

nize MTs into vortices at low motor densities [58]. From our simulations, we show that motor directionality, motor speed, and motor processivity play an important role in determining what types of patterns are able to form.

For processive, fast moving, negative (positive)-directed motors, we find that MTs form stable negative (positive)- focused asters at low and high motor densities. Specifically, we find that such motors are not able to form vortices at any motor density. These results are consistent with those by Surrey and Nedéléc [58], who showed that, for low and high (negative-directed) motor densities, MTs form negative-focused asters (as in Figure 1.7). Similar to our simulation results, the motor type used in the experiments described in [58] is a fast moving, processive, negative-directed motor. Also, in this experiment, results show that motors are located at aster centers, which is consistent with our simulation results.

For processive, slow moving, positive-directed motors, we find that vortices can form at low motor densities. At higher densities, we find that MTs form tight clusters (and not aster patterns). This result is consistent with results by Surrey and Nedéléc [58]. In their experiments, MTs are able to form vortices at low motor densities, but form asters at higher motor densities (as in Figure 1.8). Interestingly, the motor type used in their experiment is a fast moving (and not slow), processive, positive-directed kinesin motor. Also, unlike our simulations, experiments show that asters form at high motor densities, and not clusters (as we show in our simulations).

For non-processive, fast moving, negative-directed motors, we find at moderate to high motor densities, MTs form asters at short time. As time elapses, asters merge, forming larger and fewer asters. Eventually, the aster pattern breaks down for large time. These results are similar to experiments by Hentrich and Surrey [19]. In their experiments, the fast moving, non-processive, negative-directed motor kinesin-14 is able to organize MTs into asters, and as time elapses the asters merge, forming larger and fewer asters (see Figure 7.8). The authors do not suggest whether aster patterns are stable or not for large time. However, our results suggest that such a motor would form similar aster patterns, but after large time these patterns would become unstable.

Finally, for weakly processive, slow moving, positive-directed motors, we find that motors form tight clusters that are correlated with motor location

at moderate to high motor density. Such results are similar to experiments of MT patterning in systems comprised of the weakly processive, slow-moving, positive directed motor kinesin-5 (see Figure 7.10).

8.3   Limitations and future work

One of the limitations of our investigation is that the numerical scheme used to simulate our model is an explicit upwinding scheme for advection (treadmilling), and an explicit central difference scheme for diffusion. Such a scheme puts limitations on the values for motor velocity and motor diffusion that can be tested using our model. For motor velocity, we are able to test motor speeds up to $\approx 0.3\mu m/s$. Such restrictions on speeds are reasonable for slow motors like kinesin-5 and faster motors like kinesin-14 (values recorded in Table 3.1). However, we are unable to test very fast motors such as cytoplasmic dynein (which moves at speeds up to 1.2 $\mu m/s$. Such motors have been found to contribute to MT organization. Also, the diffusion speed must be very small for our model. In reality, motors are able to diffuse much more quickly than represented in our simulations. In future work, it would be a good idea to use an implicit scheme that puts less restrictions on such model parameters.

In this thesis, we consider constant length MTs. In reality, MT are able to grow and shrink, and such dynamics are an important consideration, as it has been shown to alter MT organization. An extension to this model could be to incorporate MT growth and shortening (dynamic instability). To do so, we could include a new independent variable, r, to our model that accounts for the length of each MT. To describe growth and shortening, we could include an advection-type term into the equation for MT movement so that equation (3.3) would read as follows:

$$\frac{\partial p(\vec{x}, t, r, \theta)}{\partial t} + S_{MT}\hat{\theta} \cdot \nabla_{\vec{x}} p(\vec{x}, t, r, \theta) + \frac{\partial}{\partial r}(G(p, r)p(\vec{x}, t, r, \theta)) =$$
$$- \lambda(m_b)p(\vec{x}, t, r, \theta) + \lambda(m_b) \int_{-\pi}^{\pi} k(\theta, \tilde{\theta}, m_b)p(\vec{x}, t, r, \theta)d\tilde{\theta}, \tag{8.1}$$

where $G(p, r)$ represents the growth rate for MTs so that if $G(p, r) < 0$ the
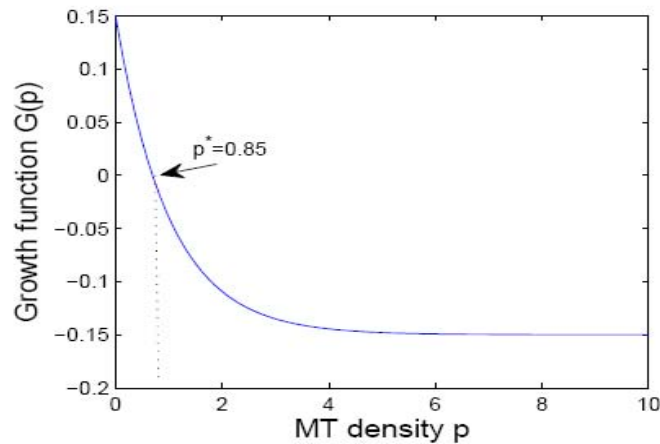
Figure 8.1: An example of $G(p)$. Here, MTs are motor likely to growth when less MTs are present (due to availability of free tubulin) and shrink when more MTs are present (due to overcrowding effects).

MT shrinks and if $G(p, r) > 0$ the MT grows. In general, it has been shown that longer MTs (MTs with larger r) tend to shrink, while shorter MTs (MTs with smaller r) tend to grow. Also, in locations where the MT density p is high, MTs tend to shrink, due to overcrowding affects, whereas if p is low, MTs grow, due to the availability of free tubulin. For simplicity, if we were to choose a growth function that only depends on p, it could be described as in Figure 8.1.

Bibliography

[1] J Allard, G Wasteneys, and E Cytrynbaum. Mechanisms and self-organization of cortical microtubules in plants revealed by computational simulations. *Molecular Biology of the Cell*, 21:278–286, 2010.

[2] I Aranson and L Tsimring. Pattern formation of microtubules and motors: Inelastic interaction of polar rods. *Physical Review*, 71:050901, 2005.

[3] I Aranson and L Tsimring. Theory of self-assembly of microtubule and motors. *Physical Review*, E74:031915:1–15, 2006.

[4] G Bellett, J Carter, J Keynton, D Goldspink, C James, D Moss, and M Mogensen. Microtubule plus-end and minus-end capture at adherens junctions is involved in the assembly of apical-basal arrays in polarised epithelial cells. *Cell Motility and the Cytoskeleton*, 66(10):893–908, 2009.

[5] G Bellett, J Carter, J Keynton, D Goldspink, G James, D Moss, and M Mogenson. Microtubule Plus-End and Minus-End Capture at Adherens Junctions is Involved in the Assembly of Apico-Basal Arrays in Polarized Epithelial Cells. *Cell Motility and the Cytoskeleton*, 66:893–908, 2009.

[6] H Bolterauer, H Limbach, and J Tuszynski. Models of assembly and disassembly of individual microtubules: Stochastics and averaged equations. *Journal of Biological Physics*, 1(15):1–22, 1999.

[7] W Brinkley. Microtubules: A brief historical perspective. *Journal of Structural Biology*, 118(2):84–86, 1997.

[8] A Burokov, O Kovalenko, I Semonova, O Zhapparova, E Nadezhdina, and V Rodionov. Cytoplasmic dynein is involved in the retention of microtubules at the centrosome in interphase cells. *Traffic*, 9:472–480, 2008.

[9] E Cytrynbaum, V Rodionov, and A Mogilner. Nonlocal mechanism of self-organization and centering of microtubule asters. *Bullin of Mathematical Biology*, 68:1053–1072, 2006.

[10] M Dogterom and S Leibler. Physical aspects of the growth and regulation of microtubule structures. *Physical Review*, 70(9):1347–1350, 1993.

[11] M Dogterom and T Surrey. Microtubule organization in *Vitro*. *Current Opinion in Cell Biology*, 25:23–29, 2013.

[12] M Doi, I Yamamoto, and F Kano. Monte carlo simulation of the dynamics of thin rodlike polymers in concentrated solution. *Journal of the Physical Society of Japan*, 53(9):3000–3003, 1984.

[13] O Donal, J Chediack, and E Caviedes-Vidal. Isolation of epithelial cells, villi and crypts from small intestine of pigeons. *Biology of the Cell*, 32(3):219–227, 2008.

[14] R Eftimie. *Modeling Animal Group Formation*. PhD thesis, University of Alberta, 2008.

[15] F Gibbons, J-F Chauwin, M Despósito, and J José. A dynamical model of kinesin-microtubule motility assays. *Biophysical Journal*, 80:2515–2526, 2001.

[16] B Govindan. Steady states of microtubule assembly in a confined geometry. *Physical Review*, 70, 2004.

[17] Y He, F Francis, K A Myers, W Yu, M Black, and P Baas. Role of Cytoplasmic Dynein in the Axonal Transport of Microtubules and Neurofilaments. *Journal of Cell Biology*, 168:697–703, 2005.

[18] Yan He, F Francis, K Myers, W Yu, M Black, and P Baas. Role of cytoplasmic dynein in the axonal transport of microtubule and neurofilaments. *Journal of Cell Biology*, 168(5):697–703, 2005.

[19] C Hentrich and T Surrey. Microtubule organization by the antagonistic mitotic motors kinesin-5 and kinesin-14. *Journal of Cell Biology*, 189(3):465–480, 2010.

[20] T Hill and Y Chen. Phase Changes at the End of a Microtubule With a GTP Cap. *Proceedings of the National Academy of Sciences*, 81:5772–5776, 1984.

[21] T Hillen. M5 mesoscopic and macroscopic models for mesenchymal motion. *Journal of Mathemical Biology*, 53:585–615, 2006.

[22] T Hillen, P Hinow, and Z Wang. Mathematical analysis of a kinetic model for cell movement in tissue networks. *Discrete and Continuous Dynamical Systems Series B*, 14(3):1055–1080, 2010.

[23] P Hollenbeck and D Suter. Axon outgrowth: Motor protein moonlights in microtubule sliding. *Current Biology*, 23(13):R575–R576, 2013.

[24] Z Jia, D Karpeev, I Aranson, and P Bates. Simulation studies of self-organization of microtubules and molecular motors. *Physical Review*, E 77:051905, 2008.

[25] N Johnson and L Kotz. *Distributions in Statistics-Continuous Univariate Distributions*. New York, 2nd edition, 1970.

[26] L Kapitein, E Peterman, B Kwok, J Kim, T Kapoor, and C Schmidt. The bipolar mitotic kinesin eg5 moves on both microtubules that it crosslinks. *Nature*, 435:114–118, 2005.

[27] S Karki and E Holzbaur. Cytoplasmic dynein and dynactin in cell division and intracellular transport. *Current Opinion in Cell Biology*, 11:45–53, 1999.

[28] G Karp. *Cell and Molecular Biology*. John Wiley and Sons, Inc., 1st edition, 1996.

[29] T Keating and G Borisy. Centrosomal and Non-Centrosomal Microtubules. *Biology of the Cell*, 91:321–329, 1999.

[30] J Kim, Y Park, B Kahng, and H Y Lee. Self-organized patterns in mixtures of microtubules and motor proteins. *Journal of the Korean Physical Society*, 42(1):162–166, 2003.

[31] M Kirschner and K. Mitchison. Dynamic Instability of Microtubule Growth. *Nature*, 312:237–242, 1984.

[32] H Y Lee. Macroscopic equations for pattern formation in mixtures of microtubules and molecular motors. *Physical Reviews*, 64:056113, 2001.

[33] R Levayer and T Lecuit. Breaking down emt. *Nature Cell Biology*, 10(7):757–759, 2008.

[34] M Lewis, P Maini, and S Petrovskii. *Dispersal, Individual Movement and Spatial Ecology: A mathematical perspective*, chapter Transport and Anisotropic Diffusion Models for Movement in Oriented Habitats. Springer, Heidelberg, 1st edition, 2012.

[35] H Lodish, A Berk, P Matsudaira, C Kaiser, K Krieger, M Scott, S L Zipursky, and J Darnell. *Molecular Cell Biology*. W H Freeman and Company, 5th edition, 2004.

[36] H Lodish, A Berk, P Matsudaira, C Kaiser, M Krieger, M Scott, S L Zipursky, and J Darnell. *Molecular Cell Biology*. W H Freeman and Company, New York, 5th edition, 2004.

[37] I Maly and G Borisy. Self-organization of treadmilling microtubules into a polar array. *TRENDS in Cell Biology*, 12(10):462–465, 2002.

[38] K Mitchison and M Kirschner. Beyond Self-assembly: From Microtubules to Morphogenesis. *Cell*, 45:329–342, 1986.

[39] T Mitchison and M Kirschner. Microtubule assembly nucleated by isolated centrosomes. *Nature*, 312:232–237, 1984.

[40] T Mitchison, P Nguyen, M Coughlin, and A Groen. Self-organization of stabilized microtubules by both spindle and midzone mechanisms in *Xenopus* egg cytosol. *Molecular Biology of the Cell*, 24:1559–1573, 2013.

[41] A Musch. Microtubule Function and Organization in Epithelial Cells. *Traffic*, 5:1–9, 2004.

[42] A Nascimento, J Roland, and V Gelfand. Pigment cells: A model for the study of organelle transport. *Cell and Developmental Biology*, 19:469–491, 2003.

[43] F Nedelec and T Surrey. Dynamics of Microtubule Aster Formation by Motor Complexes. *Physics at the Scale of the Cell*, 4:841–847, 2001.

[44] F Nedelec, T Surrey, A C Maggs, and S Leibler. Self-Organization of Microtubules and Motors. *Nature*, 389:305–308, 1997.

[45] H Othmer. Notes on space- and velocity-jump models of biological movement. *Theoretical Biology*, 10:913–917, 2010.

[46] H Othmer, S Dunbar, and W Alt. Models of dispersal in biological systems. *Journal of Mathematical Biology*, 26:263–298, 1988.

[47] K Painter. Modelling cell migration strategies in the extracellular matrix. *Journal of Mathematical Biology*, 58:511–543, 2009.

[48] A Pazy. *Semigroups of Linear Operators and Applications to Partial Differential Equations*. Springer-Verlag, New York., 1983.

[49] B Perthame. *Transport Equations in Biology*. Birkhäuser Verlag, Berlin, 2007.

[50] D Porter. *Integral Equations: A Practical Treatment, From Spectral Theory to Applications*. Cambridge University Press, 1990.

117

[51] D Portran, J Gaillard, M Vantard, and M Thery. Quantification of map and molecular motor activities on geometrically controlled microtubule networks. *Cytoskeleton*, doi:10.1002:1–10, 2012.

[52] J Robinson. *Infinite-Dimensional Dynamical Systems*, chapter Ordinary Differential Equations. Cambridge University Press, Cambridge, 1st edition, 2001.

[53] V Rodionov and G Borisy. Self-centering in cytoplasmic fragments of melanophores. *Molecular Biology of the Cell*, 9:1613–1615, 1998.

[54] V Rodionov, E Nadezhdina, and G Borisy. Centrosomal control of microtubule dynamics. *Proceedings of the National Academy of Science*, 96:115–120, 1999.

[55] D Sharp, G Rogers, and J Scholey. Microtubule motors in mitosis. *Nature*, 407:41–47, 2000.

[56] E Shelden and P Wadsworth. Observation and Quantification of Individual Microtubule Behaviour In Vivo:Microtubule Dynamics are Cell-Type Specific. *Journal of Cell Biology*, 120:934–945, 1993.

[57] R Subramanian and T Kapoor. Building complexity: Insights into self-organized assembly of microtubule-based architectures. *Developmental Cell*, doi:10.1002:1–10, 2012.

[58] T Surrey, F Nedelec, S Leibler, and E Karsenti. Physical Properties Determining Self-Organization of Motors and Microtubules. *Science*, 292:1167–1171, 2001.

[59] L Tao, A Mogliner, G Civelekoglu-Scholey, R Wollman, J Evans, H Stahlberg, and J Scholey. A homotetrameric kinesin-5, klp61f, bundles microtubules and antagonizes ncd in motility assays. *Current Biology*, 16:2293–2302, 2006.

[60] M Taylor. *Partial Differential Equations 3*. Springer-Verlag, New York Inc., 1996.

[61] J Thiery. Epithelial-mesenchymal transitions in tumour progression. *Nature*, 2:442–454, 2002.

[62] J Tse and R Kalluri. Mechanisms of metastatsis: Epithelial-to-mesenchymal transition and contribution of tumor microenvironment. *Journal of Cellular Biochemistry*, 101:816–829, 2007.

[63] R Vale, F Malik, and D Brown. Directional instability of microtubule transport in the presence of kinesin and dynein, two opposite polarity motor proteins. *Journal of Cell Biology*, 119:1589–1596, 1992.

[64] T Vignaud, L Blanchoin, and M Thery. Directed cytoskeleton self-organization. *Synthetic Cell Biology*, 22:671–682, 2001.

[65] R H Wade. On and Around Microtubules: An Overview. *Molecular Biotechnology*, 43:177–191, 2009.

[66] P Wadsworth and M McGrail. Interphase Microtubule Dynamics are Cell-Type Specific. *Journal of Cell Biology*, 95:23–32, 1990.

[67] C M Waterman-Storer and E D Salmon. Microtubule Dynamics: Tread-milling Comes Around Again. *Current Biology*, 7:369–372, 1997.

[68] C M Waterman-Storer and E D Salmon. Microtubules: Strange Polymers Inside the Cell. *Bioelectro-Chemistry and Bioenergetics*, 48:285–295, 1999.

[69] E Yokota, S Sonobe, H Igarashi, and T Shimmen. Plant microtubules can be traslocated by a dynein atpase from sea urchin in vitro. *Plant Cell Physiology*, 36(8):1563–1569, 1995.

[70] M-K Yuko. Shaping microtubules into diverse patterns: Molecular connections for setting up both ends. *Cytoskeleton*, 68:603–618, 2011.

[71] J Zhou and P Giannakakou. Targeting Microtubules for Cancer Chemotherapy. *Current Medical Chemistry*, 5:65–71, 2005.

Appendix A

Important Mathematical Concepts

1.1 The spaces of continuous functions

We first introduce the space of continuous functions on Ω, $C^0(\Omega)$. In particular,

$$C^0(\Omega) := \{f : \Omega \to \mathbb{R}, \Omega \subset \mathbb{R}^n \text{ is bounded and open with smooth boundary}\} \tag{1.1}$$

The standard norm on $C^0(\Omega)$ is the supremum norm,

$$\|f\|_\infty = \sup_{x \in \Omega} |f(\mathbf{x})|. \tag{1.2}$$

Such a space defined by (1.1) and equipped with the norm given in (1.2) is complete, and so is a Banach space. Other spaces of continuous functions require higher orders of differentiability. We define the following:

$$|\alpha| = \alpha_1 + \alpha_2 + ... + \alpha_m,$$

where α is a multi-index vector consisting of m nonnegative integers.

$$x^\alpha = x_1^{\alpha_1} x_2^{\alpha_2} ... x_m^{\alpha_m},$$

where x is any vector.

$$D^\alpha = D_1^{\alpha_1} D_2^{\alpha_2} ... D_m^{\alpha_m},$$

where D is the vector, and finally

$$D^\alpha f = \frac{\partial^{|\alpha|} f}{\partial x_1^{\alpha_1} \partial x_2^{\alpha_2} ... \partial x_m^{\alpha_m}}.$$

Now, we define the space of functions f, for which all derivatives up to (and

including) the order r are continuous, $C^r(\Omega)$.

$$C^r(\Omega) := \{f : D^\alpha f \in C^0(\Omega) \;\; \forall \;\; |\alpha| \leq r\}. \tag{1.3}$$

For $C^1(\Omega)$, the space of continuously differentiable functions, the standard norm is the supremum norm on both f and the derivative of f. In particular,

$$\|f\|_{C^1} := \|f\|_\infty + \|f'\|_\infty. \tag{1.4}$$

The space of smooth functions $C^\infty(\Omega)$, that are infinitely differentiable on Ω is defined by,

$$C^\infty(\Omega) := \cap_{r=0}^\infty C^r(\Omega). \tag{1.5}$$

1.2   Lebesgue Spaces L^p and L^∞

We now define the spaces of Lebesque integrable functions, $L^p(\Omega)$, where $1 \leq p \leq \infty$. First, the L^p norm is given by

$$\|f\|_{L^p} = \left(\int_\Omega |f(x)|^p dx \right)^{1/p}. \tag{1.6}$$

A function is in $L^p(\Omega)$ if

$$\left(\int_\Omega |f(x)|^p dx \right)^{1/p} < \infty.$$

The Lebesgue space $L^2(\Omega)$ is of importance to our analysis in Chapter 4. In particular, $L^2(\Omega)$ is a complete inner product space, or Hilbert space ($L^2(\Omega) = H(\Omega)$), when equipped with the inner product $< \cdot, \cdot >: L^2(\Omega) \times L^2(\Omega) \longrightarrow \mathbb{R}$. And so, for f and $g \in L^2(\Omega)$

$$< f, g > = \int_\Omega f(x), g(x) dx.$$

In Chapter 5, we will make use of a special "Lebesgue" space that is not defined in terms of the Lebesgue integral. This space is $L^\infty(\Omega)$, the space of "essentially bounded" functions. A function f is in $L^\infty(\Omega)$ if

$$\operatorname*{ess\,sup}_\Omega |f(x)| < \infty,$$

where

$$\operatorname*{ess\,sup}_\Omega |f(x)| = \inf\{\sup_{x \in S} |f(x)| : S \subset \overline{\Omega}, \text{with } \Omega \setminus S \text{ of measure zero}\}.$$

That is, $|f(x)| \leq \|f\|_\infty$ almost everywhere.

1.3   Banach space valued functions

For evolution problems (those depending on time t), we often deal with Banach space valued functions. For an interval on the real line, I, and a Banach space X, we define the space of continuous functions from I to X as,

$$C^0(I, X) := \{u(t) : I \to X | u(t) \to u(t_0) \ \ \text{in} \ \ X \ \ \text{as} \ \ t \to t_0\}. \qquad (1.7)$$

On this space, we define the functional

$$\|u\|_{L^p(I,X)} := \left(\int_I \| \ u(t)|_X^p dt \right)^{1/p}. \qquad (1.8)$$

1.4   Properties of integral operators

We define the integral operator $K : X \to Y$ as

$$K(f)(x) := \int k(x, y) f(y) dy, \quad f \in X. \qquad (1.9)$$

The mapping $k : Y \times X \to \mathbb{R}$ is called the kernel of K.

Definition: (adjoint operator) K is a self-adjoint operator if $K = K^*$.

Definition: (Hilbert-Schmidt integral operator) The operator $K : X \to Y$ given by

$$K(f)(x) := \int k(x, y) f(y) dy, \quad f \in X,$$

is a Hilbert-Schmidt integral operator if the norm

$$\|k\|_{L^2(\Omega \times \Omega)} = \int_\Omega \int_\Omega |k(x, y)|^2 dx dy < \infty.$$

This norm is called the Hilbert-Schmidt norm where, $\|K\|_{HS} = \|k\|_{L^2(\Omega \times \Omega)}$.

Lemma A.1: *(Compactness of Hilbert-Schmidt Operators) Hilbert-Schmidt integral operators are continuous and compact.*

1.5   Banach's Fixed Point Theorem

In Chapter 6 of this thesis, we make use of the following fixed point result.

Theorem A.1: *(Banach Fixed Point Theorem) Let X be a closed subset of a Banach space $(Y, \|\cdot\|)$, and $h : X \to X$ a function satisfying $\|h(x) - h(y)\| \le k\|x - y\|$, for all $x, y \in X$, where $k < 1$ (we say that h is a contraction, or contraction mapping, on X): Then h has a unique fixed point in X.*

1.6 Gronwall's Inequality

In Chapter 6 of this thesis, we make use of Gronwall's Inequality

Lemma A.2: *Let $x(t) \in \mathbb{R}$ satisfy the differential inequality*

$$\frac{d}{dt_+} \leq g(t)x + h(t).$$

Then

$$x(t) \leq x(0) \exp[G(t)] + \int_0^t \exp[G(t) - G(s)]h(s)ds,$$

where

$$G(t) = \int_0^t g(r)dr.$$

In particular, if a and b are constants and

$$\frac{d}{dt_+} \leq ax + b,$$

Then

$$x(t) \leq (x_0 + b/a) \exp(at) - b/a.$$